Winter March 2015

X-band Dual Polarization Phased-Array Radar for Meteorological Applications

Krzysztof Orzel
University of Massachusetts - Amherst

X-BAND DUAL POLARIZATION PHASED-ARRAY RADAR FOR METEOROLOGICAL APPLICATIONS

A Dissertation Presented

by

KRZYSZTOF A. ORZEL

Submitted to the Graduate School of the
University of Massachusetts Amherst in partial fulfillment
of the requirements for the degree of

DOCTOR OF PHILOSOPHY

February 2015

Electrical and Computer Engineering

X-BAND DUAL POLARIZATION PHASED-ARRAY RADAR FOR METEOROLOGICAL APPLICATIONS

A Dissertation Presented

by

KRZYSZTOF A. ORZEL

Approved as to style and content by:

Stephen J. Frasier, Chair

Robert W. Jackson, Member

Paul Siqueira, Member

Michael Zink, Member

Gopal Narayanan, Member

Christopher V. Hollot, Department Chair
Electrical and Computer Engineering

For my mother and father

In the fields of observation, fortune favors only the prepared mind.
Louis Pasteur

ACKNOWLEDGMENTS

I finally arrived to this very last station of a PhD program. The acknowledgments page is located at the very beginning of a dissertation, but it is in a twisted way the last thing one writes in a process of graduation. Pursuing and getting a PhD degree is a tremendous personal achievement and along the way it is perceived as a lonely journey. PhD is like climbing a big mountain. There are days when it can get very steep. There are times when you have to traverse a valley before you can climb up again. And sometimes ... the weather is just not right. I am very fortunate that I was given a chance to climb my mountain. I would never get here without encouragement, guidance, support and motivation from many people I have met during all these years.

First and foremost, I would like to extend my sincerest thanks to my advisor Prof. Stephen Frasier for the opportunity to work in a unique research environment provided by MIRSL. Thank you for letting me to work on so many cutting edge projects, for all the freedom in scientific problem solving and for stepping in whenever it was needed. I would also like to thank to the professors who make up my thesis committee: Dr. Robert Jackson, Dr. Paul Siqueira, Dr. Michael Zink, and Dr. Gopal Narayanan. Your valuable input has made this dissertation manuscript better.

I am very thankful to Vijay Venkatesh. I have learned a great deal about remote sensing while working with him. I could always count on his help and his contribution to this project is inestimable. The phase-tilt weather radar project was born out of a passion and tireless efforts of Jorge Salazar and Rafael Medina. Tom Hartley and Tom Scott provided much appreciated help during the system assembly phase. I acknowledge Eric Knapp and Rob Palumbo for our countless hallway discussions. Special thanks to Linda Klemyk and Mary Nied for providing administrative support.

I was also very lucky to share office space with Joe Sapp, who became a great companion in this long hike. Big kudos go to all my friends in MIRSL, especially, Razi Ahmed, Tony Swochak, Izzy Masiunas, Peisang Tsai, Bruno Galobart and Matt McLinden, who in one way or another made my stay here more enjoyable.

I wish to express my profound appreciation to my family. I am deeply grateful for having them in my life. I thank my Mum for her constant love and support. I thank my Dad for showing me that great things can be accomplished with grit and perseverance.

Last, but not the least, I would like to thank Laura for her patience, encouragement and love throughout this endeavor. You brought the joy and happiness on the final way to the summit.

ABSTRACT

X-BAND DUAL POLARIZATION PHASED-ARRAY RADAR FOR METEOROLOGICAL APPLICATIONS

FEBRUARY 2015

KRZYSZTOF A. ORZEL

M.Sc., GDANSK UNIVERSITY OF TECHNOLOGY

Dipl.Ing., KARLSRUHE INSTITUTE OF TECHNOLOGY

Ph.D., UNIVERSITY OF MASSACHUSETTS AMHERST

Directed by: Professor Stephen J. Frasier

This dissertation details the development and operation of a novel dual-polarized Phase-Tilt Weather Radar (PTWR) designed for meteorological applications. The use of radar has a well-documented history in detection and classification of weather phenomena, but due to the limited mechanical scanning speed, its usage for severe weather observations remains far from ideal. The PTWR utilizes phased-array technology and provides unique capabilities such as smart scanning, fast scan update, and tracking. This technology is considered a candidate for a replacement and consolidation of the current US weather and surveillance radar networks.

The dissertation can be divided into three parts. First, the hardware design of the radar is presented. Methods of an element and array calibration are discussed. The measured sidelobe level and pattern match exhibit satisfactory performance. The algorithms for signal processing in alternate transmit alternate receive mode

of operation are described in detail. The PTWR weather detection capability is validated by an inter-comparison with a collocated X-band high-power radar. These tests showed correlation exceeding 90% for measurements of reflectivity in a convective storm system. The results support the hypothesis that phased-array technology poses an attractive solution for weather remote sensing.

The second part addresses the radar waveform considerations. The sensitivity of the radar can be improved by several decibels by means of pulse compression techniques. This is necessary, since the PTWR utilizes low-power solid-state transmitters. The work discusses the trade-offs in waveform design and introduces a novel compression filter, which outperforms traditional window-based solutions. The pulse compression performance is validated using clutter data collected by the PTWR, proving that a deep sidelobe reduction in excess of $40dB$ can be achieved at the minimal penalty in signal-to-noise level (below $0.5dB$).

Finally, the third part focuses on the scanning geometry of a 1-D phase-tilt architecture. It is shown that as the elevation angle is increased, the measurements are affected by a self-induced apparent canting angle. The methods of polarization rotation correction are presented. The biases in typical weather radar products such as reflectivity, differential reflectivity, correlation coefficient, and specific propagation phase, are investigated. The analysis shows that for elevation angles below 15°, the retrievals errors are acceptable.

TABLE OF CONTENTS

LIST OF TABLES

Table **Page**

LIST OF FIGURES

Figure **Page**

CHAPTER 1

INTRODUCTION

1.1 Scientific motivation

Over the past decades, several dual polarization radar systems for meteorological research have been developed such as: the fully polarimetric CSU-CHILL (*Brunkow et al.*, 2000), KOUN - the S-band dual polarized prototype for WSR-88D (*Ryzhkov et al.*, 2005), NCAR S-POL (*Keeler et al.*, 2000), OU-PRIME - a high resolution, polarimetric, C-band radar (*Palmer et al.*, 2011), UMass Xpol - a mobile, X-band radar (*Venkatesh et al.*, 2008), and several others. In recent years dual polarization weather radars have entered operational use in Europe (*Kaltenboeck*, 2012),(*Frech*, 2013). The US network of WSR-88D was upgraded to dual polarization during 2011-2012 (*Doviak et al.*, 2000). The information contained in the amplitude and phase of two orthogonal, backscattered, electromagnetic waves allows for hydrometeor classification (*Liu and Chandrasekar*, 2000), better attenuation correction (*Snyder et al.*, 2010), and more accurate estimation of rain rate (*Bringi and Chandrasekar*, 2001).

One still unresolved bottleneck of current meteorological radar systems is low temporal resolution. Long revisit times on the order of 5 minutes reduce the chance to observe quickly evolving phenomena such as tornadoes as well as to issue accurate warnings in advance. It is believed that electronically scanned antennas pose a solution to solve this restriction, but due to the high cost of narrow-beam phased arrays, their implementation in weather sensing radar remains very limited. However, a cost-effective solution is potentially available, if a radar infrastructure can be shared for both weather surveillance and air-traffic control. The the next generation multi-

mission phased-array radar (MPAR) (*Weber et al.*, 2007) promises a consolidation of four US national radar networks: Weather Surveillance Radars operated by National Weather Service, Terminal Doppler Weather Radars funded by the Federal Aviation Agency (FAA), Airport Surveillance Radars and Air Route Surveillance Radars used by FAA and United States Air Force. The MPAR concept assumes polarimetric capability, which can provide an important information for aviation safety such as detection of microbursts (*Wakimoto and Bringi*, 1988).

Phased-array technology is widely used in military and in space missions. For example, the Shuttle Radar Topography Mission utilized fan-beam, active phased-array antennas at C-band and X-band (*Farr et al.*, 2007). The current TerraSAR-X satellites also employ active phased arrays (*Buckreuss et al.*, 2003). Such systems are characterized by a fairly small dynamic range when compared to that required for weather radar. The calibration requirements for a pencil-beam weather radar are far more strict than those for a hard target detection. *Wang and Chandrasekar* (2006) specify the bias in differential reflectivity (Z_{DR}) should be below $0.2dB$, while bias in correlation coefficient (ρ_{hv}) should not exceed 2% in rain observations. These conditions translates into cross-polarization isolation lower than $-40dB$ for simultaneous transmission case, and $-20dB$ if alternate transmission case is considered. The bias restriction in ρ_{hv} means that the H and V antenna patterns should match with an accuracy as high as 98%. These requirements have to be met across entire radar field of view ($\pm 45^\circ$ in azimuth and $\pm 15^\circ$ in elevation for planar array), which makes system design very challenging.

Several rapid scanning systems for weather observations has been developed in the past decade. National Weather Radar Testbed (NWRT) (*Heinselman et al.*, 2008) is a repurposed U.S. Navy SPY-1 S-band phased array radar built in the 1970's. The NWRT has demonstrated advantages provided by use of phased-array technology such as beam multiplexing (*Yu et al.*, 2007) and smart adaptive scanning

(*Torres*, 2012). *Wurman and Randall* (2001) developed a mobile, Xband, hybrid electronic/mechanical scanning radar for severe weather observations. The frequency dependent beam steering allows for a rapid elevation scanning in range between 0° and 13.5°. Another mobile X-band radar, $MWR-05XP$, uses a different hybrid approach, with pulse-to-pulse electronic elevation scanning, limited electronic azimuth scanning, and rapid mechanical azimuth scanning (*Bluestein et al.*, 2009). The temporal resolution can be even further improved, if digital beamforming techniques are employed as demonstrated by the Atmospheric Imaging Radar (AIR) (*Isom et al.*, 2013). A common feature of all of the systems mentioned above is a lack of dual polarization capability. A design of a cylindrical polarimetric phased array radar is in progress (*Karimkashi et al.*, 2013).

The existing weather sensing networks are based on long-range radars such as S-band NEXRAD and C-band TDWR. However, due to the earth curvature, observations of the lower part of the atmosphere are not always available. The Engineering Research Center for Collaborative Adaptive Sensing of the Atmosphere (CASA) suggests the use of a low cost, low power dense radar network to overcome this limitation (*McLaughlin et al.*, 2009). Additionally, using a dense radar network a significant improvement in an average spatial resolution can be achieved.

The higher spatial resolution was one of the main motivations behind the second Verification of the Origins of Rotation in Tornadoes Experiment (VORTEX2) (*Wurman et al.*, 2012). In this experiment a fleet of mobile weather sensing systems was used to observe tornadic and nontornadic supercell thunderstorms with an extraordinary level of detail. *Snyder et al.* (2013), using high resolution X-band radar data, was able to define a new polarimetric signature in tornadic storms such as a low reflectivity ribbon, which is depicted as a narrow zone of reduced reflectivity and differential reflectivity near the hook area. *Tanamachi et al.* (2013), using high resolution W-band radar data, described the full life cycle of a sub-tornado strength,

convective storm vortex, which met tornado criterion, but was not related with a visible condensation funnel.

The selection of an X-band technology for CASA dense radar network is a compromise between the size of antenna and the expected attenuation due to propagation in a water filled atmosphere. The CASA IP1 Test-bed (*Junyent et al.*, 2010) has demonstrated the improvement in temporal resolution (5 times faster than NEXRAD), spatial resolution (tornado tracking with a street level accuracy), dual Doppler wind estimation, and quantitative precipitation estimation resulting in better flash flood prediction.

The CASA concept involves usage of multiple radar nodes and therefore the reliability of utilized infrastructure is of the highest concern. *Salazar et al.* (2008) proposed use of a solid-state transmitters and a 1-D phased-array system in order to accomplish this goal. The Microwave Remote Sensing Laboratory (MIRSL) at the University of Massachusetts in collaboration with CASA has developed a state-of-the-art, low-cost, dual-polarized Phase-Tilt Weather Radar (PTWR) as a proof-of-concept. This prototype radar assumes electronic scanning in azimuth and mechanical scanning in elevation. It is proposed here to evaluate polarization purity, calibration stability, data quality, and rapid scanning capability unique to 1-D phased array architecture.

1.2 Dissertation outline

This work builds upon previous contributions to the phase-tilt weather radar project. *Salazar Cerreno* (2012) addressed the feasibility of low-cost, dual-polarized, X-band phased array antennas for use in dense radar networks for weather surveillance. A prototype antenna has been designed, fabricated and tested. *Medina-Sanchez* (2013) developed a beam steering control system and related calibration techniques. A prototype array system populated by 64 TR modules has been integrated and its performance has been verified in an anechoic chamber. *Krishna-*

murthy (2011) designed the Array Formatter using a Field Programmable Gate Array (FPGA)-based master controller that translates user commands from a computer into control and timing signals for the radar system. PTWR was also used to verify spaced-antenna wind estimation algorithms developed by *Venkatesh* (2013).

This dissertation describes the design, capability, and limitations of a 1-D active phased-array system for weather surveillance. It is organized as follows.

Chapter 2 provides a brief description of hardware architecture. The signal processing flow is presented followed by a comprehensive explanation of a multithreading data acquisition and processing. The configuration of PTWR is very flexible, and various pulsing schemes were tested. The weather radar processor using a staggered pulse repetition time (PRT) scheme under alternate polarization mode was selected as the standard scheme. The PTWR was operated on a mobile platform during Spring-Winter 2013 in Western Massachusetts and as a fixed roof installation in Arlington, Texas during Spring 2014. The summary of available datasets is given. To verify the observational capabilities of the PTWR, a qualitative comparison with S-band weather radar and a quantitative comparison with collocated X-band radar is presented.

In Chapter 3 methods of calibration are evaluated. First, individual TR modules are characterized using a near field probe in a laboratory environment. This technique is compared against a mutual coupling based characterization, which does not require external measurement equipment and can be used as an in-field calibration method. The TR module short term stability and temperature drift effect are assessed. Second, the array beam forming capability is verified using a horn antenna and corner reflector as a calibration standard. The beam gain, peak sidelobe level, 3dB beamwidth and beam pointing error are estimated in all four modes of operation (TxH, TxV, RxH, RxV).

Chapter 4 focuses on waveform design for a solid-state weather radar. A brief description of pulse compression techniques is given. The trade-offs in optimal waveform design are discussed. The method for an inverse filter computation is provided and its theoretical performance is examined. The designed waveform was recorded using a horn antenna. This measurement was used to evaluate the effect of waveform predistortion on pulse compression performance. The results are compared with standard compression methods such as a matched filter and Hann window. Finally, pulse compression performance using a clutter target is presented.

Chapter 5 describes the scanning geometry for 1-D phased array architecture. The dependence of an effective beam direction on a tilt angle and radar defined beam direction is given. The effect of polarization rotation is discussed and its impact on scattering matrix is described. The bias correction method is suggested. The retrieval biases in reflectivity, differential reflectivity, correlation coefficient, specific differential phase, and linear depolarization ratio due to apparent canting angle when the beam is scanned away from broadside are analyzed.

Finally, chapter 6 summarizes the conclusions of this work and suggests the possible future development in the phased-array weather meteorology.

The broad goal of this work is to validate that the PTWR presents a viable alternative to a high-power, spinning dish antenna radar systems. The contributions of this dissertation are:

1. Design, implementation, and development of the first-of-its-kind dual-polarized phased-array weather radar.

2. Demonstration that the designed low-power phased array system provides comparable data quality as a high power magnetron based X-band radar.

3. Demonstration of a low-cost in-field calibration method based on a mutual coupling technique.

4. Validation of a novel pulse compression filter, which provides substantial side-lobe level reduction at a minimal penalty in signal to noise ratio based on real data and simulations.

5. Description of a scanning geometry unique to a 1-D phase-tilt radar and the impact of the apparent canting angle on data quality.

CHAPTER 2

SYSTEM DESCRIPTION

2.1 System overview

The Microwave Remote Sensing Laboratory (MIRSL) at the University of Massachusetts has developed a low-cost, mobile, dual-polarized Phase-Tilt Weather Radar (PTWR) presented in Figure 2.1. The PTWR block diagram is shown in Figure 2.2. The system consists of the phase-tilt antenna, up/down converter, IF digital transceiver, host computer, pedestal and array controller/formatter. The phase-tilt antenna subsystem was designed by the Center for Collaborative Adaptive Sensing of the Atmosphere (CASA) for use in distributed, collaborative, and adaptive sensing networks (*Hopf et al.*, 2009). It is a one dimensional dual-polarization active array antenna that enables electronic scanning in the azimuth plane, while scanning in the elevation plane is performed mechanically. This type of antenna architecture reduces the number of required T/R modules and hence significantly decreases the overall system cost. Furthermore, the antenna subsystem is a modular design composed of four line replaceable units (LRU). This design approach is an attempt to facilitate future system extensions.

An FPGA based array controller/formatter provides control and timing signals for all subsystems (with the exception of pedestal). Owing to low peak power provided by solid state based T/R modules, implementation of pulse compression techniques is required. The transmitted nonlinear chirp is produced by an arbitrary waveform generator within the digital IF transceiver and is compressed by means of an inverse

a)

b)

Figure 2.1. a) The PTWR deployed in Hadley,MA on a mobile platform in storm season 2013 b) The PTWR deployed on a roof at the University of Texas Arlington in storm season 2014.

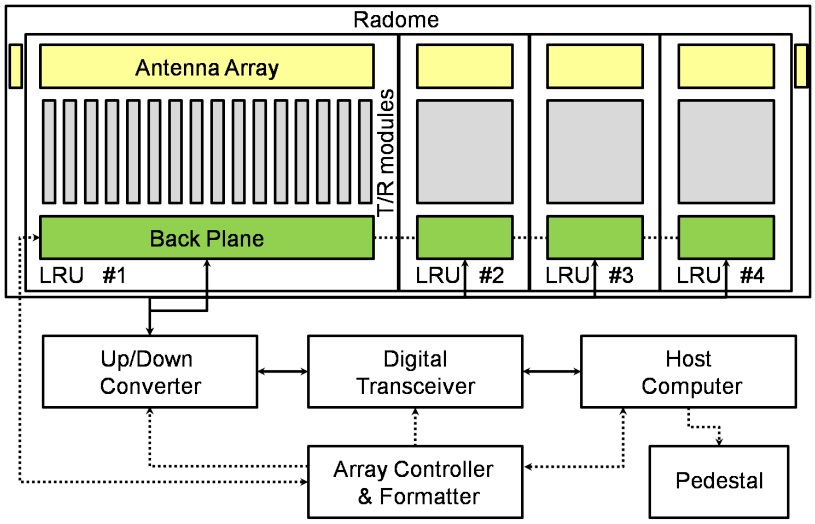

Figure 2.2. MIRSL phased array radar block diagram and signal flow.

filter. The host computer generates all scanning settings, executes signal processing, and controls the data flow. Radar system specifications are shown in Table 2.1.

2.1.1 Phase-Tilt Antenna Subsystem

Each LRU consists of an antenna array (0.27 x 0.56 m), a set of 16 T/R modules and a DC and signal distribution backplane. The full antenna assembly is a planar structure of 72 columns. The central 64 columns of the antenna array are fed by dedicated T/R modules, while the remaining 8 outer columns are used as terminated dummy elements in order to reduce the effects of diffraction and non-uniform mutual coupling (*Knapp et al.*, 2011). Each column is a dual linear polarized subarray composed of 32 aperture coupled microstrip patch antennas interconnected by series-fed networks for each polarization. Here, two serpentine lines are implemented to feed each radiating element in both polarizations. Although a series feed, when compared to its corporate alternative, exhibits lower transmission loss and require less substrate area, its performance is frequency dependent, which limits antenna bandwidth.

The phase tilt antenna allows scanning of $\pm 45^\circ$ in the horizontal plane with a beam width of 3.5° in elevation and 1.8° in azimuth at broadside. It is also important

Table 2.1. PTWR parameters.

Parameter	**Specifications**
Radar system dimensions [m]	1.47 x 0.82 x 0.30
Weight [kg]	82
Frequency [GHz]	9.3 - 9.4
Transmit power (peak) [W]	60
Pulse compression gain [dB]	up to 20
Duty cycle	up to 30%
Beam width [°]	2 (azimuth) x 3.5 (elevation)
Integrated cross-pol isolation [dB]	< -15
Range resolution [m]	> 37.5
Polarization	alternate H & V
Radar products	$Z_h, V, \sigma_v, Z_{dr}, \rho_{hv}, \phi_{dp}, \kappa_{dp}, LDR$

to highlight that in case of dual polarized phased arrays, removing biases due to the coupling of the H and V fields exhibits a great challenge, since the antenna radiation patterns depend on the pointing direction. *Wang and Chandrasekar* (2006) reported that cross-polarization isolation in excess of -20 dB is required to maintain measured bias error in differential reflectivity below 0.1 dB. The first prototype of the CASA phase tilt antenna described by *Salazar et al.* (2010) meets this requirement. The cross-polarization isolation of -35 dB and -32 dB at broadside for V and H respectively was measured in the frequency range between 9.3 GHz to 9.4 GHz. Furthermore if these values are integrated across entire scanning range of $\pm 45°$, cross polarization better than -21 dB is obtained for both channels.

A block diagram of a TR module is presented in Figure 2.3. The TR module architecture can be broken down into four sets of components: control block, diversity switch, and transmit and receive channels. Operation of each individual TR module is controlled by an independent FPGA, which can be accessed and programmed by the array formatter. A custom-designed, high-power, four-port diversity switch is a star configuration of four GaAs single pole, single throw PIN diode switches. It is

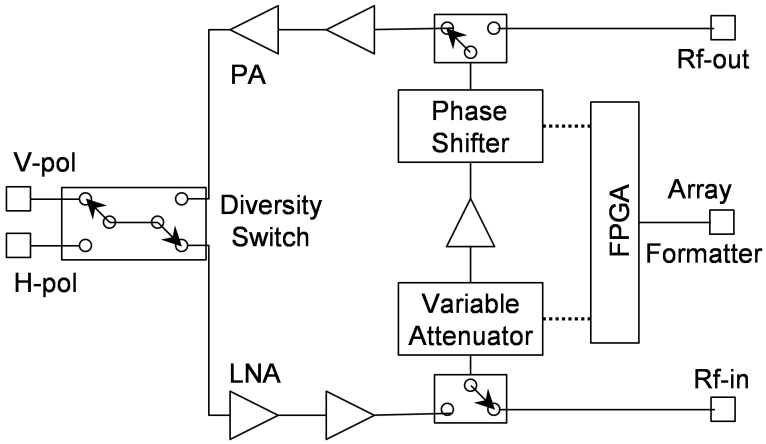

Figure 2.3. TR module block diagram.

characterized by an insertion loss less than 3 dB and isolation in excess of 45 dB over the frequency band 9 to 9.6 GHz. This design approach allows calculation of all polarimetric products, but also forces alternate transmit alternate receive (ATAR) mode of operation. The transmitter block consists of a high and medium power amplifier. The transmit peak power is about 1.25 W. The receiver block consists of a low noise amplifier and a gain block. The TR modules design utilizes a common leg architecture (*Medina et al.*, 2012a), i.e., phase shifter, gain block, and variable attenuator are shared between transmit and receive channels. This configuration features 360° of phase control with 5.6° of resolution and 31.5 dB of amplitude control with 0.5 dB of resolution. The common part of the circuit is connected to the independent input and output ports by means of two switches.

Each LRU backplane is used as an interface between TR modules and the remaining part of the system. The backplane provides DC power distribution and a 25 MHz low voltage differential signals bus for fast programming and communication to the TR modules.

2.1.2 RF subsystem

Figure 2.4 shows a block diagram of the RF subsystem. It consists of a double stage up- and down-converter. All radar subsystems are referenced to the master clock operated at 100 MHz. The usage of common PLL clocks guarantees that the received signal will be always contained within the bandwidth of the antialiasing bandpass filter located at the end of the down-converter chain. The first bandpass filter in the up-conversion chain suppresses spurious signals generated by DAQ transmitter, while the second bandpass filter rejects the 1.7 GHz LO signal. This architecture provides over 48 dB suppression of undesired signals in transmit mode within the bandwidth of antenna.

A 2-way switch located at the beginning of the receiver chain, combined with a 30 dB coupler located next to the high power amplifier in the transmitter chain, enables real-time control of the RF subsystem stability. The transmitted pulse is stored using a calibration path and can be used as a reference waveform for subsequent pulse compression processing. The coaxial limiter located in front of the DAQ input port protects analog-digital converters and ensures that the received signal power is below 10 dBm.

2.1.3 Control subsystem

A core component of the PTWR is the array formatter. It is an FPGA-based master controller that translates user commands from the host computer to control and timing signals for the radar system. The array formatter loads look-up tables and sequence tables for all TR modules.

The look-up table (Figure 2.5) contains the calibration values required for the phase shifter and digital attenuator to switch to the requested beam location. The look-up table defines 256 beam positions in four modes of operation (TxV, TxH, RxV, RxH). The structure of the look-up table is common for all TR modules, but

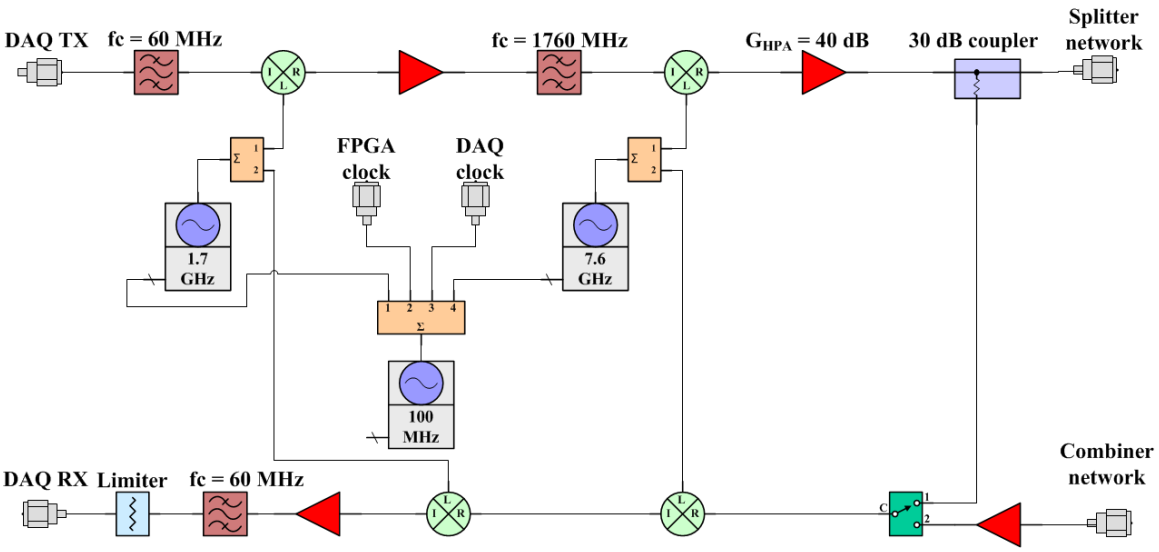

Figure 2.4. RF subsystem block diagram.

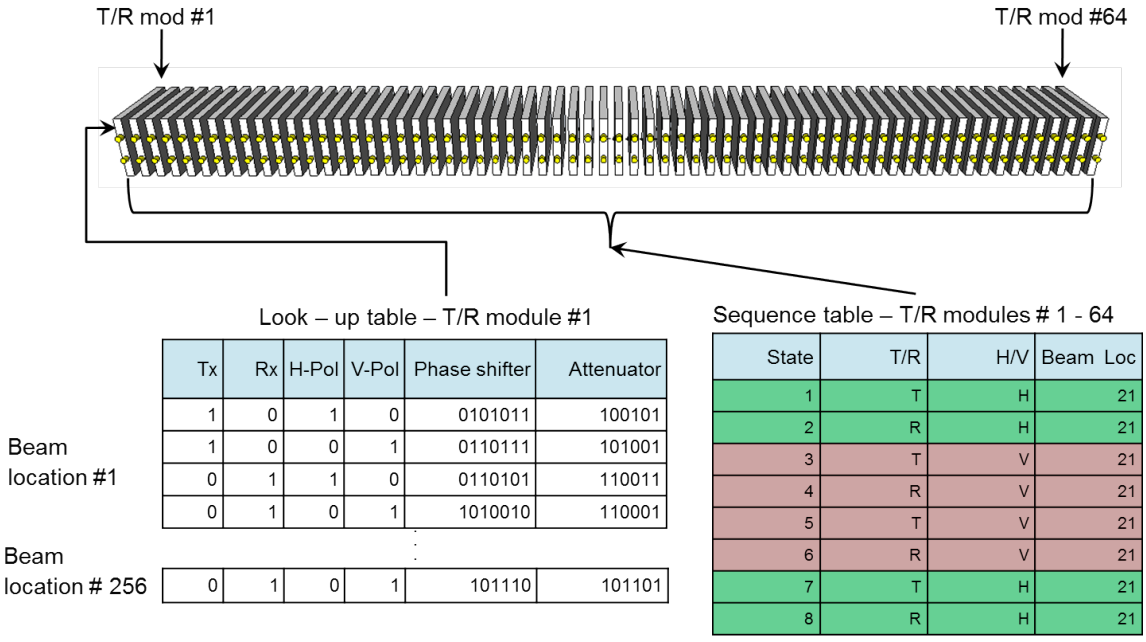

	Tx	Rx	H-Pol	V-Pol	Phase shifter	Attenuator
Beam location #1	1	0	1	0	0101011	100101
	1	0	0	1	0110111	101001
	0	1	1	0	0110101	110011
	0	1	0	1	1010010	110001
Beam location # 256	0	1	0	1	101110	101101

State	T/R	H/V	Beam Loc
1	T	H	21
2	R	H	21
3	T	V	21
4	R	V	21
5	T	V	21
6	R	V	21
7	T	H	21
8	R	H	21

Figure 2.5. Beam location look-up table and sequence table definition.

the settings for phase shifter and attenuator are specific to the individual TR module. Once the radar system is turned on, the array formatter uploads the look-up tables to the individual TR modules on time order of 3 minutes.

The radar operator then specifies the requested beam locations and polarimetric mode of operation. This information forms the beam sequence table (Figure 2.5), which defines 4 pulses. In order to collect more pulses per beam, a sequence table repetition factor is defined. Since the sequence table holds only memory register addresses, which are common for all TR modules, the array formatter broadcasts a single sequence table simultaneously to all TR modules. In the next step, the timing information is passed from the host computer to the array formatter in order to set up the state machine. The entire procedure is repeated for each beam.

2.1.4 Data acquisition subsystem

The data acquisition subsystem consists of a high speed digital transceiver, PC based signal processor, and a RAID for data storage. A commercial digital transceiver (Pentek 7140) is integrated into the host computer and serves as an arbitrary waveform generator and a data digitizer. The transmitted waveform utilizes up to 5 MHz of bandwidth and is synthesized at the intermediate frequency (IF) of 60 MHz. On board 14-bit A/D converters sample the IF receiver channel at 100 MHz rate. The resulting sampled IF signals alias to an apparent intermediate frequency of 40 MHz. Then a digital complex mixer shifts the real valued input signal down to a complex baseband representation. Finally the signal is filtered and decimated by a factor of 16, resulting in 16 bit in-phase and quadrature samples generated at a 6.25 MHz sampling rate. The 14-bit A/D converters provide 78 dB of dynamic range, which is sufficient for a short range X-band weather radar system.

The signal processing flow chart is presented in Figure 2.6. During radar software boot up, the main program process initializes 3 additional threads. In order to im-

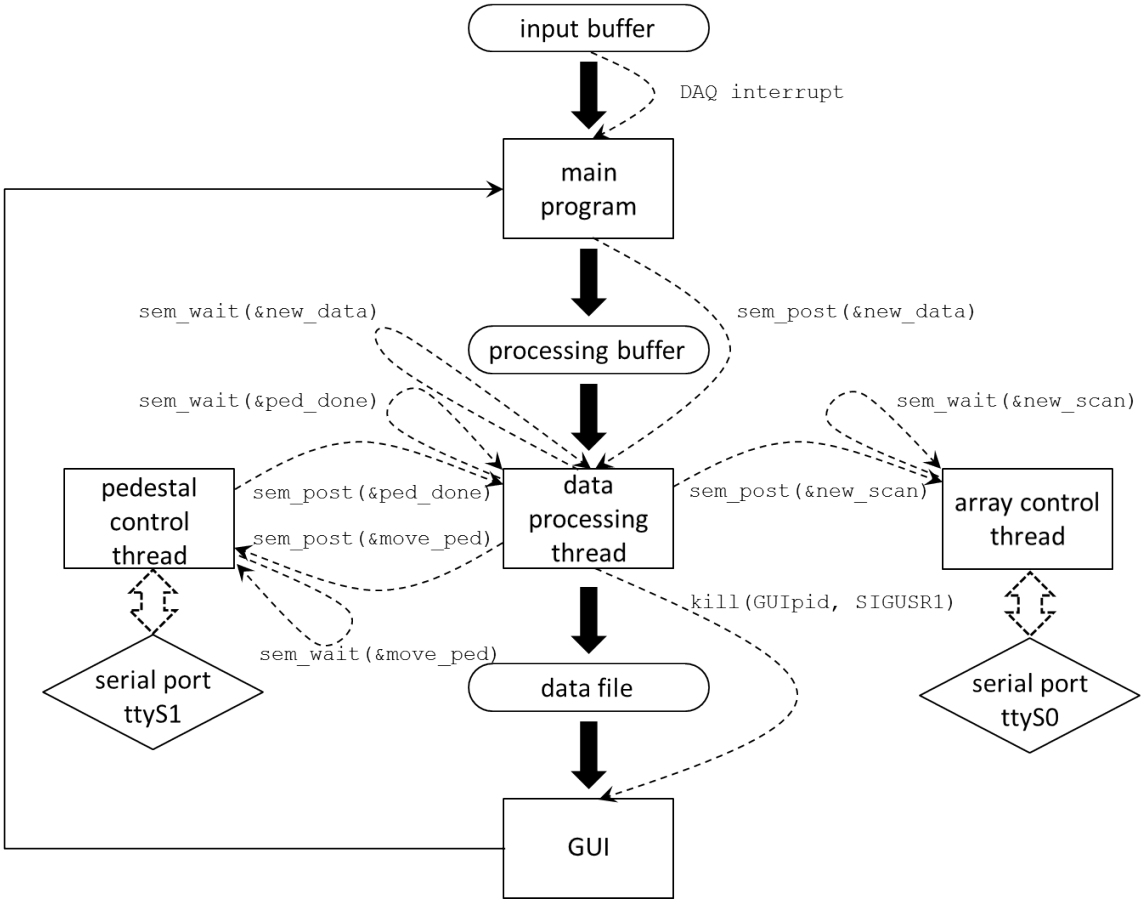

Figure 2.6. PTWR signal processing flow chart. Solid arrows represent the data flow, while the dashed arrows represent system signals, which are required to enable multithreaded processing.

prove the system's real time performance, each thread runs on a dedicated processor. A set of counting semaphores is utilized to prevent the simultaneous modification of the processed data by more than one thread. Once the initial setup is completed, the main program waits for a system interrupt. This signal is generated by the DAQ card each time 4 pulses of raw data are collected. When the interrupt is generated, the main program checks if the received data is in order and moves it to the processing buffer, which is shared with the data processing thread. With the arrival of new data, the value of a shared semaphore is increased.

An array control thread sends a trigger request to the array formatter once per scan. On receiving this signal, the array formatter executes the previously loaded sequence tables. If the execution of the sequence table is successful, the array formatter sends a confirmation back to the array control thread. The pedestal position is requested and monitored by the pedestal control thread. The activity of this thread depends on the requested mode of operation. If the electronic sector scan is requested, this thread will be called only once. If the electronic volume scan is requested, the pedestal control thread will be called each time a new elevation is set. If the mechanical sector scan is requested, the pedestal control thread will be running continuously. The data processing thread implements a pulse compression filter using an open source C subroutine library for computing discrete Fourier transforms called FFTW (*Frigo and Johnson*, 2005). Once this procedure is completed, a set of covariances at lags 0, 1 and 2 is computed and stored in a Level 1 intermediate file.

The Python based graphical user interface (GUI) is presented in Figure 2.7. The radar operation parameters are selected by a user in the *Settings* tab and stored in a configuration file. This file is then passed to the main radar program. Once the first sector scan is completed, the Linux system call notifies the GUI of a new data file. Finally, the GUI calls Python functions to compute radar products and displays them in a separate tab (see Figure 2.7b).

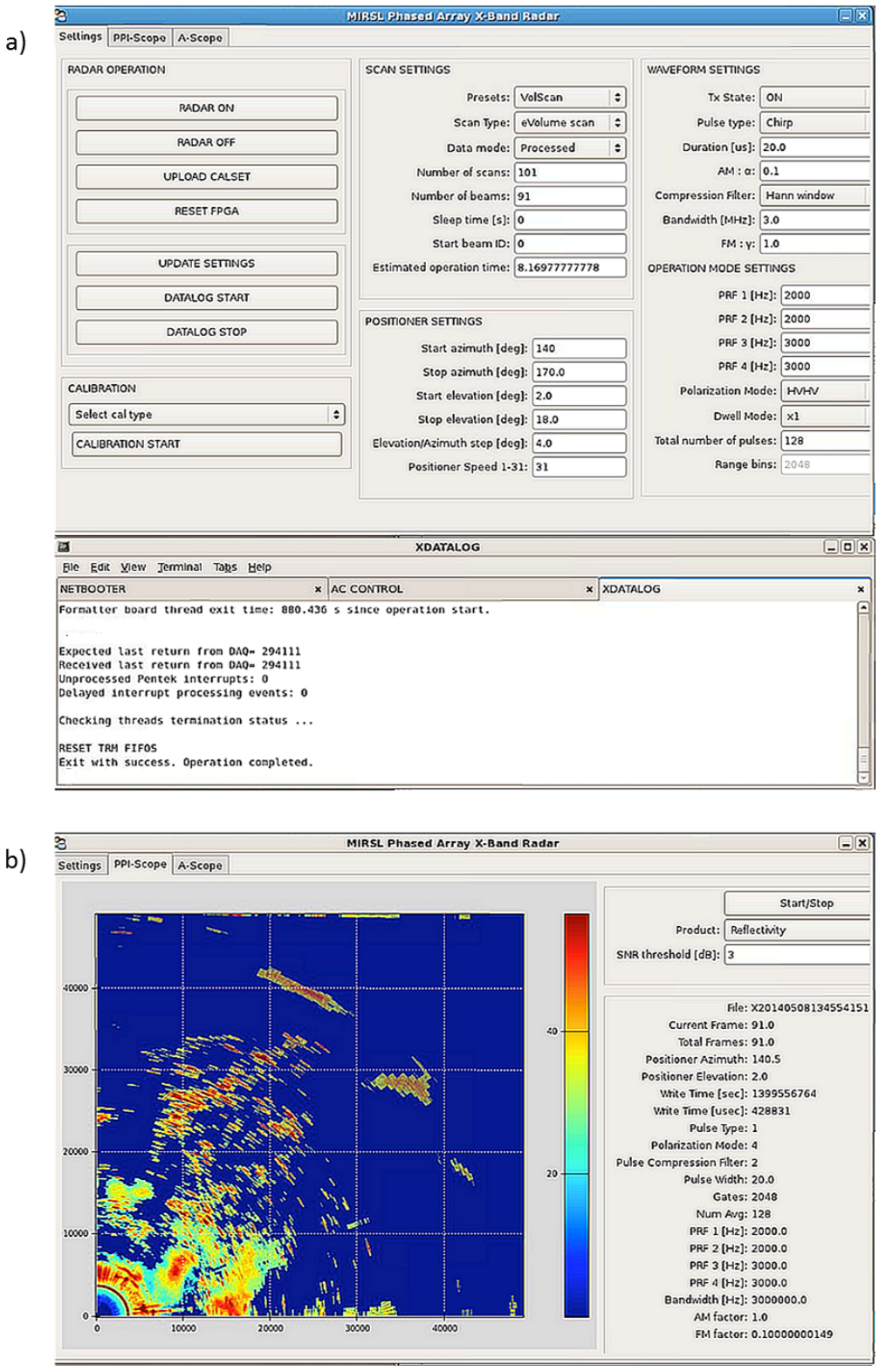

Figure 2.7. PTWR graphical user interface: a) radar settings tab, b) plan position indicator (PPI) display tab.

2.2 Signal processing using a staggered PRT scheme under alternate polarization mode

The PTWR utilizes the alternate-transmit-alternate-receive (ATAR) mode of operation, which enables measurement of all 9 components of the backscattering covariance matrix. The most elementary means of operation is to transmit a polarization sequence of HVHV at a constant pulse repetition frequency (*Bringi and Chandrasekar*, 2001). This pulsing scheme does not provide the measurement of cross-polarized parameters such as linear depolarization ratio. However, most of the observed weather events are exhibiting negligible depolarization properties and hence this measurement is usually not required. The main drawback of this pulsing scheme is that the maximum unambiguous velocity is limited to:

$$v_{max} = \pm\frac{\lambda}{4T} \tag{2.1}$$

and the Doppler velocity is calculated as:

$$v = \frac{\lambda}{4\pi T}\angle R(T) \tag{2.2}$$

where $R(T)$ is the signal autocorrelation at a sample time lag T.

This can be a significant issue especially at higher frequencies. For example, assuming $f_p = 2$ kHz, maximum unambiguous velocity at S-band is $\pm$ 50 m/s, while at X-band it is only $\pm$ 16 m/s. Since wind velocities in excess of 30 m/s can be expected during severe weather outbreaks, implementation of the staggered PRT technique is required. This method utilizes two velocity estimates: v_1 obtained from samples spaced by $2T_1$, and v_2 obtained from samples spaced by $2T_2$. Then the maximum unambiguous velocity can be defined as (*Doviak and Zrnic*, 1993):

$$v_{max} = \pm\frac{\lambda}{4(2T_1 - 2T_2)} \tag{2.3}$$

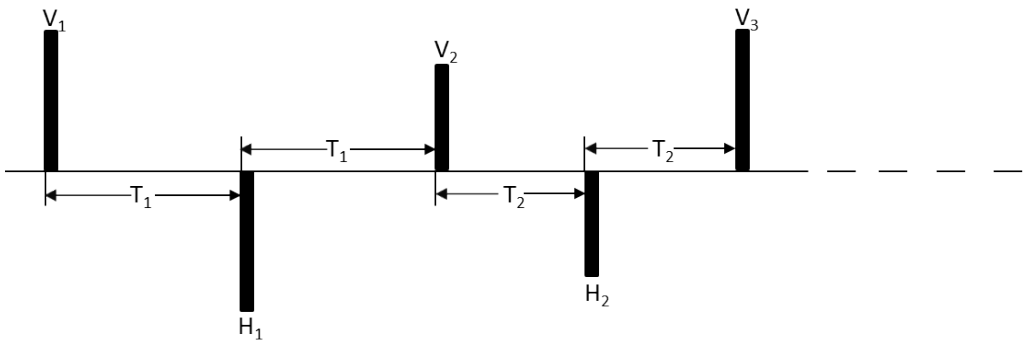

Figure 2.8. Staggered pulsing scheme used in PTWR. V-polarized pulses are staggered at $PRT_1 = 2T_1$ and $PRT_2 = 2T_2$ and $PRT_2/PRT_1 = 2/3$. H-polarized pulses are triggered at constant $PRT_3 = T_1 + T_2$

and the Doppler velocity is calculated as:

$$v = \frac{\lambda}{4\pi(T_1 - T_2)} \angle \frac{R(T_2)}{R(T_1)} \tag{2.4}$$

Zrnic and Mahapatra (1985) have shown that the standard error in velocity estimatation increases as the difference between T_1 and T_2 decreases. It is suggested to choose the ratio $T_2/T_1 = 2/3$, which provides good compromise between increasing unambiguous velocity, while decreasing error in the velocity estimate. The additional benefit of the staggered PRT technique is the improvement in unambiguous range.

The dual polarized staggered PRT scheme utilized by the PTWR is presented if Figure 2.8. H pulses are uniformly spaced by $PRT_3 = T_1 + T_2$, while V pulses are staggered at $PRT_1 = 2T_1$ and $PRT_2 = 2T_2$. The uniform spacing of H-pulses enables simpler clutter filtering processing in H-channel. Estimation of the Doppler velocity using a staggered PRT benefits from a higher SNR expected in V-channel. Following procedure described by *Golestani et al.* (1995) several correlation products can be defined. The co-polar correlations can be estimated as:

$$
\begin{aligned}
P_H &= \frac{1}{N}\sum_{i=1}^{N}|H_i|^2 \\
P_V &= \frac{1}{N}\sum_{i=1}^{N}|V_i|^2 \\
R_{VV}(2T_1) &= \frac{2}{N}\sum_{i=1}^{N/2}(V_{2i}V_{2i-1}^*) \\
R_{VV}(2T_2) &= \frac{2}{N-2}\sum_{i=1}^{N/2-1}(V_{2i+1}V_{2i}^*) \\
R_{HH}(T_1+T_2) &= \frac{1}{N-1}\sum_{i=1}^{N}(H_{i+1}H_i^*)
\end{aligned}
\tag{2.5}
$$

and the cross-polar correlations can be estimated as:

$$
\begin{aligned}
R_{HV}(T_1) &= \frac{2}{N}\sum_{i=1}^{N/2}(H_{2i-1}V_{2i-1}^*) \\
R_{VH}(T_1) &= \frac{2}{N}\sum_{i=1}^{N/2}(V_{2i}H_{2i-1}^*) \\
R_{HV}(T_2) &= \frac{2}{N}\sum_{i=1}^{N/2}(H_{2i}V_{2i}^*) \\
R_{VH}(T_2) &= \frac{2}{N-2}\sum_{i=1}^{N/2-1}(V_{2i+1}H_{2i}^*)
\end{aligned}
\tag{2.6}
$$

where N is the number of pulses in each polarization channel. The co-polar correlation $R_{HH}(T_1+T_2)$ can be used to calculate mean velocity at lag-2, while $R_{VV}(2T_1)$ and $R_{VV}(2T_2)$ can be used to calculate mean velocity utilizing staggered PRT scheme. The unambiguous velocity range can be further increased, if the information contained in the cross-polar correlations is used. The phase of cross-polar products contains the contribution due to Doppler shift ϕ_D and the two-way differential propagation shift ϕ_{dp} and are defined as follows:

$$
\begin{aligned}
\phi_{dp}(T_1) &= \frac{1}{2}(\angle(R_{HV}(T_1)) - \angle(R_{VH}(T_1))) \\
\phi_{dp}(T_2) &= \frac{1}{2}(\angle(R_{HV}(T_2)) - \angle(R_{VH}(T_2)))
\end{aligned}
\tag{2.7}
$$

$$\begin{aligned}\phi_D(T_1) &= \frac{1}{2}(\angle(R_{HV}(T_1)) + \angle(R_{VH}(T_1))) \\ \phi_D(T_2) &= \frac{1}{2}(\angle(R_{HV}(T_2)) + \angle(R_{VH}(T_2)))\end{aligned} \tag{2.8}$$

These phase estimates are only unique within an interval of 180°. However, the ambiguity in measured ϕ_{dp} can be easily resolved due to the fact that in most cases it is a monotonically increasing function of range. If this correction is applied, then using the procedure given by *Sachidananda and Zrnic* (1989) we can calculate a corrected differential phase ϕ^c_{dp} as:

$$\phi^c_{dp} = \frac{1}{2}(\phi^c_{dp}(T_1) + \phi^c_{dp}(T_2)) \tag{2.9}$$

$$\begin{aligned}R(T_1) &= \frac{1}{2}(R_{VH}(T_1)e^{-i\phi^c_{dp}} + R_{HV}(T_1)e^{i\phi^c_{dp}}) \\ R(T_2) &= \frac{1}{2}(R_{VH}(T_2)e^{-i\phi^c_{dp}} + R_{HV}(T_2)e^{i\phi^c_{dp}})\end{aligned} \tag{2.10}$$

where ϕ^c_{dp} is corrected diffrential propagation phase. The velocity estimate using arguments of $R(T_1)$ and $R(T_2)$ can be computed using a staggered PRT scheme, since $T_2/T_1 = 2/3$.

The magnitude of the co-polar correlation coefficient ρ_{hv} can not be computed directly, because the cross-correlation $R_{HV}(0)$ is not available in the alternate transmission mode. It can be computed indirectly as (*Doviak and Zrnic*, 1993):

$$\rho_{hv} = \frac{|R_{VH}(T_2)| + |R_{HV}(T_2)|}{2\sqrt{(P_H - N_H)(P_V - N_V)}} \left| \frac{R_{VV}(PRT_2)}{(P_V - N_V)} \right|^{-0.25} \tag{2.11}$$

where N_H and N_V are the estimates of white noise power in H- and V-channel.

2.3 Weather radar equation for a phased array radar

The effective size of an antenna is reduced, when radar scans away from broadside. This results in an increase in a beam width and a decrease in a beam gain, which can be approximated as follows:

$$G_{TX} = G_{TX(\Theta_0)} cos\alpha - L_r$$
$$G_{RX} = G_{RX(\Theta_0)} cos\alpha - L_r - L_t \tag{2.12}$$
$$\Theta_s = \frac{\Theta_0}{cos\alpha}$$

where G_{TX} and G_{RX} are the antenna transmit and receive gain, L_r is a radome loss. L_t is a loss due to Taylor taper function, α is a beam steering angle, and Θ_0 is the azimuth beam width at broadside, and Θ_s is a beam width at the steering angle α. Equation 2.12 is valid only for large arrays and even in this case can be used only as an approximation. Therefore it is suggested to use antenna calibration factors in order to guarantee accurate differential reflectivity estimates.

The impact of beam broadening on a radar equation is described by *Knorr* (2007). In case of a 1-D phased array the reflectivity factor can be estimated as follows:

$$dBZ = 10\log_{10}(C) + P_r[dBm] + 20\log_{10}(r)[km] - 10\log_{10}(\tau)[s] \tag{2.13}$$

and radar constant C is defined as:

$$C = \frac{10^{21} 1024 ln(2) \lambda^2 L_{PC}}{P_{TX} G_{TX} G_{RX} \Theta_s \phi c \pi^3 |K|^2} \tag{2.14}$$

where P_r is a received power, r is a range from radar, τ is a pulse width,λ is the wavelength, L_{PC} is a loss due to pulse compression filter, P_{TX} is a transmitted power, ϕ is a $3dB$ beam width in elevation, c is a speed of light, and K is the complex refractive index of water.

2.4 Overview of available datasets

The PTWR data repository contains multiple data sets collected during Summer and Fall 2013 in Hadley, MA. The topography of Western Massachusetts is domi-

nated by the Berkshires, a broad belt of steeply rolling hills, and a rift valley of Connecticut River. These topographical features, combined with relatively wide antenna beamwidth restricts the possibility to collect clutter-free data close to the ground. On average the precipitation intensity weakens and the storm structure decomposes into several cells as the weather system enters Western Massachusetts, making the data collection particularly challenging. The radar platform pitch and roll was leveled within $\pm 0.2^{\circ}$ with respect to the ground.

The radar configuration is highly flexible, owing to alternate transmit and receive mode of operation, independent control of individual modules, high duty cycle, and ability to scan mechanically using broadside beam only offers a great flexibility in radar configuration. The PTWR pulsing scheme is based on a set of 4 pulses repeated n-times per beam. For example, radar mode HVHV means that all odd pulses are transmitted at horizontal polarization, while even pulses are transmitted at vertical polarization. This is the intended standard mode of operation. It can provide unambiguous Doppler velocity of $\pm$ 30 m/s up to 40km in range, which is sufficient for most meteorological observations. Cross-polarized measurements are provided in POL mode. The radar is also capable of synthesizing beams using only a part of all available TR modules, which is necessary to implement a spaced antenna (SA) mode of operation. Eigenvalue signal processing (ESP) and bias correction (BC) modes of operation were implemented to investigate the bias in polarimetric radar products due to rotation of polarizations as the beam is steered away from broadside at higher tilt elevations.

The majority of measurements were performed in a raster scan mode combining electronic sector scan at multiple elevation angles spanning from 2 to 16 degrees. Some data sets were collected in a sector scan mode, with rapid update time on a scale of 2-3 seconds, to examine the capability of imaging fast moving storm systems. The repository contains NEXRAD KENX radar data for qualitative comparison studies.

A limited possibility for quantitative comparison between PTWR and CASA-MA-1 radar exists in few cases. The summary of data collected in Summer/Fall 2013 is presented in Table 2.2.

During spring 2014, the PTWR was deployed as a fixed roof installation in Arlington,TX. The direct proximity (250 meters away) of XUTA, a magnetron-based radar, allowed for a qualitative and quantitative data comparison. XUTA is an X-band dual polarization radar, which is part of the Dallas-Fort Worth Urban Demonstration Network (*Chandrasekar et al.*, 2013) (*Bajaj and Philips*, 2012) operated by CASA. The DFW test bed is the first demonstration of a short-range weather radar network deployed in a metropolitan area. The biggest advantage of this sensor network is an improvement in temporal and spatial resolution, along with the availability of radar observations close to the ground. As a consequence, it is expected to generate more accurate detections and forecasts of low altitude wind, tornado, hail, ice, and flash flood hazards. The provided weather hazard information can be validated using a set of existing sensors, such as NEXRAD WSR-88D and TDWR radars, and rain gauges. Figure 2.9 presents the locations of all available weather radars in the Dallas-Fort Worth area during the spring 2014 deployment. The specifications of the radar systems are listed in Table 2.3. The PTWR collected data in multiple weather events using a staggered PRT scheme described in Section 2.2. The summary of data collected in Spring 2014 is presented in Table 2.4.

Table 2.2. Summary of data collected by PTWR in season 2013. CASA MA-1 X-band radar was operational during deployments # 1-6 allowing for a limited quantitative comparison.

#	Date	Weather event	Radar mode
1	6/17/2013	severe thunderstorm watch	HHVV, POL
2	6/24/2013	severe thunderstorm warning	HHVV
3	6/28/2013	severe thunderstorm warning	HHVV, HVHV, POL
4	7/01/2013	stratiform rain	HHVV, HVHV, POL
5	7/07/2013	severe thunderstorm warning tornado warning	HHVV
6	7/10/2013	stratiform rain	HHVV, POL, SA
7	7/23/2013	stratiform rain	HVHV, SA, BC
8	8/01/2013	stratiform rain	HVHV, BC
9	8/26/2013	stratiform rain	HVHV, SA, BC
10	10/03/2013	clutter measurements	HVHV
11	10/04/2013	stratiform rain	HVHV, ESP
12	10/07/2013	severe thunderstorm warning tornado warning	HVHV, POL
13	10/31/2013	stratiform rain	HVHV
14	11/01/2013	stratiform rain	HVHV
15	11/07/2013	clutter measurements	HVHV
16	11/07/2013	clutter measurements	HVHV
17	11/23/2013	horn antenna calibration	HVHV
18	11/26/2013	corner reflector calibration	HVHV
19	11/27/2013	rain calibration bright band observation	HVHV
20	12/14/2013	winter storm	HVHV
21	02/13/2014	winter storm	HVHV

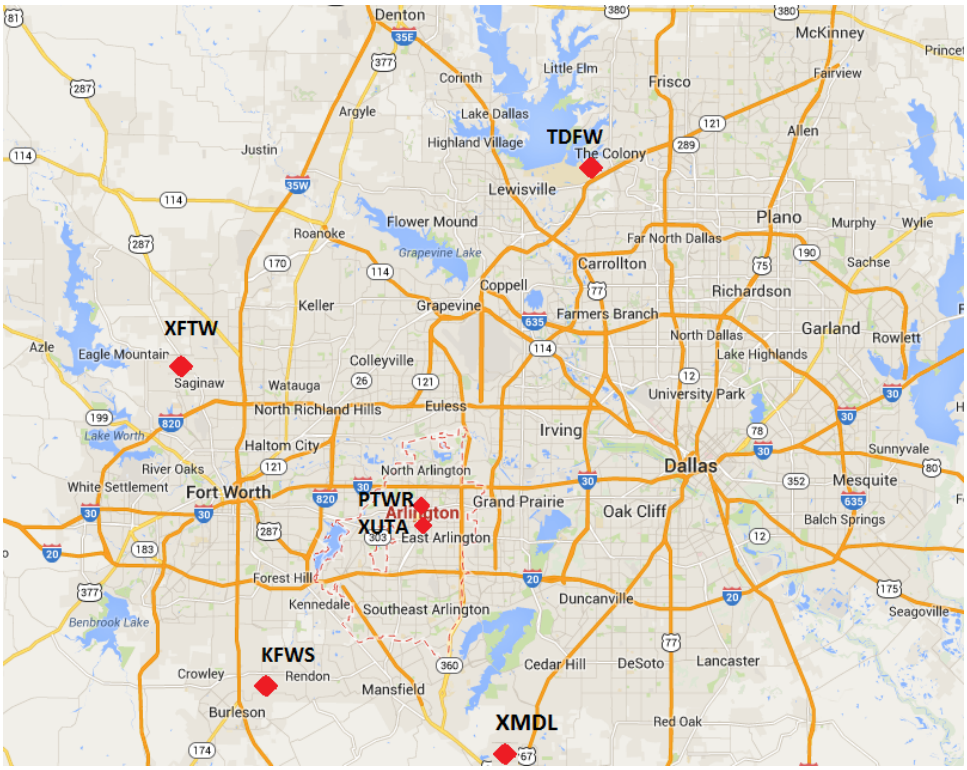

Figure 2.9. Map of the Dallas-Fort Worth area radar network during spring 2014 deployment. The PTWR was installed in direct proximity of CASA XUTA X-band radar. Additionally, the data can be compared against S-band WSR-88D radar (KFWS) located 25 km to the southwest direction, and C-band TDWR radar (TDFW) located 40 km to the northeast direction. CASA network at the time of PTWR deployment consisted of 2 additional X-band radars (XFTW and XMDL).

Table 2.3. Radar system characteristics of the PTWR, XUTA, TDWR, and NEXRAD

Parameter	PTWR	XUTA	TDWR	NEXRAD
Peak power	$60W$	$10.8kW$	$250kW$	$500kW$
Frequency	$9.36GHz$	$9.41GHz$	$5.6GHz$	$3GHz$
Beam width (az/el)	$1.8 - 2.6°/3.6°$	$1.8°$	$0.5°$	$1.25°$
Range resolution	$60m$	$60m$	$150m$	$1km$
Range coverage	$45km$	$40km$	$460km$	$460km$
PRF	$2000 - 3000Hz$	$1600 - 2400Hz$	$800 - 1120Hz$	$320 - 1300Hz$
Azimuthal resolution	$1°$	$0.5°$	$0.55°$	$1°$
Sector	$90°$	$360°/adaptive$	$360°$	$360°$
Pulse width	$20\mu s$	$0.6\mu s$	$1.1\mu s$	$1.57 - 4\mu s$
Pulse compression	yes	no	no	no

Table 2.4. Summary of data collected by PTWR in season 2014 in Arlington,TX. A collocated CASA XUTA X-band radar was operational during all deployments allowing for a qualitative and quantitative comparison.

#	**Date**	**Time UTC**	**Weather event**
1	4/3/2014	22:34-23:25	severe thunderstorm warning
2	4/4/2014	00:22-01:25	severe thunderstorm warning
3	4/8/2014	00:40-01:46	moderate rain
4	4/13/2014	15:46-17:41	light rain
5	4/27/2014	13:30-13:50	severe thunderstorm warning
6	5/8/2014	13:16-14:23	heavy rain
7	5/8/2014	19:33-21:43	severe thunderstorm warning flash flood warning tornado warning
8	5/12/2014	19:11-19:42	severe thunderstorm warning
9	5/13/2014	04:08-01:09	moderate rain
10	5/24/2014	21:29-03:12	moderate rain
11	5/25/2014	21:31-02:09	heavy rain
12	6/9/2014	12:05-13:45	moderate rain

2.5 Meteorological data examples

2.5.1 Case 1: Squall line

A major storm complex formed on 4 October 2013 over the midwestern United States. It moved eastward and produced 22 confirmed tornadoes. On 7 October 2013 a cold front passing over US East Coast initiated a line of storms spanning from North Carolina to Vermont. The PTWR performed an observation of the squall line event passing over Western Massachusetts. The radar location and parameters are presented in Table 2.5. In order to avoid a beam blockage from the surrounding hills, the radar elevation angle was set to 6 degrees. A uniform sampling at 5 kHz provided a high unambiguous velocity ($\pm$ 38 m/s) at the cost of a reduced range coverage (25 km). The closest WSR-88D radar, KENX in Albany,NY, was located around 120 km to the west away from the observation site, therefore only a limited qualitative comparison is possible.

A dataset at 21:04:39 UTC from the PTWR along with the closest scan from KENX is shown in Figure 2.10 for comparison. The location of PTWR is denoted by the black cross. A 5 km wide band of very intense precipitation in excess of 50 dBZ is visible in a reflectivity field provided by KENX. This causes a severe attenuation and a signal extinction in the reflectivity field measured by PTWR. The sensitivity of PTWR can be considerably improved by increasing the pulse duration or decreasing the chirp bandwidth. Additional improvement is promised by a multilag processing (*Lei et al.*, 2012). However, the signal extinction in heavy precipitation is unavoidable due to the shorter radar wavelength utilized by PTWR. The storm was moving fast in the direction east-northeast with an average speed of 60 km/h. The lower panel in Figure 2.10 indicates the Doppler velocities up to 30 m/s. Furthermore, a rotating structure in front of the squall line with a visible inflow can be identified.

The evolution of a low reflectivity structure in front of the squall line over the time period of 5 minutes is presented in Figure 2.11. The images shown represent

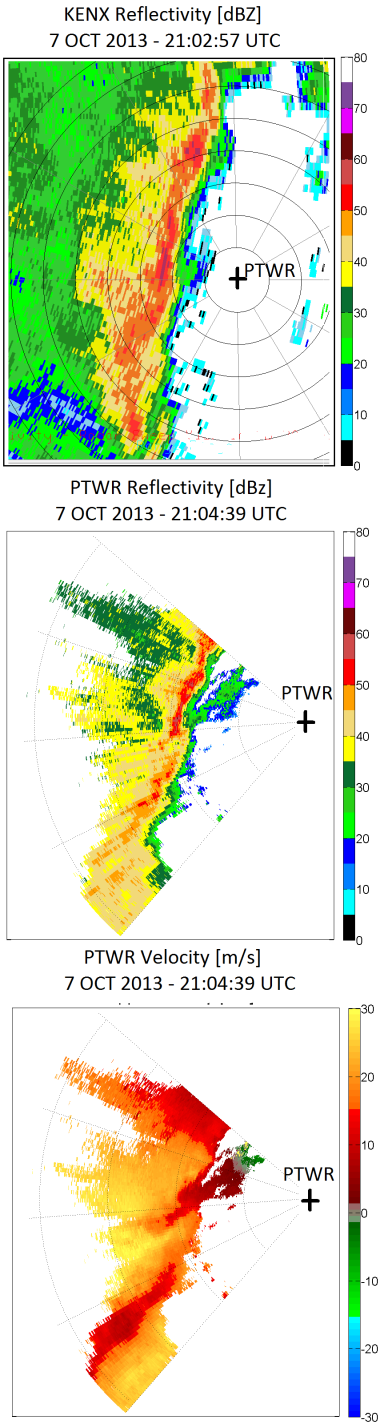

Figure 2.10. Comparison between PTWR and a nearby WSR-88D radar (KENX). PTWR measurements are significantly affected by a signal extinction when observing heavy rain ($> 40dBz$). The range rings are spaced 5km apart.

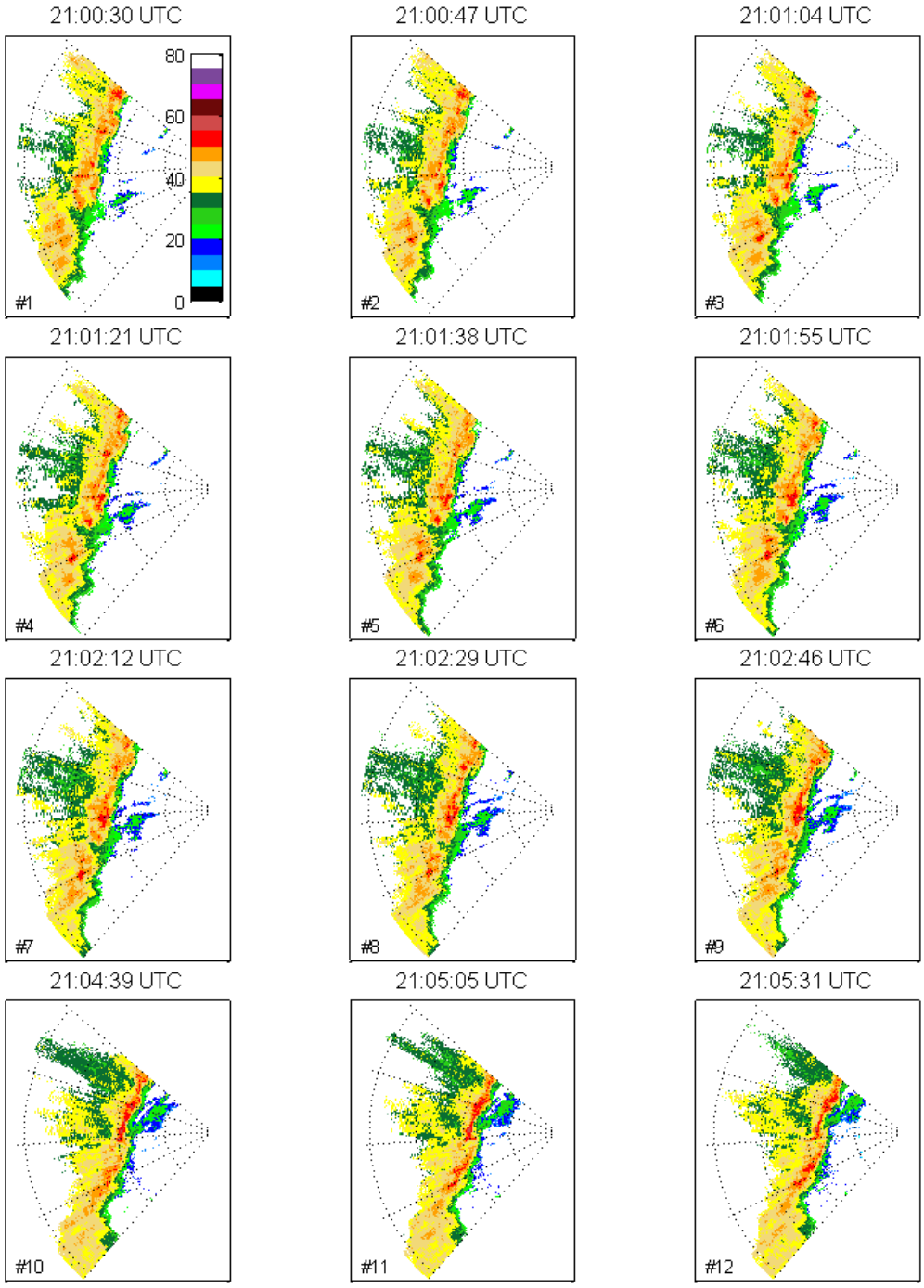

Figure 2.11. Reflectivity fields collected by PTWR at 21:00-21:05 UTC on 7 Oct 2013. A 90° PPI is collected in each scan using 91 beams. The images shown represent a decimated view of the true temporal resolution ($\Delta t = 3s$).

Table 2.5. Data collection parameters on 10/7/2013.

Parameter	Value
Latitude	$42.3417°N$
Longitude	$72.5889°W$
Bearing	$260°$
Time	20:34 - 21:24 UTC
Elevation	$6°$
Sector	$\pm 45°$
Dwell	128 pulses
PRF	uniform 5 kHz
Range	25 km
v_a	$\pm 38 m/s$
Modulation	NLFM
Pulse width	$20 \mu s$
Bandwidth	$3 MHz$

a decimated view of the true temporal resolution ($\Delta t = 3s$). Three-body scatter spikes (TBSS) are visible in multiple panels as weak reflectivity echoes that extend out from the thunderstorm. At S-band this artifact indicates presence of hailstones, while in case of C-band and X-band weather radars even large rain drops can cause a TBSS effect. The physical proximity of the PTWR results in a better spatial resolution compared with KENX despite larger antenna beamwidth. This allows for an identification of the fine details such as a thin rain curtain visible in panels #4−#9.

Moreover, the higher temporal resolution allows to monitor rapidly evolving phenomena. The same storm system produced a confirmed EF-1 tornado in Paramus, NJ, which stayed on the ground for only 2 minutes. The NWS confirmed the tornado by looking at Doppler velocity data, observations of the damage, and eyewitness reports. However, no tornado warning was issued, due to the lack of high temporal observations. This data set highlights the importance of PTWR's capability to provide rapid scan update during severe weather events.

Table 2.6. Data collection parameters on 4/4/2014.

Parameter	Value
Latitude	$32.7310°N$
Longitude	$97.1148°W$
Bearing	330°
Time	23:50 - 2:10 UTC
Elevation	$2° - 18°$
Elevation step	4°
Sector	±45°
Dwell	128 pulses
PRF	staggered 2&3 kHz
Range	45 km
v_a	$\pm 48 m/s$
Modulation	NLFM
Pulse width	$20\mu s$
Bandwidth	$3MHz$

2.5.2 Case 2: Convective rain

The PTWR performed an observation of an evening severe thunderstorm passing over Fort Worth, TX area on 3 April 2014. The radar location and parameters are presented in Table 2.6. It operated in volume scan mode, collecting data at five elevation angles between 2° and 18°. The maximum observation range was set to 45 km, while the unambiguous velocity was within ± 48 m/s using a staggered PRT technique. The radar illuminated a 90° sector facing northwest. The use of a $20\mu s/3MHz$ non-linear frequency modulated waveform resulted in a 3 km blind range and a range resolution of 60 m.

For qualitative comparison, a PPI of reflectivity collected by the Fort-Worth WSR-88D radar (KFWS) at 01:11:21 UTC and the TDWR radar (TDFW) at 01:10:59 UTC on 4 April 2014 is presented in Figure 2.12. These radars are not co-located and utilize different antennas. Hence, the reflectivity fields do not correspond to the same

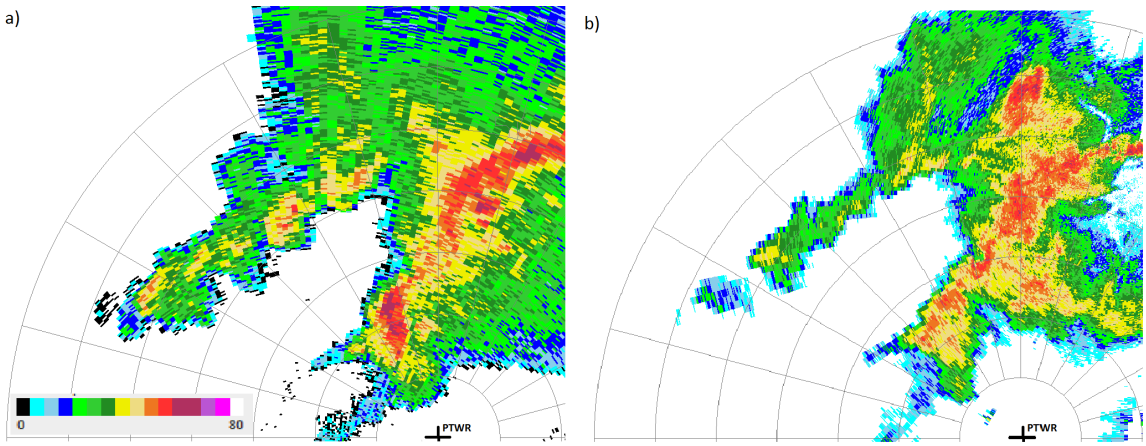

Figure 2.12. Comparison between a) the WSR-88D radar (KFWS) at 01:11:21 UTC and b) the TDWR radar (TDFW) at 01:10:59 UTC on 4 April 2014. Radars are not co-located and hence the reflectivity fields do not correspond to the same altitude. Finer spatial resolution provided by the TDWR radar is apparent. The location of the PTWR is indicated with a black cross. The range rings are spaced 10 km apart.

scattering volumes. Nevertheless, the measured reflectivity fields are roughly comparable. Both radars detected heavy precipitation in excess of 50 dBZ. Furthermore, the better spatial and range resolution provided by the TDWR radar is apparent.

To analyze the calibration accuracy and weather imaging capabilities of the PTWR, co-located measurements (in time and space) with XUTA were performed. Figure 2.13 presents radar polarimetric products generated by XUTA, while Figure 2.14 presents corresponding products generated by PTWR. There are eight panels in each figure, showing attenuation corrected reflectivity, velocity, differential reflectivity, spectrum width, normalized coherent power, signal to noise ratio, differential propagation phase, and correlation coefficient. Attenuation correction for the PTWR was performed using the relation shown in Equation 2.15 (*Frasier et al.*, 2013). *Chen and Chandrasekar* (2012) demonstrated the excellent performance of the CASA QPE system by the cross comparison with rain gauges. Hence the radar products observed by XUTA are considered as the „truth“ and used to examine the bias in PTWR. The

general comparison reveals that the storm structures illuminated by both radars are well matched. The differences between XUTA and PTWR are caused by two factors.

$$Z_{H,corr} = Z_H + 0.28\phi_{dp} \tag{2.15}$$

First, the PTWR is a solid-state low-power radar, and hence a lower SNR is to be expected. The measurements show the beam dependent SNR reduction in excess of 12 dB compared with XUTA. Due to lower sensitivity, the PTWR did not detect weak echoes seen in XUTA data between azimuth angles 0° and 15°. The sensitivity of the PTWR can be improved by the modification of waveform parameters, by either increasing pulse duration or decreasing chirp bandwidth. The quality of the correlation coefficient and spectrum width also degrades with decreasing SNR and is clearly visible in PTWR data. *Cheong et al.* (2013) has shown that this degradation can be significant in X-band solid-state weather radar and proposed a multilag moment processor, which does not utilize lag-0 auto-correlation estimates and performs well even if SNR is low (< 20 dB).

Second, the PTWR illuminates a scattering volume more than 2 times larger than XUTA due to its wide antenna beamwidth. This is particularly disadvantageous at longer ranges, where a non-uniform beam filling effect can result in lower correlation coefficient values, noisier spectrum width, and a bias in specific attenuation estimate (*Gosset and Zawadzki*, 2001). The different scattering volumes between the radars is also evident in reflectivity fields. The strong reflectivity values are underestimated, and the weak reflectivity values tend to be slightly overestimated. This stands in agreement with findings presented by *Wu and Liu* (2014), who compared observations of an X-band radar utilizing a dish antenna against a 2-D single polarized phased array radar.

A qualitative evaluation of the wide beamwidth effect on uncorrected reflectivity is presented in Figure 2.15. To simplify comparison, the XUTA data were first aver-

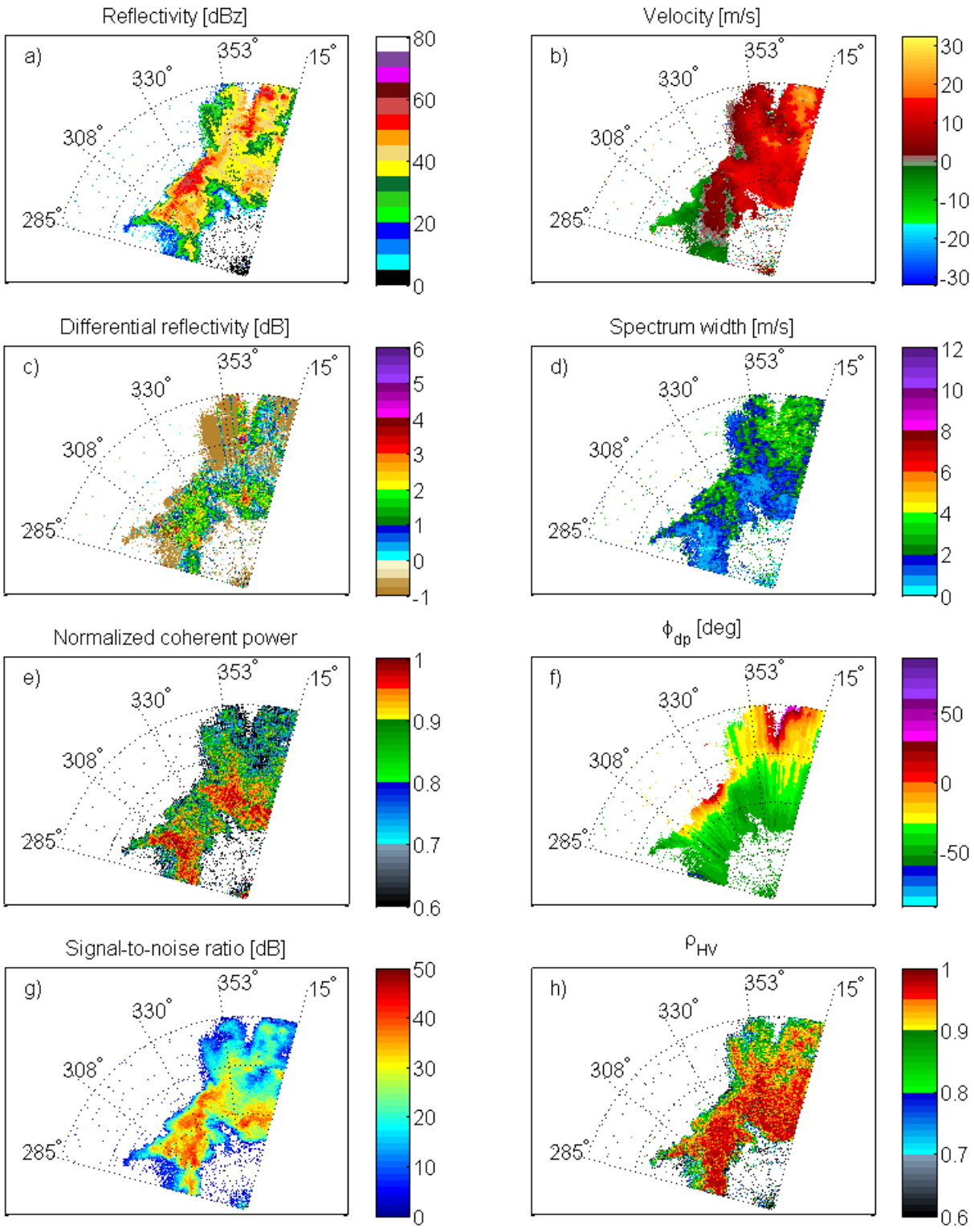

Figure 2.13. Severe weather observation by CASA XUTA radar at elevation angle 5.3° over north Fort Worth area on 4/4/2014 at 01:10:09 UTC.

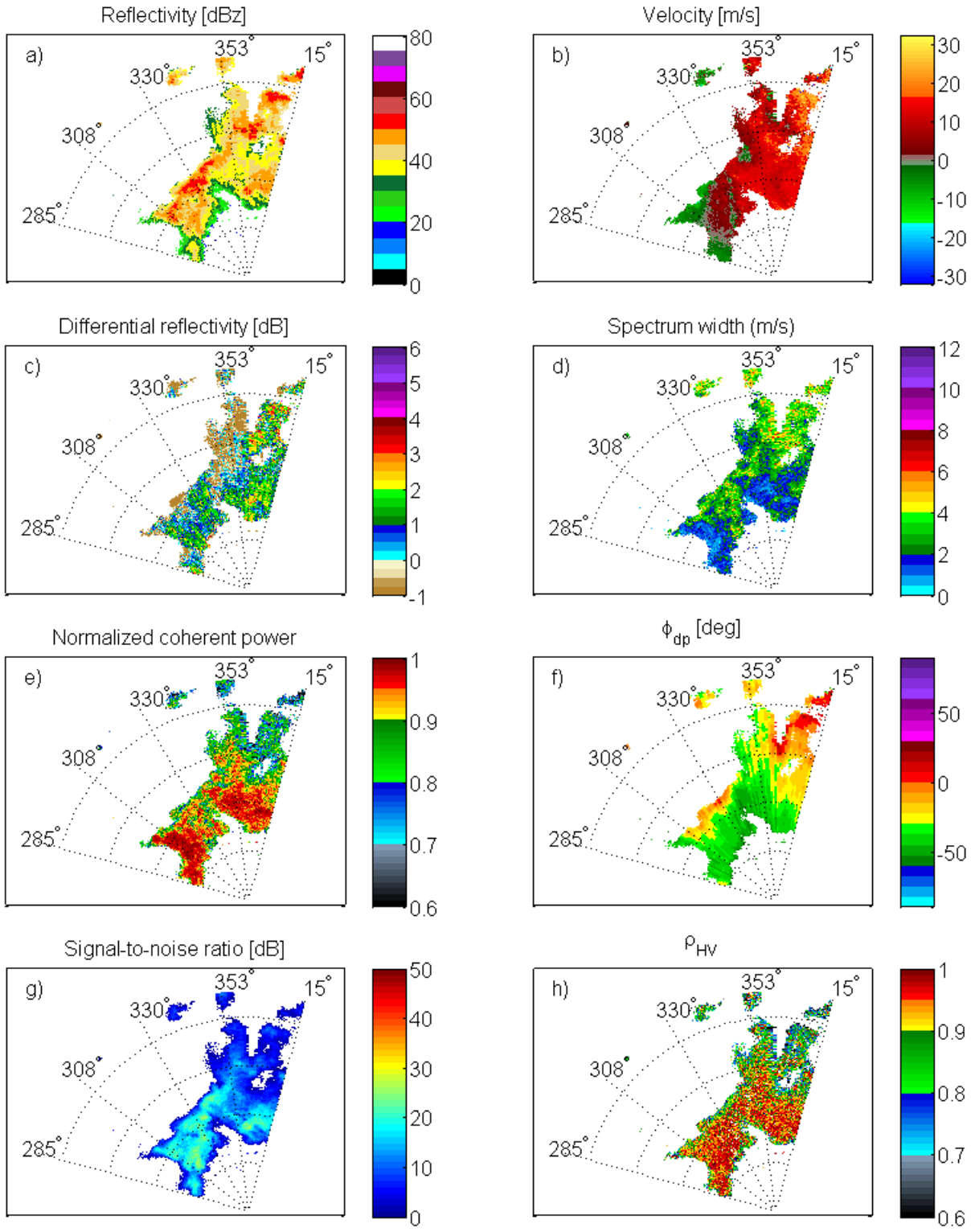

Figure 2.14. Severe weather observation by PTWR radar at elevation angle 6° over north Fort Worth area on 4/4/2014 at 01:10:07 UTC.

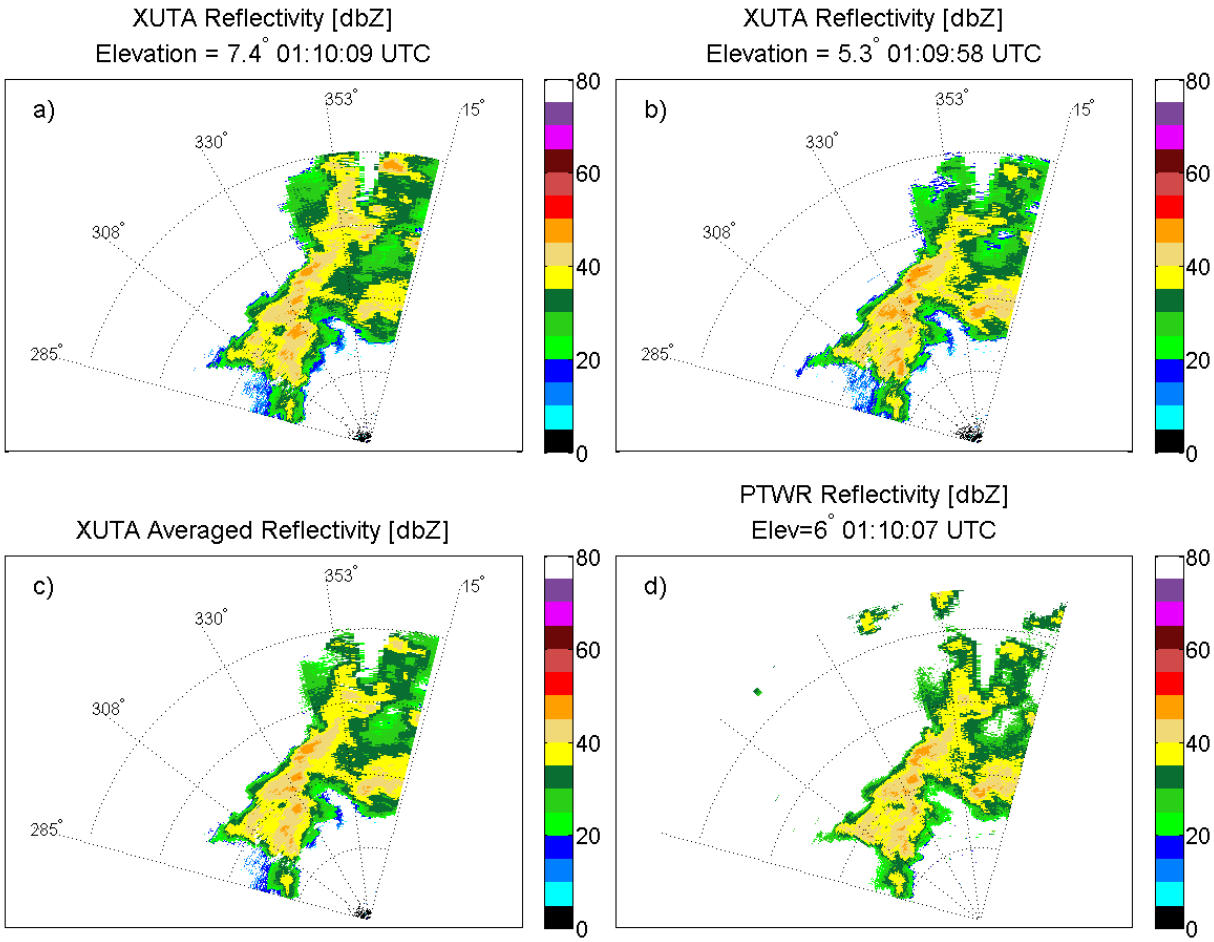

Figure 2.15. The PPI of uncorrected reflectivity by a) XUTA at an elevation angle 7.4° averaged in azimuth over 2°, b) XUTA at an elevation angle 5.3° averaged in azimuth over 2°, c) XUTA as an average of elevation angles 5.3° and 7.4°, d) PTWR at an elevation angle 6°.

aged in azimuth over 2° (panels a and b) to roughly match with PTWR azimuthal resolution. Additionally, XUTA precipitation data from two available elevations (5.3° and 7.4°) were averaged in order to obtain reflectivity field of a comparable observation volume. The averaged PPI of XUTA (Figure 2.15c) is close to that observed by PTWR (Figure 2.15d). The improvement obtained by averaging is the most visible at long-range gates, since the beam mismatch effect between XUTA and PTWR increases with range.

Figure 2.16a shows a histogram of all available observations from averaged XUTA (Figure 2.15c) and PTWR (Figure 2.15d) data, thresholded at $\mathrm{SNR_{PTWR}} = 0$ dB. These are calibrated X-band reflectivities without attenuation correction. The observations provided by both radars exhibit a high correlation coefficient of 0.90, a relative bias (XUTA/PTWR) of 0.75 dB, and a standard deviation of 2.58 dB. The less-than-unity slope of the least square fit line confirms an underestimation of higher reflectivities by PTWR. This is mostly due to the uncompensated signal attenuation. The overestimation of low reflectivities by the PTWR is a consequence of the larger antenna beamwidth and the rain reflectivity probability distribution (see Figure 2.16b). The deviation from XUTA=PTWR line increases if a non-averaged XUTA reflectivity field is used as a reference. The measurements are also affected by different calibration procedures.

To verify the observational capabilities of the new X-band dual polarization Phase Tilt Weather Radar (PTWR), co-located precipitation observations with a CASA magnetron-based radar (XUTA) were performed in the Dallas-Forth Worth Urban Demonstration Network. A qualitative comparison shows that both radars can resolve similar reflectivity structures. The experiment proved that a low-cost, low-power, electronically-scanned radar, using an alternate-transmit alternate-receive mode of operation, can detect severe weather events up to 45 km away and provide a volume update on order of 1 minute. The degradation of PTWR data quality compared

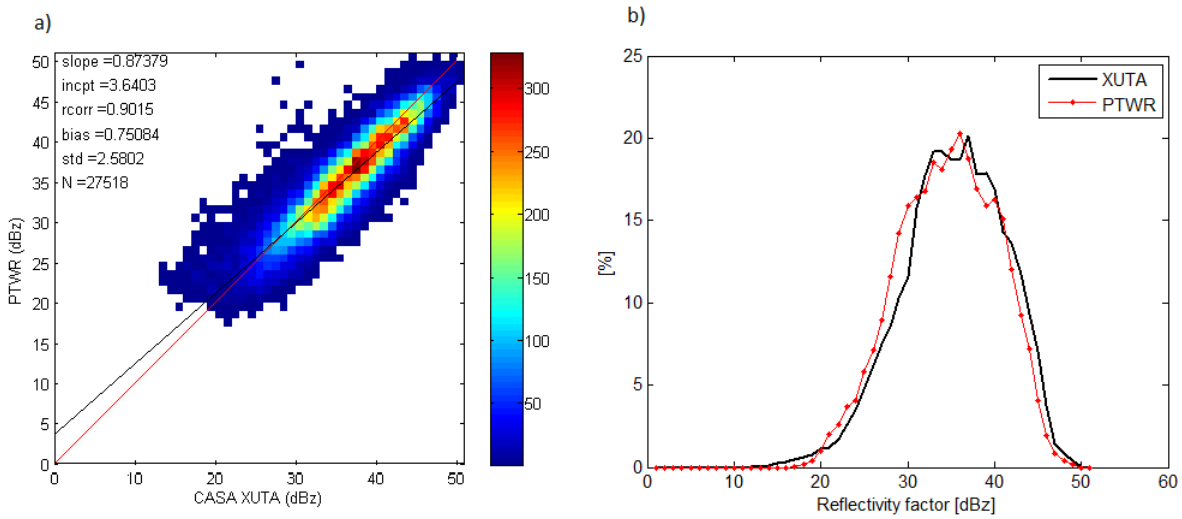

Figure 2.16. a) Histogram of uncorrected reflectivities observed over Fort Worth area by CASA XUTA and PTWR radars (Figures 2.15c and 2.15d). The black line is XUTA=PTWR and the red line is a least squares fit. An average bias over all observations is 0.75 dB. b) Corresponding probability distributions of reflectivity by XUTA and PTWR.

to XUTA radar is mostly due to a significantly lower signal to noise ratio. The techniques to mitigate this problem, such as waveform modification and multilag and spectral processing, are currently investigated. The effect of beam width mismatch on reflectivity between XUTA and PTWR was analyzed. The quantitative analysis demonstrated a high correlation coefficient between both radars, which validates the usage of solid-state radars for weather observations.

CHAPTER 3

SYSTEM CALIBRATION

3.1 Near field probe TR module calibration

In order to perform initial system characterization a near field probe setup described in detail by *Medina et al.* (2012b) was used. The measurement setup utilizes a single axis-linear positioner and an open ended waveguide as shown in Figure 3.1. The near-field probe, is positioned in front of the subarray under test (SUT), and the S_{21} parameter is measured using a network analyzer operated at the RF frequency. Each SUT is fed by an independent TR module, which utilizes a 6-bit phase shifter and a 6-bit digital attenuator. Hence, in order to fully characterize the SUT, 4096 states should be measured. The number of measurements is significantly reduced using the following procedure. First, with the attenuator in the zero state, the phase shifter is switched through all possible states. Similarly, with the phase shifter in the zero state, the digital attenuator is switched through all possible states. As a consequence, only 128 measurements per SUT are performed. The remaining 3968 states are then derived using following formula:

$$S_{21}^{m}(n, att, phs) = \frac{S_{21}^{m}(n, att, 0) S_{21}^{m}(n, 0, phs)}{S_{21}^{m}(n, 0, 0)} \tag{3.1}$$

where m represents the mode of operation (TxH, TxV, RxH, RxV), n is the number of utilized TR module, *att* and *phs* are the attenuator and phase shifter states. n, *att* and *phs* are in range (0,1,2,..,63).

The typical performance of a single TR module measured at 9.36 GHz is shown in Figure 3.2. Figure 3.2a shows gain performance versus attenuator and phase shifter

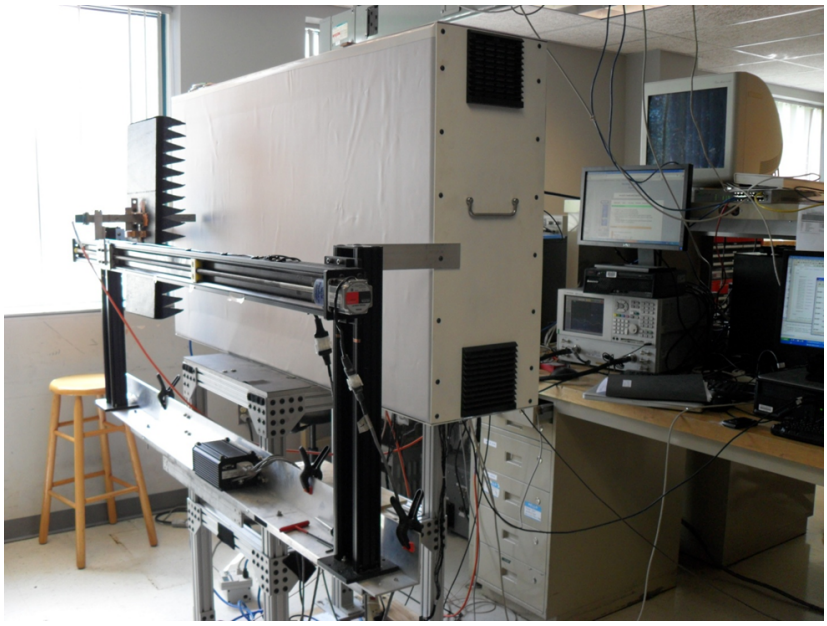

Figure 3.1. Near field probe measurement setup.

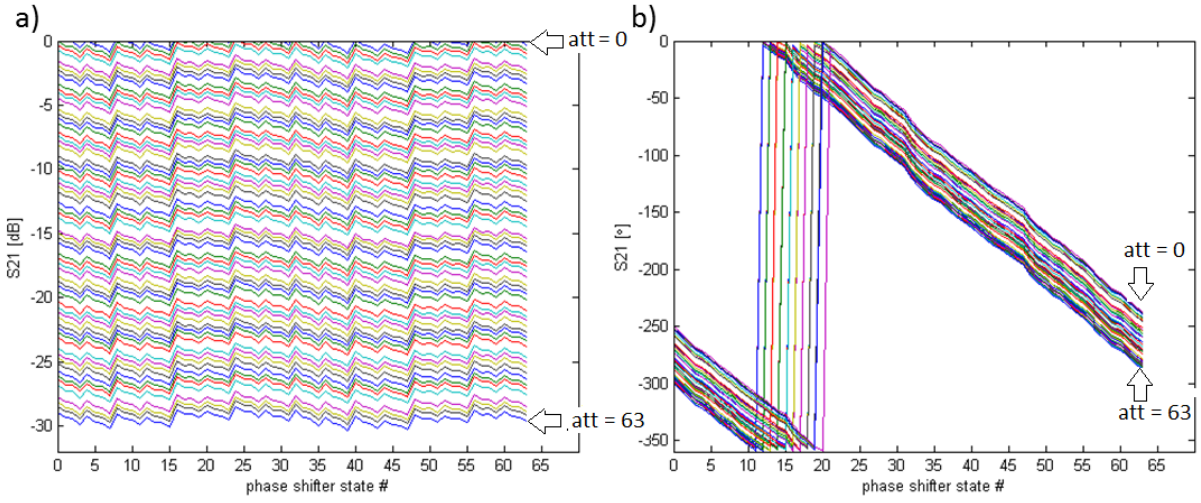

Figure 3.2. Single TR module RF performance in *RxH* mode of operation. a) Gain performance versus attenuator and phase shifter state. b) Phase performance versus attenuator and phase shifter state.

state. The phase shifter insertion loss varies within $\pm 1dB$ and exhibits a repeatable pattern when switched over all 64 states. Furthermore, as shown in Figure 3.2b, the digital attenuator introduces additional phase shift, which can be as high as 50° when switched over all 64 states. This effect is illustrated in detail in Figure 3.3a, that presents the average measured phase of S_{21} over all available digital attenuator states. There is an identifiable pattern, which repeats every 8 states. On average the phase shift between two consecutive attenuator states is much smaller than the phase step of a phase shifter. This can be beneficial in order increase the effective phase shifter resolution.

The average measured phase of S_{21} over all available phase shifter states is presented in Figure 3.3b, where the digital attenuator was set to zero state . The measured data present a linear phase progression with a measured mean phase step of 5.62° as expected. Note that phase shifter states 16, 48 and 64 exhibit a large phase shift error in excess of 3.5°. This periodic error could result in the antenna performance deterioration, since the effects of errors which are correlated from element to element tend to be more severe compared with the effects of random errors (*Carlson et al.*, 1990). However, the data presented here does not include the phase shift due to power divider and feed lines, which is dependent on the TR module location within the antenna array. Thus observed imperfections should be of no concern.

The measured gain performance of 64 TR modules over all available phase shifter states is presented in Figure 3.4, where the digital attenuator was set to zero state. The measured data were normalized to the TR module characterized by the lowest gain S_{21MIN}. The measured absolute gain can vary by $2dB$ between two TR modules. On the other hand, a consistent trend over phase shifter states can be observed. Note that in order to implement Taylor amplitude distribution to the antenna pattern in the receive mode of operation, only digital attenuator states with $S_{21} < S_{21MIN}$ are permitted, which results in a reduced receiver gain.

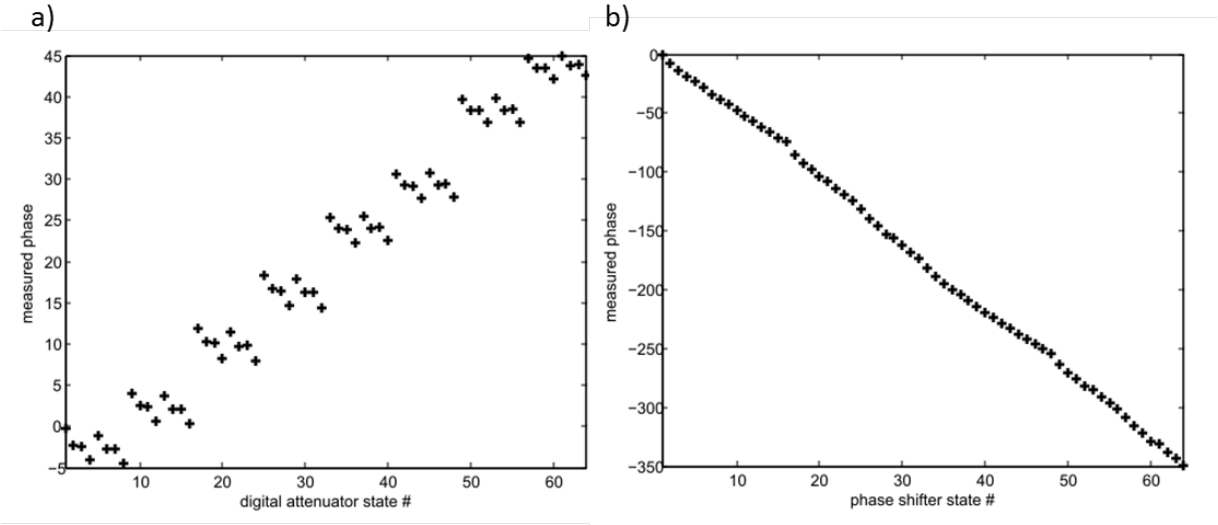

Figure 3.3. Measured TR module phase response averaged over all 64 TR modules. a) Phase shifter set to state zero. b) Digital attenuator set to state zero.

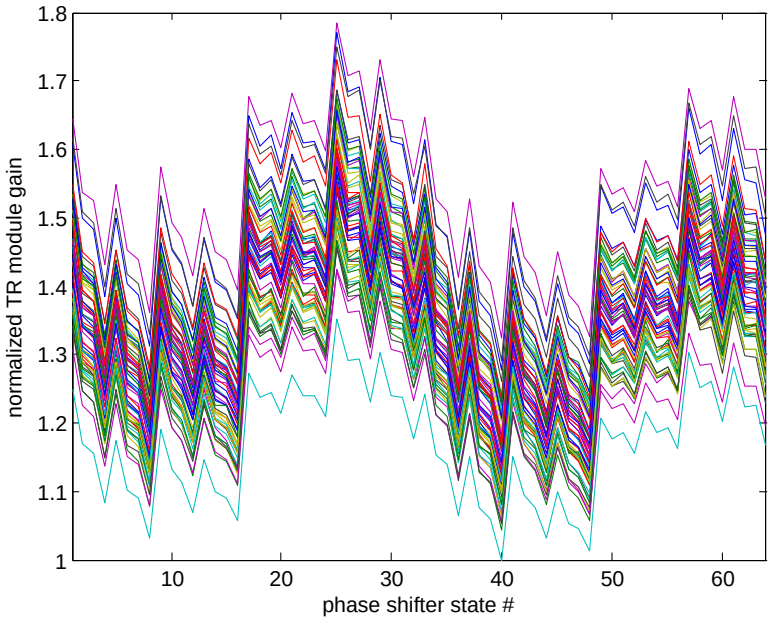

Figure 3.4. Measured gain performance of 64 TR modules (H-channel receivers) versus phase shifter state. Digital attenuator was set to state zero.

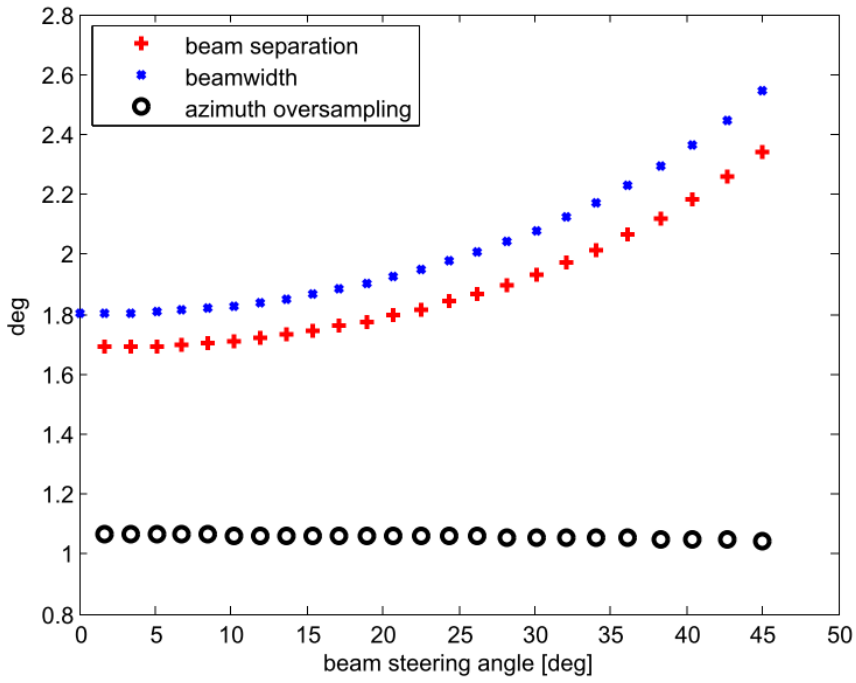

Figure 3.5. Beam steering capability using a 6-bit phase shifter (theoretical performance).

3.1.1 Beam steering capability

The phase increment $\Delta\phi$ between two successive elements for a given beam steering angle θ_s is constant and is defined as:

$$\Delta\phi = \frac{2\pi d \sin(\theta_s)}{\lambda} \tag{3.2}$$

where:

d - distance between the radiating elements. For PTWR $d = 0.17mm = 0.53\lambda$.

θ_s - beam steering angle

$\Delta\phi$ - phase increment in radians

The PTWR utilize 6-bit phase shifters (HMC642LC5 from Hittite), which provide a 5.625° phase step. According to (3.2), in order to set the beam direction to 1°

away from broadside, the phase increment should be 3.33°. This phase increment is smaller than the phase shifter step. However, a 6-bit digital attenuator (HMC424 from Hittite) provides an additional phase shift between two consecutive attenuation steps on order of 2.4°. Therefore using a combination of phase shifter and attenuator settings, a requested phase increment can be set.

Equation (3.2) can be rewritten in order to compute the beam steering angles θ_s (in degrees) which can be achieved using just the 6-bit phase shifter:

$$\theta_s = \arcsin\left(\frac{n5.625\lambda}{360d}\right) \tag{3.3}$$

where $0 \leq$ n $\leq$ number of phase shifter steps.

In this theoretical case, beam separation, defined as a difference in beam direction between two consecutive beams, increases from 1.69° at broadside to 2.34° at $\theta_s = 45°$. Further, the $3dB$ antenna beamwidth ϕ_{3dB} depends on steering angle. The effect of beam broadening can be approximated as in (3.4), which compensates for the increase in beam spacing. Hence the azimuth oversampling, defined as a ratio of beamwidth and beam separation, is almost constant in beam steering range ±45° at a level of 1.05 (see Figure 3.5).

$$\phi_{3dB}(\theta_s) = \frac{\phi_{3dB}(\theta_0)}{\cos(\theta_s)} \tag{3.4}$$

The digital attenuator enhances the effective phase setting capabilities. Therefore implementation of beam steering resolution close to 1° can be achieved. Figure 3.6 presents theoretical and applied array factor (based on near field probe calibration measurements) at the scan angle $\theta_s = 1°$ using a Taylor $25dB$ amplitude distribution. The root-mean square error of applied phase coefficients is 1.51° and for amplitude it is $0.26dB$ (see Figure 3.6b and c). Note that due to phase and amplitude imbalance there exists random peak sidelobes in range between 30 and 40 dBc. Locations of

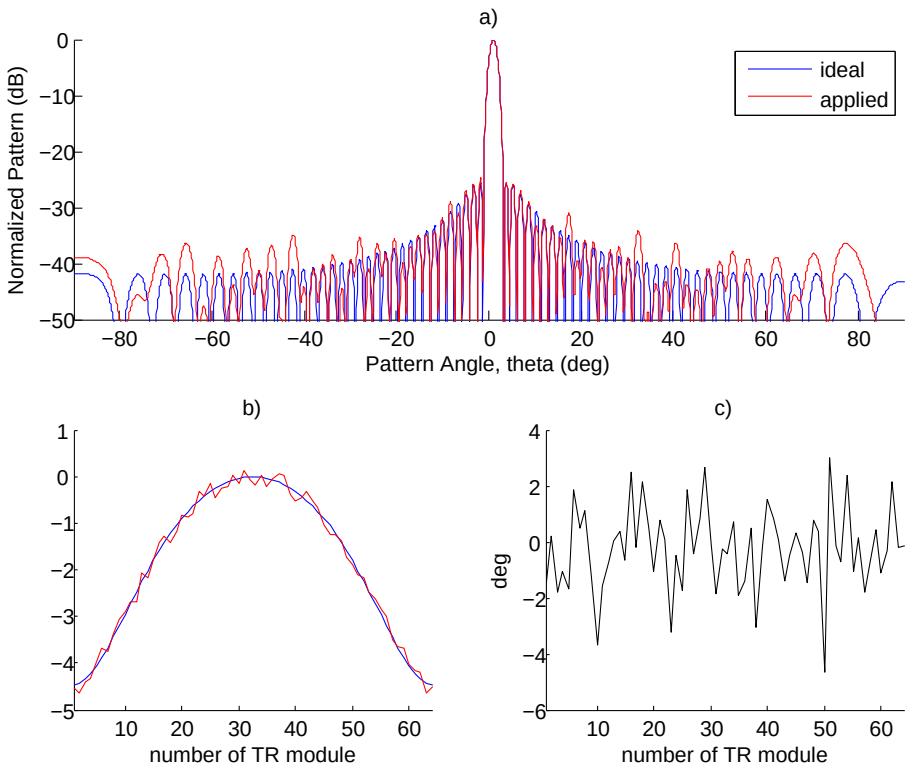

Figure 3.6. a) Theoretical and applied array factor at steering angle $\theta_s = 1°$. Note random peak sidelobes due to amplitude (b) and phase (c) misalignment. Figure c) shows the difference between required and applied phase.

the peak sidelobes depend on the steering angle θ_s and the radar mode of operation. The level of these sidelobes sets the limit of the achievable array pattern control by means of a tapered amplitude distribution.

3.1.2 TR module short term stability and temperature drift effect

The average sidelobe level in an array in terms of the independent element errors is defined as (*Mailloux*, 2005):

$$\overline{\sigma^2} = \frac{[(1-P) + \overline{\phi^2} + \overline{\delta^2}]}{P\epsilon_T} \tag{3.5}$$

where

$\overline{\sigma^2}$ - average sidelobe level normalized to the main beam peak

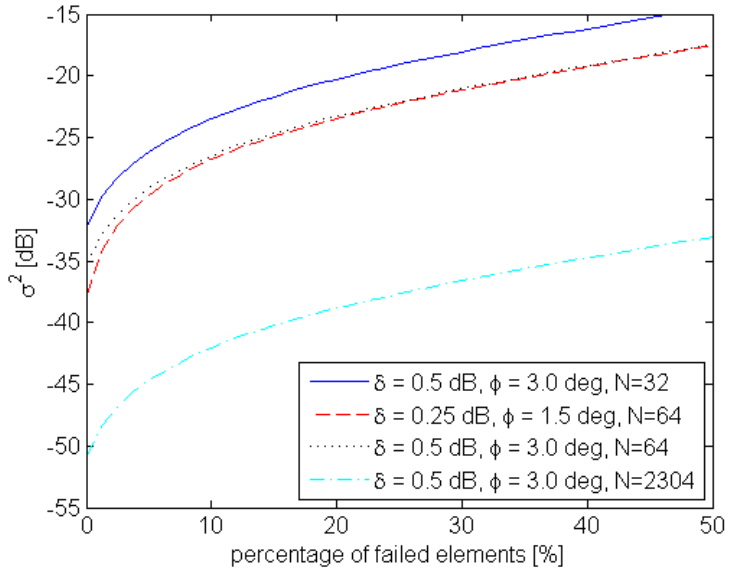

Figure 3.7. Average sidelobes due to random phase and amplitude errors as a function of number of failed elements. Taylor 25 dB taper is applied.

ϕ - RMS phase error in radians

δ - RMS amplitude error in Volts/Volt or RMS amplitude error in $dB/8.686$

N - total number of radiating elements

P - probability of elements operating properly $= 1 - N_F/N$ where N_F is number of failed elements

ϵ_T - array taper efficiency

The average sidelobe level $\overline{\sigma^2}$ due to random phase and amplitude errors as a function of number of failed elements is presented in Figure 3.7. It is evident that increasing the size of an array results in the lower value of $\overline{\sigma^2}$. The effect of failing elements on $\overline{\sigma^2}$ is very prominent for P in range 0.9 - 1. In this case an increase in $\overline{\sigma^2}$ up to 10 dB compared with an ideal array performance can be observed. The average sidelobe level $\overline{\sigma^2}$ for PTWR assuming $\phi = 1.5°$ and $\delta = 0.25dB$ is expected to be worse than -35 dB.

Table 3.1. Short term TR module stability. The standard deviation of phase and amplitude oscillations based on data measured over $60s$.

$\sigma\|S21_{Tx}\|[dB]$	$\sigma\|S21_{Rx}\|[dB]$	$\sigma(\angle S21_{Tx})[^\circ]$	$\sigma(\angle S21_{Rx})[^\circ]$
0.07	0.01	0.35	0.09

In order to estimate the average antenna side lobe level, the short term stability of TR modules should be considered. The standard deviation of phase and amplitude oscillations based on data measured over 60 seconds is presented in Table 3.1. The magnitude of the derived parameters is very low and hence the influence of short time stability on averaged antenna side lobe level can be neglected.

Measurements revealed that internal TR module temperature significantly influence RF performance. An amplitude drift as high as $0.1dB/^\circ C$ and a phase drift on order of $0.5^\circ/^\circ C$ can be expected in the transmission mode. It is assumed that the drift characteristic can be considered identical for all TR modules and that the error caused by thermal drift, denoted as $De^{j\delta}$, for the TR module under test is common for all combinations of digital attenuator and phase shifter. Consider that all transmission calibration coefficients measured at calibration temperature T_{cal} are defined in a matrix $X_k(T_{cal})$, where index k indicates number of the TR module. Then in theory, the calibration matrix at temperature T_{dep} can be modified as follows:

$$X_k(T_{dep}) = D_{T_{dep}} e^{j\delta_{T_{dep}}} X_k(T_{cal}). \tag{3.6}$$

However, this method is difficult to implement for number of reasons:

1. The array temperature drift should be characterized in temperature range $-30^\circ C$ to $50^\circ C$. It cannot be guaranteed that these characteristics will remain valid once the radar is fielded.

2. Currently, the TR module temperature sensors have a resolution of $1^\circ C$.

3. Temperature distribution across TR modules is not constant and hence multiple correction factors are required.

The importance of thermal drift correction is addressed now. First consider an ideal case that the thermal drift in all TR modules is identical. Since for phased array systems only relative phase shift between TR modules is of concern, hence the phase drift due to temperature does not influence system's performance. In this case a single correction factor due to reduction in transmitted power would be required. However, no degradation in beam pointing accuracy or increase in averaged sidelobe level would be observed. Next consider a situation when thermal drift between TR modules varies due to internal temperature differences and deviations in analog components. Again a single correction factor due to reduction in transmitted power is required. Using an amplitude drift coefficient of $0.1dB/^{\circ}C$ and phase drift coefficient of $0.5^{\circ}/^{\circ}C$ an array factor analysis has been performed. For $T_{dep} = T_{cal} + 5^{\circ}C$, and uniform temperature distribution within $\pm 2^{\circ}C$ (typical for PTWR), a minimal increase in the sidelobe level (below $40dBc$) far from main lobe was observed. This is not significant compared with the random peak sidelobes caused by phase and amplitude misalignment as shown in previous section. Moreover, PTWR uses a common receiver and transmitter for both polarization channels and thus it can be assumed that the relative degradation in RF performance due to temperature drift does not affect polarimetric product generation. To sum up, the main disadvantage due to thermal drift is the reduction in a signal gain, which can cause bias in reflectivity measurements. *Medina-Sanchez* (2013) reports that a two-way gain variation of 3.64 dB is possible if the temperature is varied from $0^{\circ}C$ to $52^{\circ}C$ for the current PTWR hardware architecture. Hence it is recommended to purchase an air-conditioning unit in order to keep deployment temperature constant ($T_{dep} = T_{cal}$) especially if year-round operation is taken into consideration. This would ensure constant transmitted power and significantly reduce complexity of array calibration.

3.2 Mutual coupling calibration

Phased array systems are initially characterized using external far-field or near-field sources. These methods provide the required calibration accuracy, but can be expensive and time-consuming to implement. Additionally, external calibration sources might appear impractical to use in an operational system. For example, the corner reflector located in the vicinity of a phased array antenna would be visible only for a single beam location, unless the radar system is using an additional calibration pedestal. Therefore an in-field calibration method based on a well established mutual coupling technique (*Aumann et al.*, 1989) is proposed. The only requirement to implement this technique is the ability to simultaneously transmit and receive using only 2 TR modules. The calibration method described by *Shipley and Woods* (2000) presumes that the mutual coupling between pairs of adjacent elements is invariant to their position. However, this is only valid in case of large arrays. PTWR is utilizing patch antennas, which launches varying surface wave modes depending on column location within an array. A solution to this problem was proposed by *Fulton and Chappell* (2009), who demonstrated a successful calibration procedure using a $4x4$ linearly polarized stacked patch antenna array at S-band.

3.2.1 Large array case

First, consider a large array without surface waves (see Figure 3.8). Each TR module is capable of both transmitting and receiving. Here $C_{k,k+1}$ denotes a free space mutual coupling and $C'_{k,k+1}$ is the measured complex value, which includes the free space mutual coupling and attenuation due to feed lines as well as gain provided by TR module. (k,k+1) index defines TR module number in Tx- and Rx-mode respectively. If the element patterns are symmetrical then the mutual coupling between adjacent modules is:

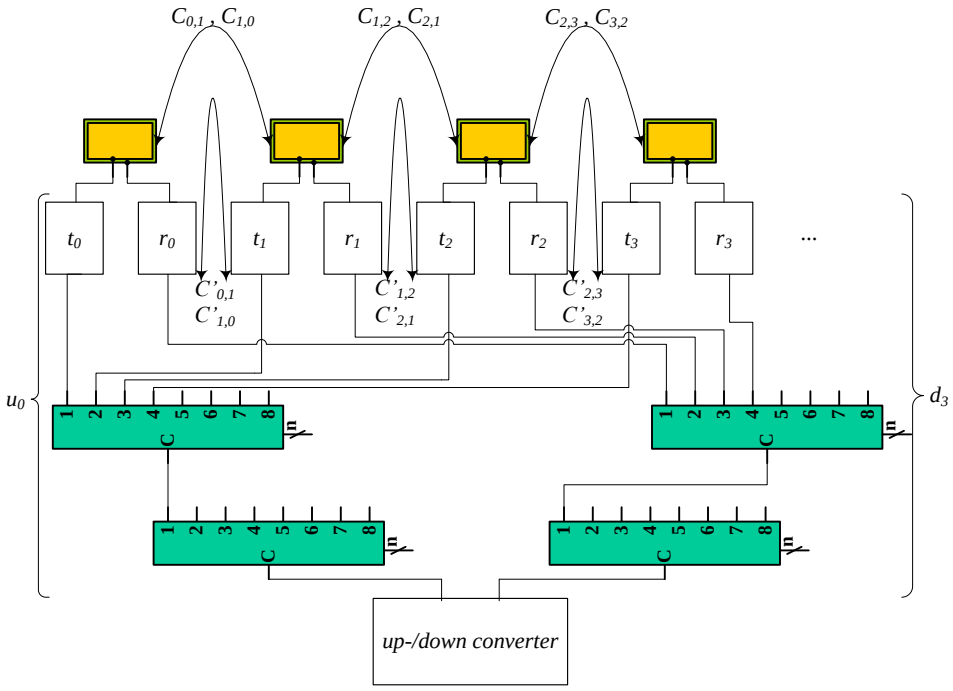

Figure 3.8. Free space mutual coupling and transfer function which includes free space coupling and feed line/module effects.

$$C_{k+1,k} = C_{k+1,k+2} \tag{3.7a}$$

$$C_{k,k+1} = C_{k+1,k} \tag{3.7b}$$

However, due to non-identical RF characteristics of TR modules:

$$C'_{k+1,k} \neq C'_{k+1,k+2} \tag{3.8}$$

Further, following procedure described by *Aumann et al.* (1989), $C'_{k+1,k}$ and $C'_{k+1,k+2}$ can be expressed as:

$$C'_{k+1,k} = t_{k+1}[i]u_{k+1}C_{k+1,k}r_k[j]d_k \tag{3.9}$$

$$C'_{k+1,k+2} = t_{k+1}[i]u_{k+1}C_{k+1,k+2}r_{k+2}[j]d_{k+2} \tag{3.10}$$

where:

- $t_{k+1}[i], r_k[j]$ are the contribution of the phase shifter and attenuator of the (k+1)-th transmitter and of the (k)-th receiver in the i-th and j-th state, respectively.

- u_{k+1}, d_{k+2} are the contribution of the feed lines, connectors and power dividers as well as phase shifter and attenuator in the zero state (i=0, j=0) in the up- and down- converter. We assume here that even if the u_{k+1}, d_{k+2} RF response changes due to the temperature drift or aging of TR modules, it affects all phase shifter and attenuator states of the TR module under test by an identical offset from the reference point.

Now, define a quantity $R[s]_{k,k+2}$ as a ratio of (3.9) and (3.10)[1]:

$$R[s]_{k,k+2} = \frac{C'_{k+1,k}}{C'_{k+1,k+2}} = \frac{t_{k+1}[i]u_{k+1}C_{k+1,k}r_k[j]d_k}{t_{k+1}[i]u_{k+1}C_{k+1,k+2}r_{k+2}[j]d_{k+2}} \tag{3.11}$$

Using (3.7a) and setting k^{th}, $(k+1)^{th}$ and $(k+2)^{th}$ TR modules to zero state equation (3.11) reduces to:

$$R[0]_{k,k+2} = \frac{d_k}{d_{k+2}} \tag{3.12}$$

The quantity $R[0]_{k,k+2}$ applied to the receiver of (k+2)th TR module, makes the signal received by this element look like the signal received by kth element. Furthermore, a similar procedure to that described above can be applied to perform transmitter calibration. The calibration offset $T[s]_{k,k+2}$ can be then defined as:

$$T[s]_{k,k+2} = \frac{C'_{k,k+1}}{C'_{k+2,k+1}} = \frac{t_k[i]u_kC_{k,k+1}r_{k+1}[j]d_{k+1}}{t_{k+2}[i]u_{k+2}C_{k+2,k+1}r_{k+1}[j]d_{k+1}} \tag{3.13}$$

which in zero state reduces to:

---

[1]Note that quantity $R[s]_{k,k+2}$ defines the cumulative change in RF performance of modules k and k+2.

$$T[0]_{k,k+2} = \frac{u_k}{u_{k+2}} \tag{3.14}$$

It should also be clear by now that based on the measured values of $R[0]_{k,k+2}$, one should be able to identify a defect in the TR module under test. For example, if value of $R[0]_{2,4}$ changes significantly since the last calibration process, it will mean that either the 2^{nd} or 4^{th} receiver or 3^{rd} transmitter has changed. Now, if $R[0]_{0,2}$ and $R[0]_{4,6}$ conform with previous measurements, then it will indicate that 3^{rd} transmitter has changed. Further, if $R[0]_{0,2}$ is comparable with the previous calibration measurement, but $R[0]_{4,6}$ is not, then it will indicate a malfunction in the 4^{th} receiver. This method can be implemented as a basic system health check test.

3.2.2 Small array case

Consider now a small array in the presence of surface waves. Here, the expression defined in equation (3.7a) does not hold anymore. The initial coupling values between TR modules $C_{m,n}$ in the zero state (i=0, j=0) are defined as in (3.15):

$$C_{m,n} = \frac{C'_{m,n}}{u_m d_n} \qquad \text{for } 1 < m, n < N \quad \text{and} \quad m \neq n \tag{3.15}$$

Here u_m and d_n are measured during initial external calibration performed in an anechoic chamber[2]. $C'_{m,n}$ denotes a coupling value using internal calibration circuit and is measured right after external calibration is completed. N is the number of TR modules. $m(m-1)$ measurements are required to fully describe the mutual coupling characteristic of the phased array under test expressed in (3.16). Note that diagonal elements of C matrix are not defined.

[2]A waveguide probe can also be used to perform initial external calibration.

$$C = \begin{bmatrix} C_{1,1} & \cdots & C_{1,N} \\ \vdots & \ddots & \vdots \\ C_{N,1} & \cdots & C_{N,N} \end{bmatrix} \tag{3.16}$$

It is assumed here that the physical antennas themselves do not change over time[3] nearly as much as the active subsystems of TR modules (*Fulton and Chappell*, 2009). Hence the created C matrix can be used as a reference calibration set. It enables monitoring of system health and, ideally, phase and amplitude misalignment compensation, which is the aim of the in-field self calibration procedure.

The calibration concept described in the previous subsection is valid only for adjacent modules. For arbitrary receive modules and common transmit modules equations (3.9) and (3.10) can be rewritten as:

$$C'_{m,n} = t_m[i] u_m C_{m,n} r_n[j] d_n \tag{3.17}$$

$$C'_{m,l} = t_m[i] u_m C_{m,l} r_l[j] d_l \tag{3.18}$$

The receiver correction factor $R[0]_{n,l}$ can be then expressed as:

$$R[0]_{n,l} = \frac{C'_{m,n}/C_{m,n}}{C'_{m,l}/C_{m,l}} = \frac{d_n}{d_l} \tag{3.19}$$

Note that the contribution of the utilized transmitter is canceled out in computation of $R[0]_{n,l}$. Hence, it is possible to use a subset of transmitters in the array in order to reduce the uncertainty in the calculation of $R[0]_{n,l}$ by averaging. The number of available transmitters depends on the signal-to-noise ratio. $R[0]_{n,l}$ is then defined as follows:

[3]However, it is recommended to repeat external calibration each time radome or antenna panel is relocated.

$$R[0]_{n,l} = \frac{1}{N-2} \sum_{m=1}^{N} \frac{C'_{m,n}/C_{m,n}}{C'_{m,l}/C_{m,l}} \qquad m \neq n \wedge m \neq l \tag{3.20}$$

Similarly, transmitter correction factor $T[0]_{n,l}$ can be defined as:

$$T[0]_{n,l} = \frac{C'_{n,m}/C_{n,m}}{C'_{l,m}/C_{l,m}} = \frac{u_n}{u_l} \tag{3.21}$$

A more precise measurement of $T[0]_{n,l}$ can be obtained by averaging measurements over a subset of receivers:

$$T[0]_{n,l} = \frac{1}{N-2} \sum_{m=1}^{N} \frac{C'_{n,m}/C_{n,m}}{C'_{l,m}/C_{l,m}} \qquad m \neq n \wedge m \neq l \tag{3.22}$$

The next step in calibration process involves the selection of a reference transmitter and receiver. There are many options to choose. For example, if an optimal amplitude calibration[4] is required, one should choose r_{ref} receiver with minimum gain or t_{ref} transmitter with the minimum transmitted power, which can be defined as follows:

$$r_{ref} = r_n \quad if \quad R[0]_{n,l} = \min R[0]_{k,l} \qquad 1 < k < N \quad \wedge \quad l = const \tag{3.23}$$

$$t_{ref} = t_n \quad if \quad T[0]_{n,l} = \min T[0]_{k,l} \qquad 1 < k < N \quad \wedge \quad l = const \tag{3.24}$$

Once the reference transmitter and receiver are selected, a set of correction factors for a beam location at broadside can be computed from equations (3.20) and (3.22). The above described method can be simply modified to determine $R[s]_{n,l}$ and $T[s]_{n,l}$,that is, correction factors in the s-th state relative to the zero state.

[4]at the cost of maximum reduction in transmitted power

3.2.3 Assessment of phased array calibration using mutual coupling technique

The mutual coupling measurement utilizes only 2 modules at a time and operates in simultaneous transmission and reception mode. The remaining 62 modules are set in the off state. This is principally different from normal radar operation where all TR modules are always active and switch simultaneously between transmit and receive modes. In consequence, two system issues have to be taken into consideration.

First, the radar system is affected by limited isolation between the high power transmitter (P_{Tx} = +40 dBm at the input to the power divider network) and the highly sensitive receiver (P_{Rxmin} = -103 dBm). Therefore, care has to be taken to assure that the measured calibration signal level is significantly higher than that of an unwanted internal RF leakage. The former can be significantly reduced by additional cable/connector shielding with copper tape and proper reduction of transmitted signal power at IF frequency. This can be applied at no cost when receivers are calibrated, since reference transmitting modules are not required to operate in saturation mode.

Second, each individual TR module in Tx mode of operation transmits RF power at +30 dBm, while the 1 dB compression point of the first stage low noise amplifier utilized in TR module receiver path is at -15 dBm. The coupling level between adjacent array columns is around 25 dB. The result is that, the RF power coupled to the receiver can permanently damage the LNA in the module under test. On the other hand, due to the small size of the array (only 64 modules), in order to guarantee uniform measurement configuration (e.g. SNR, number of averaged measurements over different TR modules combinations, etc.), it is practical to use only adjacent columns.

This issue in receiver calibration mode is solved by reducing digital transceiver transmitted power by factor of 24 dB. While in transmitter calibration mode the additional signal attenuation is obtained by receiving on the orthogonal polarization.

Table 3.2. TR module states under test during system health check control using the mutual coupling technique.

beam ID	attenuator state		phase shifter state	
1	0	000000	0	000000
2	0	000000	1	000001
3	0	000000	2	000010
4	0	000000	4	000100
5	0	000000	8	001000
6	0	000000	16	010000
7	0	000000	32	100000
8	0	000000	63	111111
9	0	000000	0	000000
10	1	000001	0	000000
11	2	000010	0	000000
12	4	000100	0	000000
13	8	001000	0	000000
14	16	010000	0	000000
15	32	100000	0	000000
16	63	111111	0	000000

The polarization switch located in the front-end of each TR module provides around 45 dB isolation. This ensures that received RF test signal is well below P_{1dB} even in the case of transmitting on adjacent module.

The process of mutual coupling based calibration involves 16 measurements per module and radar mode of operation. States under test are defined in Table 3.2. In order to test a single TR module over all possible states of phase shifter and attenuator, 4096 measurement would be necessary. Instead, only individual bits in each phase shifter and attenuator as well as their respective first and last states are measured. This provides a flexible tool to quickly (on order of 5 minutes) test performance of all TR modules in the system. The typical measurement is shown in Figure 3.9 where the first 8 states test the phase shifter, followed by an additional

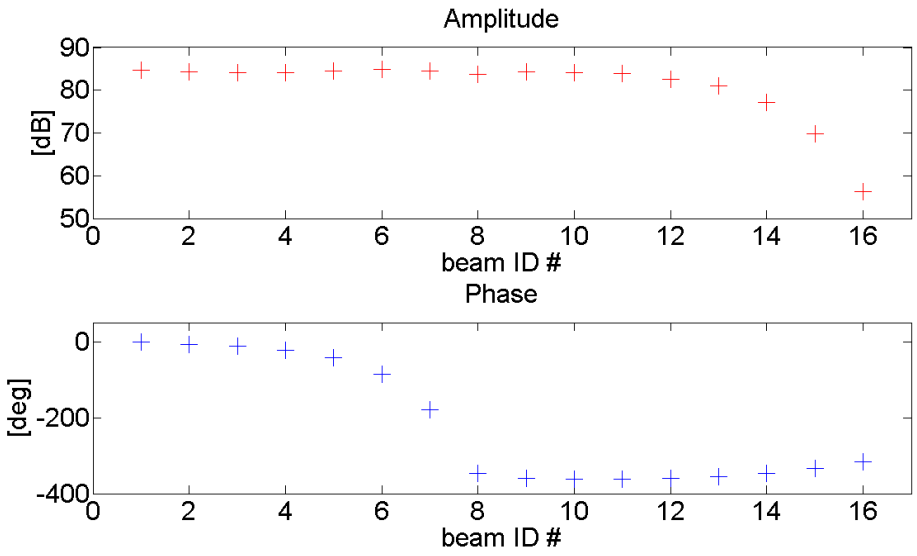

Figure 3.9. Mutual coupling based TRM characterization using TRM #1 as transmitter and TRM #0 as receiver. The transmitter power is adjusted such that the receiver is not saturated. Beams IDs are defined in Table 3.2. As expected, attenuation in excess of 30 dB is measured for beam ID 16, compared with beam IDs 1-9.

8 states that verify the operation of the attenuator. The measurements are archived and compared with previous calibrations data sets. It allows to diagnose system issues such as, phase shifter or attenuator failure, Rx and Tx gain drift due to temperature variation, SMP coaxial connector malfunction.

As shown in Figure 3.10, the RF performance of TR modules exhibits temperature dependence due to utilization of solid state components. *Medina et al.* (2012a) reports phase drift of $0.6°/°C$ in both Rx and Tx mode, while amplitude drift varies from $0.02dB/°C$ in Rx mode to $0.1dB/°C$ in Tx mode. As mentioned before, the mutual coupling measurement involves both Tx and Rx modes at the same time. The temperature drift measured here equals $0.15dB/°C$ and $0.7°/°C$ for amplitude and phase respectively.

In practice, the temperature of all TR modules across entire array varies within $\pm 1°C$ during radar operation. In this case, phase drift should not be of major concern,

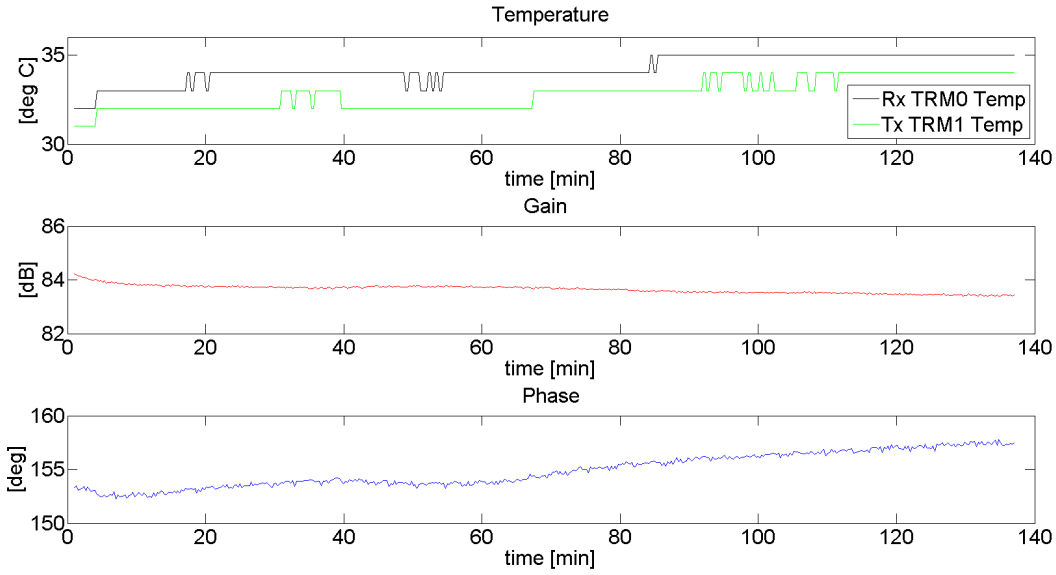

Figure 3.10. The RF performance of TR modules exhibits temperature depenedence due to utilization of solid state components. The measured temperature drift equals to $0.15dB/°C$ and $0.7°/°C$ for amplitude and phase respectively.

since beamforming depends on the relative phase shift between TR modules. Also, the expected phase and amplitude variation is smaller than a single bit phase shifter- and attenuator step (5.625° and $0.5dB$ respectively) and therefore can not be corrected.

Finally, the temperature dependence of TR module RF performance should be taken into consideration only if a significant difference between calibration and data measurement temperature is expected. In this case, the radar constant should be modified accordingly. For this purpose, temperature information is stored in a log file at the beginning and the end of each data collection session.

Figure 3.11 shows the difference between near field and mutual coupling calibration methods. Error bars represent two standard deviations of uncertainty, which for amplitude measurement equals 0.06 dB, while for phase measurement equals 0.6°. This error is mostly due to the precision of the phased array system data acquisition card and to the up/down converter stability. Error induced by near field probe

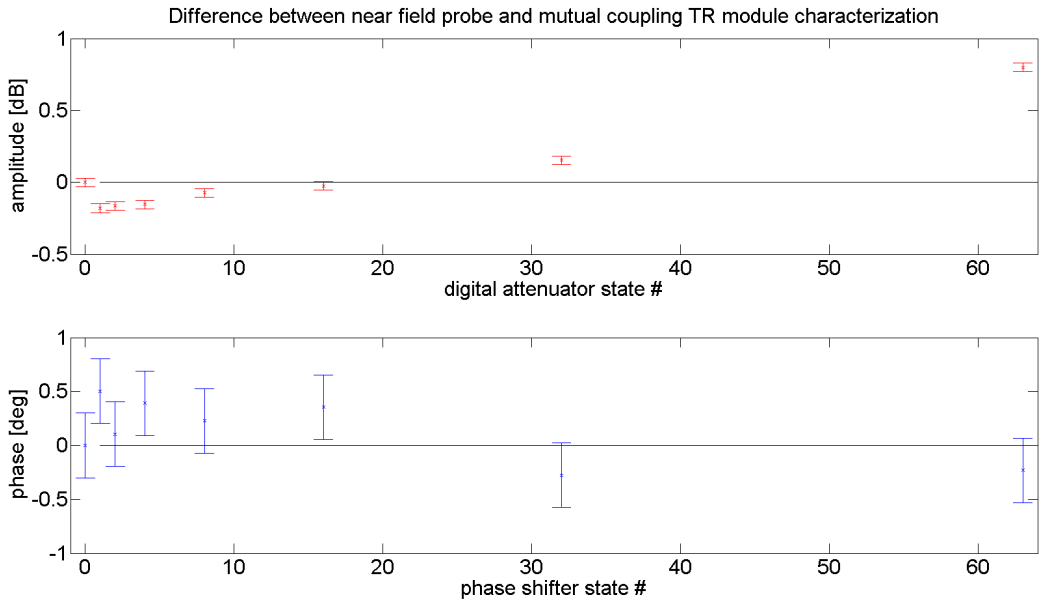

Figure 3.11. Comparison of the near field probe and mutual coupling calibration methods.

measurement is one order of magnitude smaller and can be neglected. Both methods stand in a good agreement. An increasing error when higher attenuator states are utilized is observed. The source of this error is unclear. However, for moderate amplitude distribution functions (such as a Taylor 25 dB window), attenuator states higher than #26 are never used. Furthermore, the measurements compared here were taken 2 months apart from each other and the system was physically moved in the meantime. This fact, together with temperature drift and inherent errors specific to investigated methods, can explain the difference in both measurements.

3.3 Horn calibration

Antenna performance has to meet several requirements to provide meaningful measurements for weather surveillance. In a dual-polarized system, it is important to verify that both channels are illuminating exactly same volume, i.e., the beam pointing direction and 3dB beamwidth are matching. Antenna beam patterns are

usually measured in an ancheoic chamber at the manufacturer's site. If a mechanical dish antenna is considered, these patterns are not supposed to change with time unless a mechanical incident occurs. In a phased array system, the antenna pattern depends on the number of active TR modules and may degrade over time. Damaged TR modules can be replaced during a scheduled maintenance period and recalibrated using the mutual coupling method described in the previous section. Once this procedure is completed, antenna patterns should be measured. A common method to verify antenna patterns in transmit mode is by illuminating a calibrated receiving antenna located in the far field. The received signal is then recorded on the remote antenna site or downconverted and transmitted back to the radar data acquisition card. Similar, beam patterns in receive mode may be obtained by transmitting a CW RF signal from a calibration antenna and recording the received signal on the radar system. The drawback of this method is that it requires a phased array system under test to be mounted on a pedestal during calibration process.

A schematic showing the experimental setup to complete measurements of antenna patterns using a horn antenna is shown in Figure 3.12a. The PTWR is mounted on a pedestal, which allows characterization of all 91 beams for weather surveillance within a time period of 5 minutes. A horn antenna was located 50 meters away from the PTWR. In order to reduce multipath effect, it is advantageous to elevate both antenna systems. In receive mode, the RF signal at 9.36 GHz was fed into the horn antenna from a signal generator. In transmit mode, the signal received by the horn antenna was first downconverted to 60 MHz and then transmitted over a long IF cable back to the radar data acquisition card. In both cases, a combination of electronic and mechanical PPI scan was performed, i.e., the radar system was moved mechanically in azimuth while performing electronic beam switching. The list of available beams for PTWR is presented in Table 3.3.

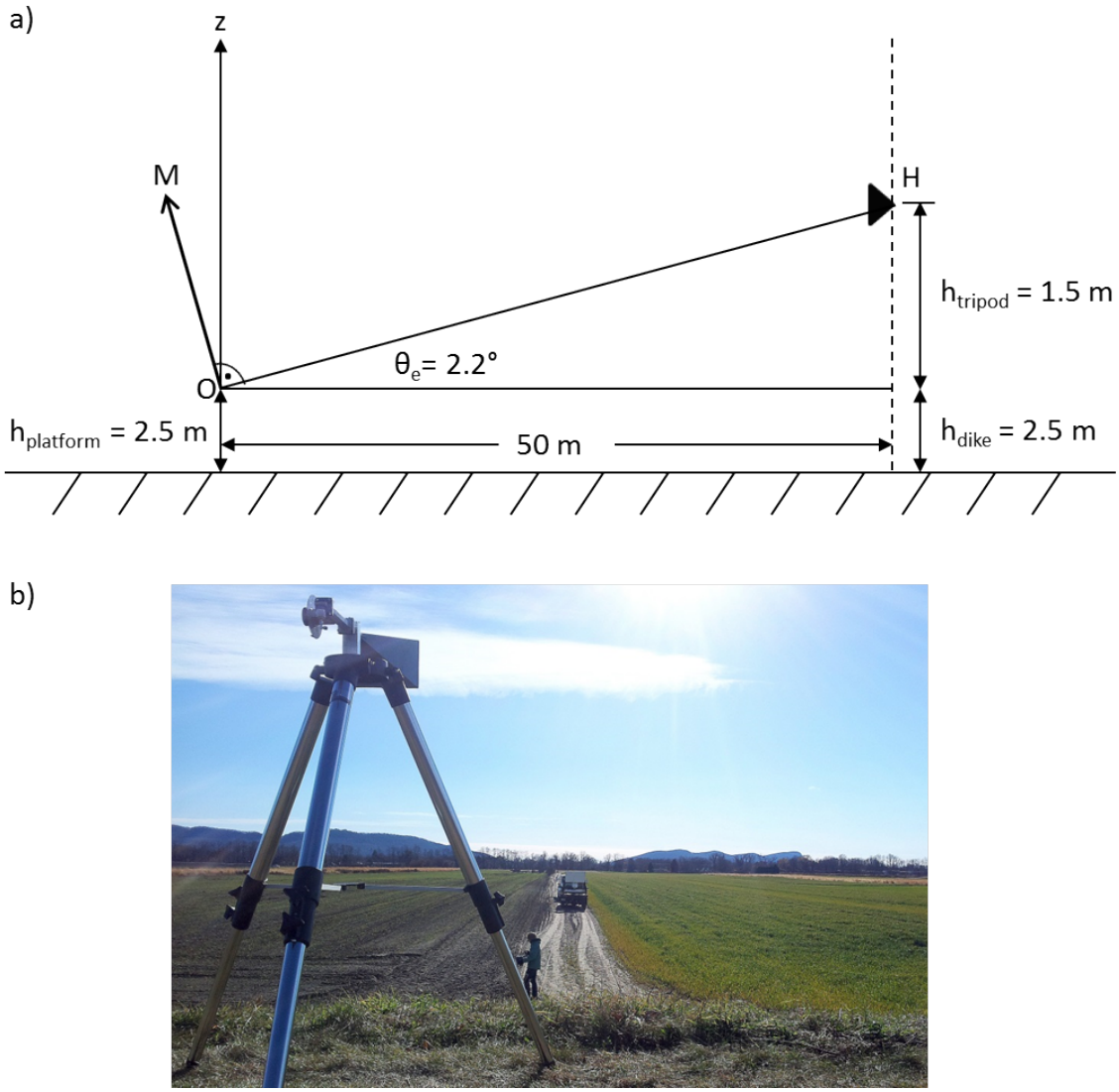

Figure 3.12. a) Schematic showing the experimental setup to make measurements of antenna patterns using horn antenna. The phase center of PTWR antenna array is at O, and a horn antenna at H. b) Horn antenna was mounted on a tripod located at the Connecticut River Dike Path in Hadley, MA.

Table 3.3. PTWR beam table. In a standard weather surveillance mode of operation (WR-ePPI), radar will perform electronic PPI scan using 91 beams with a 1 degree separation. PTWR can also emulate a mechanically scanned dish radar using broadside-only beam in WR-mPPI mode. Beams to verify spaced antenna (SA) implementation in phased array system are used in SA-ePPI and SA-mPPI mode of operation.

beam ID	**# of Tx**	**# of Rx**	**beam direction** [$\circ$]	**radar mode**
$0-90$	64	64	-45 to $+45$	WR-ePPI
$91-164$	$43-61$	$36-50$	-45 to $+45$	SA-ePPI
$165-176$	$19-60$	$16-49$	broadside	SA-mPPI
$177-255$	64	64	broadside	WR-mPPI

Calibration data was collected in a raw I,Q format. Each beam contains 16 pulses of the same polarization. In post-processing, the following steps were executed:

1. Read in data (16 pulse per beam) from binary file. A counter value stored in first gate of each pulse is verified for data consistency check.

2. Azimuth position data are smoothed.

3. Azimuth data are checked if all values are unique.

4. Note, that it takes four independent mechanical operations of the pedestal to characterize the beams in all four modes of operation. Therefore, initial data points are measured at slightly different azimuth positions. Linear interpolation is applied to increase the number of data points. This is needed for accurate beamwidth calculation. Further, after this operation, all beams are aligned to the same azimuth vector spanning azimuth locations between 110 and 240 degrees.

5. The patterns are normalized to the pointing direction of the TxV broadside beam. Power on transmit in TxV and TxH mode is normalized to the peak power in TxV mode (beams 0-90). Power on receive in RxV and RxH mode is normalized to the peak power in RxV mode (beams 0-90).

6. 3 patterns are plotted: Tx pattern, Rx pattern and a two-way pattern.

7. Additional parameters calculated for each pattern: peak sidelobe level, 3dB beamwidth, beam direction misalignment, beam gain.

One way antenna patterns are presented in Figures 3.13 - 3.20. On transmit, a uniform distribution is applied in order to maximize transmitted power. It is hypothesized that the increased peak sidelobe level (9 - 11 dB instead of the expected value of 13 dB) is due to RMS amplitude errors in the implementation of the uniform distribution. Another source of a measurement error is related to the multipath propagation effect, which can not be avoided in this measurement setup. The scanned beamwidth θ_s is increased from the broadside beamwidth θ_b as in Equation 3.4. This stands in good agreement with the data presented in the 3 dB beamwidth panel in Figures 3.14 and 3.16. The measured mean beam separation in all modes of operation is 1.036°, which is slightly larger from the requested 1° beam separation. This bias is attributed to the utilized pedestal actuator reading error. On receive, a 25 dB Taylor distribution was implemented. However, not all TR modules were operational at the time of the calibration process due to hardware failures and hence expected sidelobe reduction could not be achieved. Multipath effects also influence the accuracy of the measurements. In the current setup, a sidelobe reduction better than 19 dB is measured.

The synthesized two-way antenna patterns are shown in Figures 3.21 - 3.23. Beam gain reduction up to 4 dB is possible when scanning away from broadside. The two-way 3 dB beamwidth increases from 1.1° at broadside up to 1.8° when scanned ±45° away from broadside. The maximum $3dB$ antenna beamwidth mismatch in dual polarized measurements equals 0.17°. The maximum beam pointing mismatch in dual polarized measurements equals 0.08°.

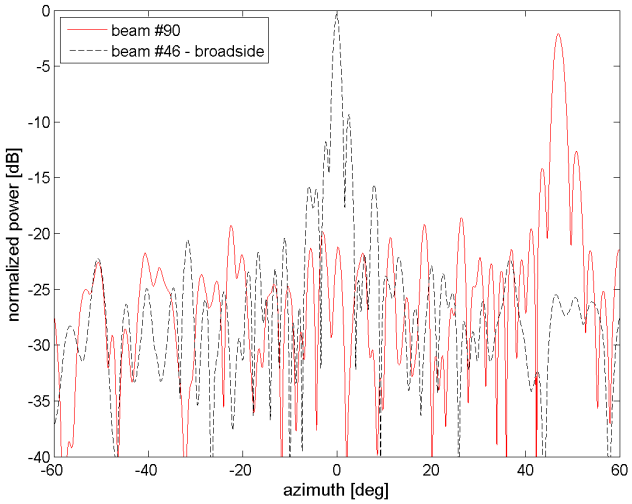

Figure 3.13. Antenna patterns of broadside- and +45° away from broadside beams in TxV mode of operation. Beam broadening up to 0.75° and gain reduction up to $2dB$ while scanning off broadside were measured.

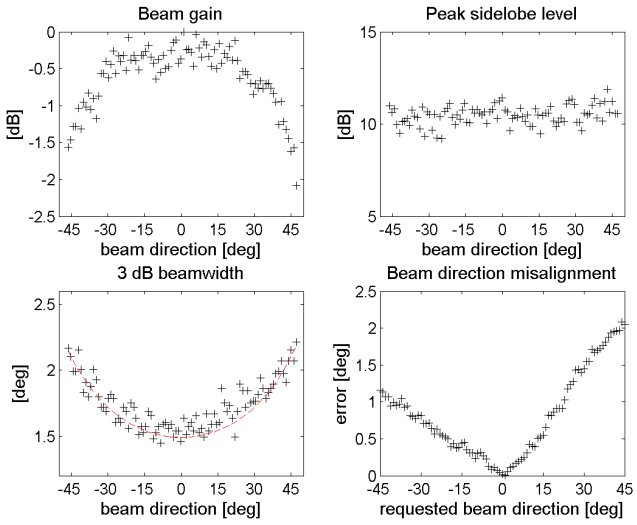

Figure 3.14. Figures of merit for antenna patterns of beams ID $0-90$ in TxV mode of operation. Beam gain reduction up to $2dB$ and peak sidelobe level better than 10 dB were measured. The scanned beamwidth θ_s is increased from the broadside beamwidth θ_b as $\theta_s = \theta_b/cos(\phi)$, where ϕ is beam direction. This stands in good agreement with the data presented in 3 dB beamwidth panel. The error in beam direction misalignment is due to miscalibration of the pedestal azimuth actuator.

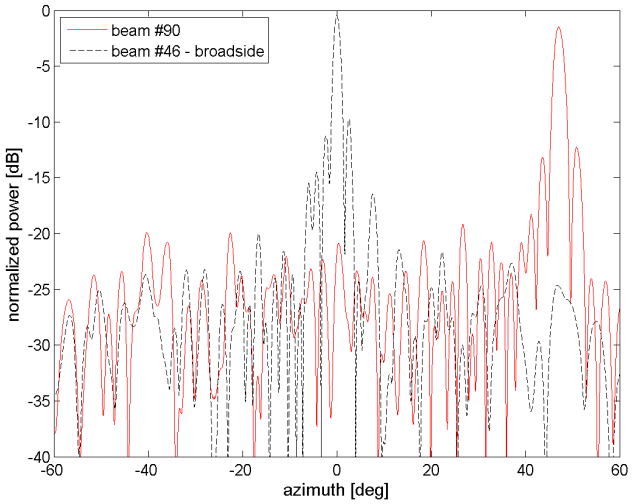

Figure 3.15. Antenna patterns of broadside- and +45° away from broadside beams in TxH mode of operation. Beam broadening up to 0.65° and gain reduction up to $1.5dB$ while scanning off broadside were measured.

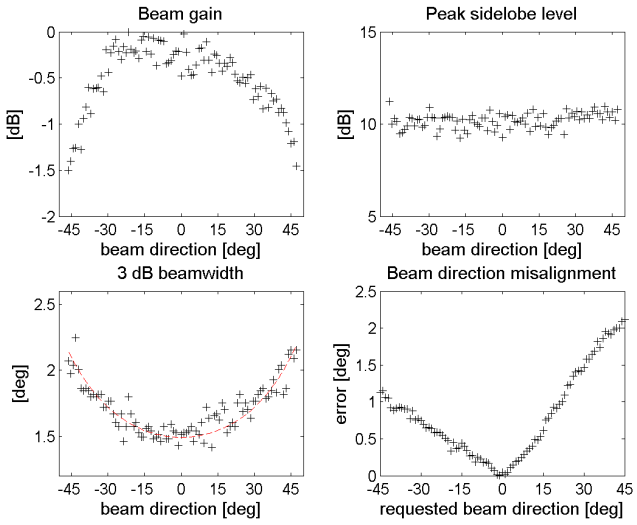

Figure 3.16. Figures of merit for antenna patterns of beams ID $0-90$ in TxH mode of operation. Beam gain reduction up to $1.5dB$ and peak sidelobe level better than 10 dB were measured. The scanned beamwidth θ_s is increased from the broadside beamwidth θ_b as $\theta_s = \theta_b/cos(\phi)$, where ϕ is beam direction. This stands in good agreement with the data presented in 3 dB beamwidth panel. The error in beam direction misalignment is due to miscalibration of the pedestal azimuth actuator.

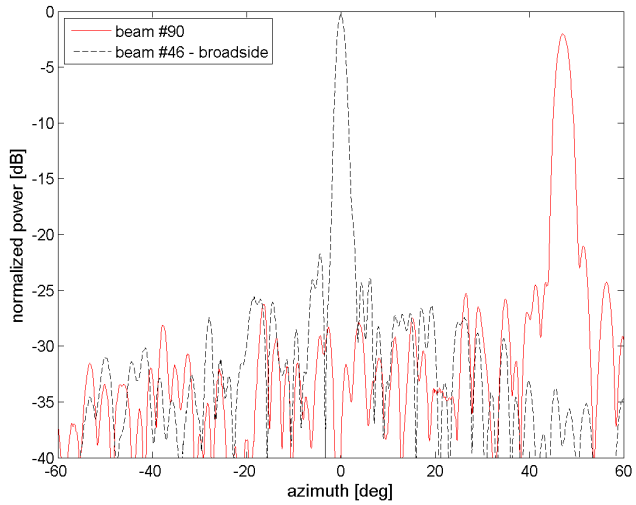

Figure 3.17. Antenna patterns of broadside- and $+45°$ away from broadside beams in RxV mode of operation. Beam broadening up to $0.96°$ and gain reduction up to $1.7dB$ while scanning off broadside were measured. $25dB$ Taylor tapering was applied in order to reduce antenna sidelobes.

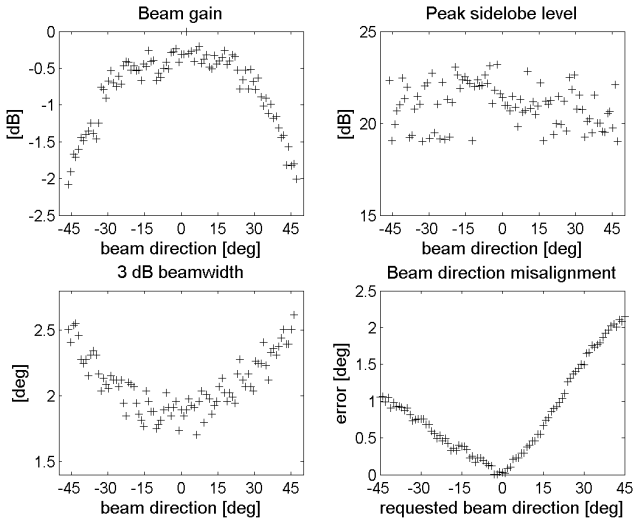

Figure 3.18. Figures of merit for antenna patterns of beams ID $0-90$ in RxV mode of operation. Beam gain reduction up to $2dB$ and peak sidelobe level better than 19 dB were measured. The $3dB$ antenna beamwidth increases from $1.7°$ to $2.85°$. The error in beam direction misalignment is due to miscalibration of the pedestal azimuth actuator.

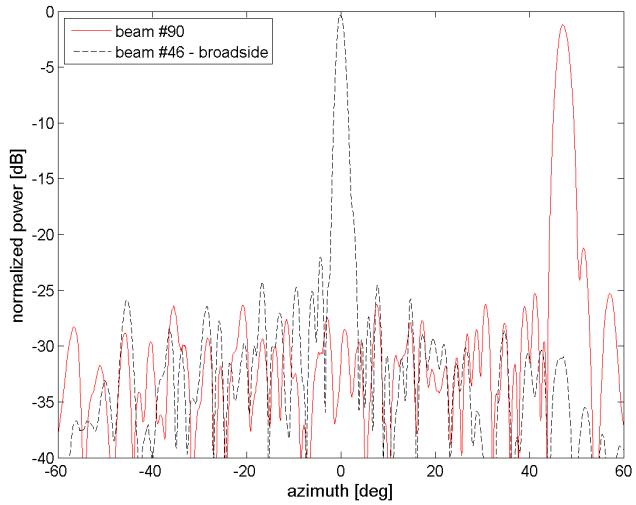

Figure 3.19. Antenna patterns of broadside- and $+45°$ away from broadside beams in RxH mode of operation. Beam broadening up to $0.86°$ and gain reduction up to $0.85dB$ while scanning off broadside were measured. $25dB$ Taylor tapering was applied in order to reduce antenna sidelobes.

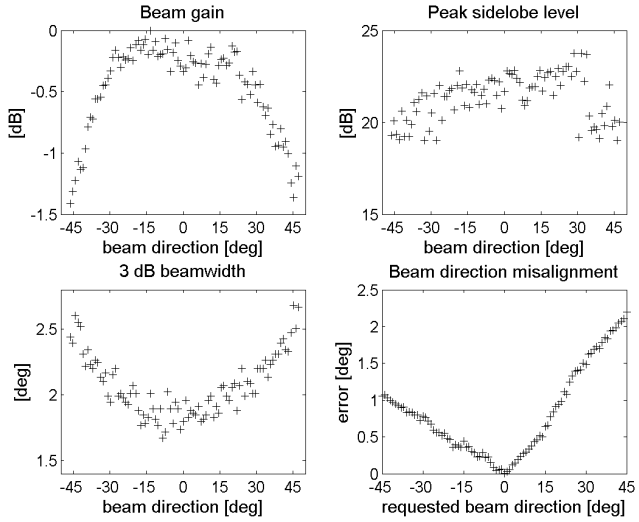

Figure 3.20. Figures of merit for antenna patterns of beams ID $0-90$ in RxV mode of operation. Beam gain reduction up to $2dB$ and peak sidelobe level better than 19 dB were measured. The $3dB$ antenna beamwidth increases from $1.6°$ to $2.6°$. The error in beam direction misalignment is due to miscalibration of the pedestal azimuth actuator.

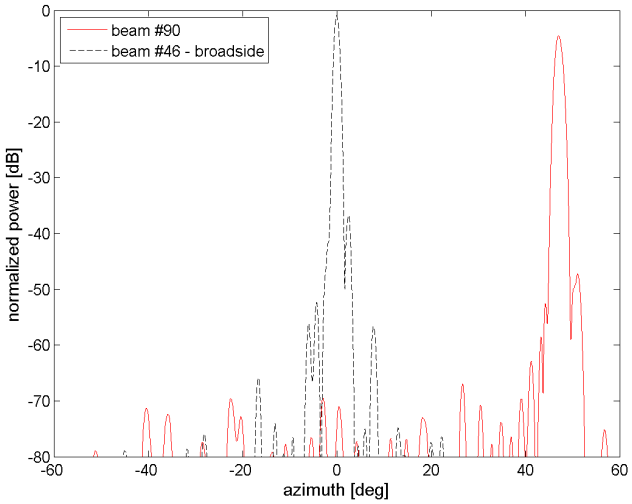

Figure 3.21. Synthesized 2-way antenna patterns of broadside- and +45° away from broadside beams in V-pol mode of operation using horn antenna. Beam broadening up to 0.64° and gain reduction up to 3.9dB while scanning off broadside were measured. Peak sidelobe in all beams is located on the right side of the mainlobe.

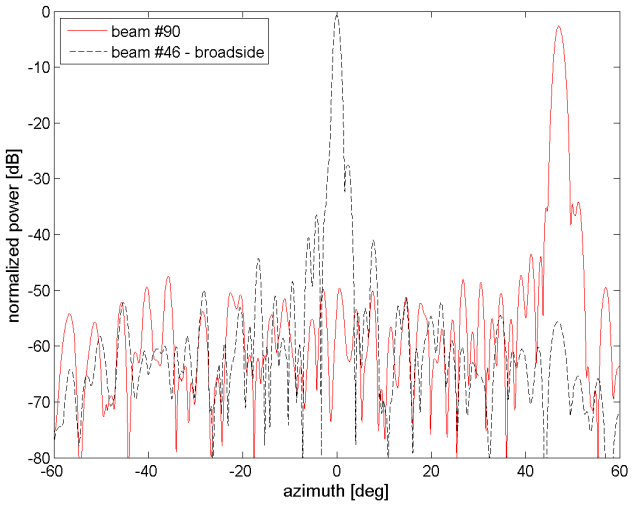

Figure 3.22. Synthesized 2-way antenna patterns of broadside- and +45° away from broadside beams in H-pol mode of operation using horn antenna. Beam broadening up to 0.66° and gain reduction up to 3.1dB while scanning off broadside were measured. Increased sidelobes level compared with V-pol patterns is attributed to the lower signal to clutter ratio in H-pol measurements.

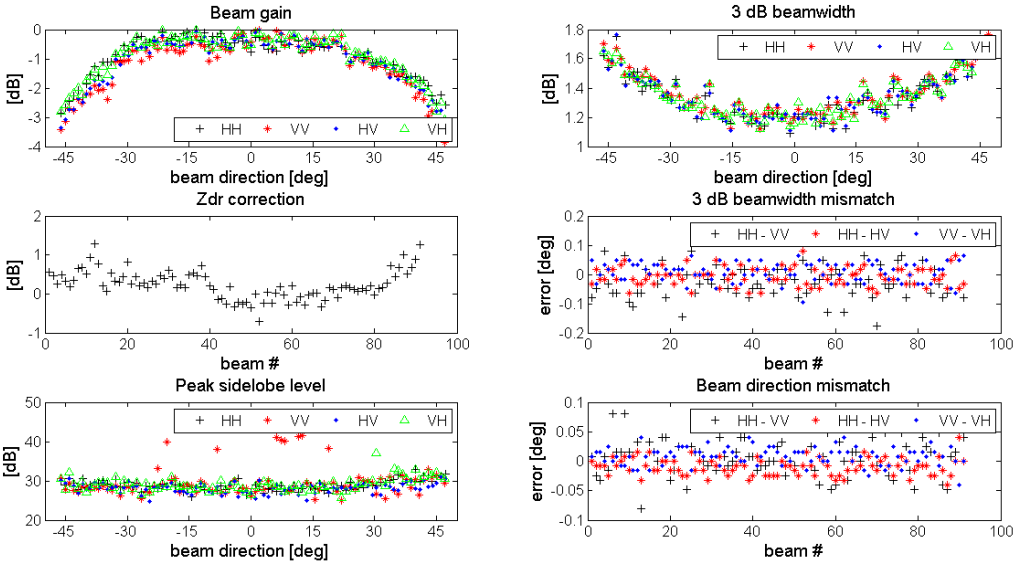

Figure 3.23. Figures of merit for synthesized 2 way antenna patterns of beams ID $0 - 90$. Peak sidelobe level better than 27 dB was measured. The maximum $3dB$ antenna beamwidth mismatch in dual polarized measurements equals to 0.17°. The maximum beam pointing mismatch in dual polarized measurements equals to 0.08°.

3.4 Corner reflector calibration

A corner reflector has a known radar cross section and therefore is commonly used as a calibration standard in an end-to-end radar calibration. The accuracy of the measurement is subject to finite signal-to-clutter (SCR) ratio as depicted in Figure 3.24, which is the main limitation of this calibration method. If the signal-to-clutter is smaller than 25 dB, then the relative error in received power from the corner reflector may exceed $\pm$ 0.5 dB. This makes the absolute calibration of a multibeam radar system using a corner reflector particularly challenging. Due to the fact that the return from a corner reflector has a zero Doppler velocity, clutter filtering is not possible. A possible solution to bypass this restriction is to mount a calibration target on a moving platform as suggested by *Bharadwaj et al.* (2013).

The location of the corner reflector plays a crucial role in the reduction of the multipath effect and the ground clutter contamination. Figure 3.25a presents the schematic of the experimental setup used for PTWR end-to-end calibration. A corner reflector was located 200 meters away from radar platform on the top of the 6.5 meter tower (see Figure 3.25b). The calibration target location is governed by two contradicting factors. First, it has to be far enough away, so the radar can collect the return from the target after it switches into receive mode. This is a severe limitation if long waveforms are considered. PTWR is a monostatic system, which uses a common antenna for transmission and reception. For example, if a $20\mu s$ waveform is considered, the corner reflector should be located at least 3 km away from radar system. Thus corner reflector is an impractical calibration source if pulse compression waveforms are utilized. Second, the antenna cross-range resolution is proportional to the range and therefore it is expected that signal to clutter ratio will decrease as the corner reflector is mounted further from the radar system.

Observations with and without a corner reflector were performed, in order to evaluate initial signal-to-clutter ratio at the corner reflector calibration site. Figure

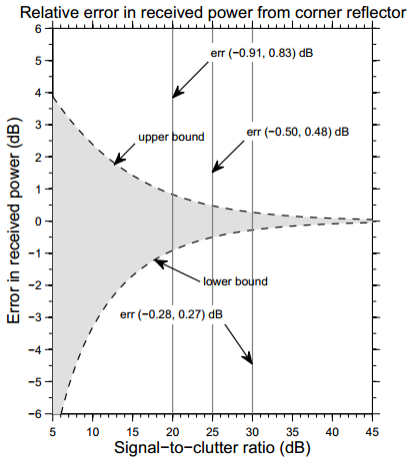

Figure 3.24. The relative error in received power from corner reflector depends on signal-to-clutter ratio. The bias greater than 0.25 dB is present, if SCR is smaller than 30 dB. Reprinted from *Bharadwaj et al.* (2013).

3.26 shows the signal-to-noise ratio of clutter targets with corner reflector located at beams #52 and #53. The measurement was repeated at several tilt angles spanning range from 1.4° to 3.6°. For $\theta_{el} = 1.86°$ the antenna was pointing exactly at corner reflector. However, the PTWR one-way elevation beamwidth equals 3.8°, which at the location of the corner reflector illuminates a volume 14 meters in elevation. This introduces increased ground clutter contribution. As the antenna tilt angle is increased, the signal-to-clutter ratio improves. For the vertical polarization channel, the signal-to-clutter ratio improves from $24.8dB$ at $\theta_{el} = 1.4°$ to $34.6dB$ at $\theta_{el} = 3.6°$. In the horizontal polarization channel, the signal-to-clutter ratio is always below 24 dB, which is due to the contamination caused by transmitted pulse leakage. As presented in Figure 3.27, the signal power of the leakage pulse in H-channel is significantly higher than in V-channel and contaminates several gates in the vicinity of the transmitted pulse. Therefore it is advised to isolate the leakage path during corner reflector calibration.

Although the measured signal to clutter ratio at the calibration site is too low for an accurate absolute radar calibration, it can still be useful to verify beam gain roll

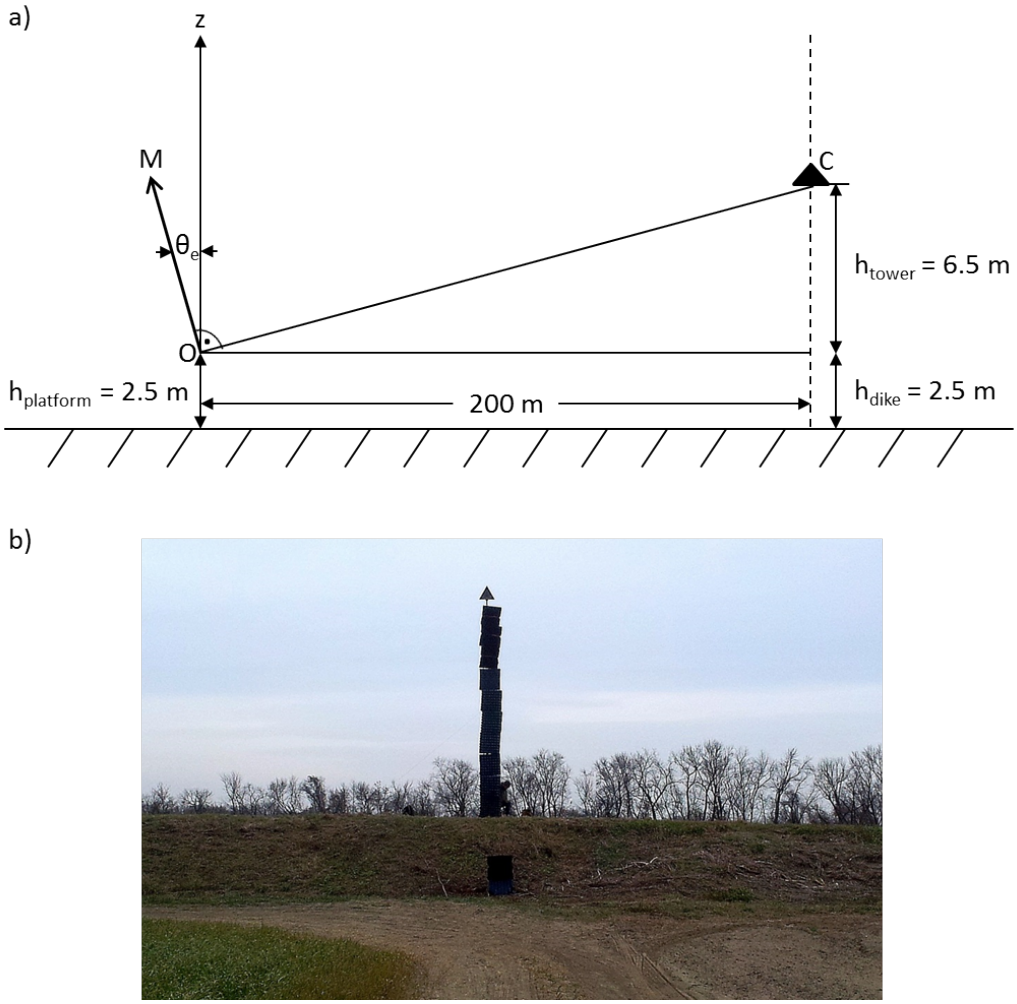

Figure 3.25. a) Schematic showing the experimental setup to make measurements of antenna patterns using corner reflector. The phase center of PTWR antenna array is at O, and a corner reflector at C. b) Corner reflector was mounted on a tower located at the Connecticut River Dike Path in Hadley, MA.

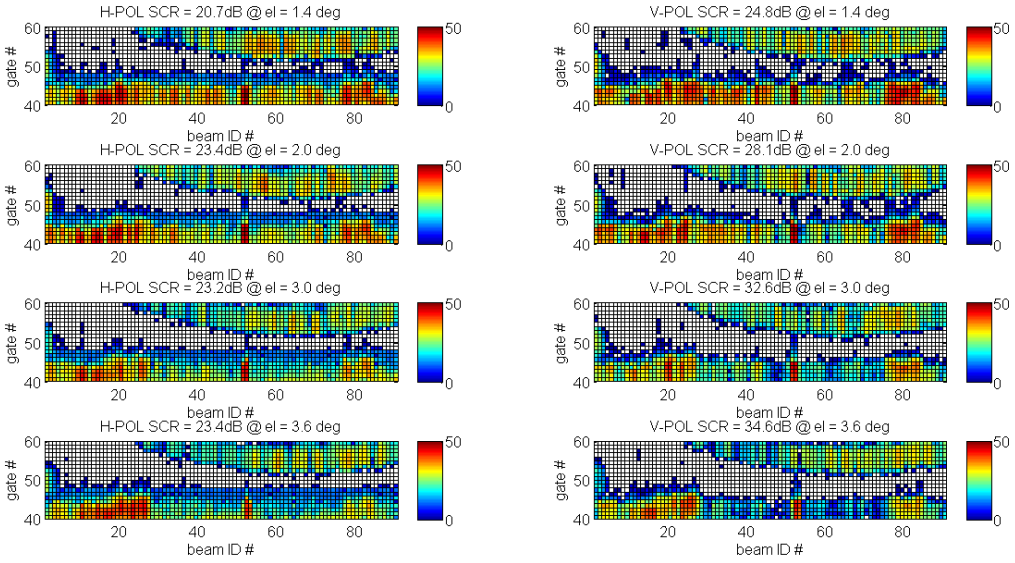

Figure 3.26. Signal-to-noise ratio of clutter targets at the corner reflector calibration site. The measurement was repeated at several tilt angles. The corner reflector is located at beams 52 and 53. Clutter signal power is higher in H-pol channel due to contamination caused by transmitted pulse leakage. Connecticut River is visible between gates 45 and 55.

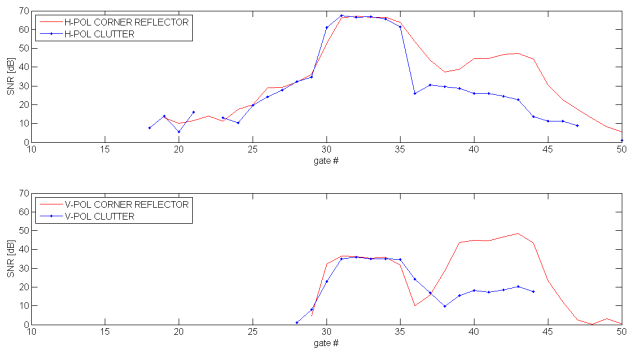

Figure 3.27. Initial assessment of signal-to-clutter ratio. The leakage of a transmitted waveform is located between gate 30 and 35, and a return from corner reflector is located between gate 40 and 45. The signal power of a leakage pulse in H-channel is significantly higher than in V-channel and contaminates several gates in the vicinity of transmitted pulse.

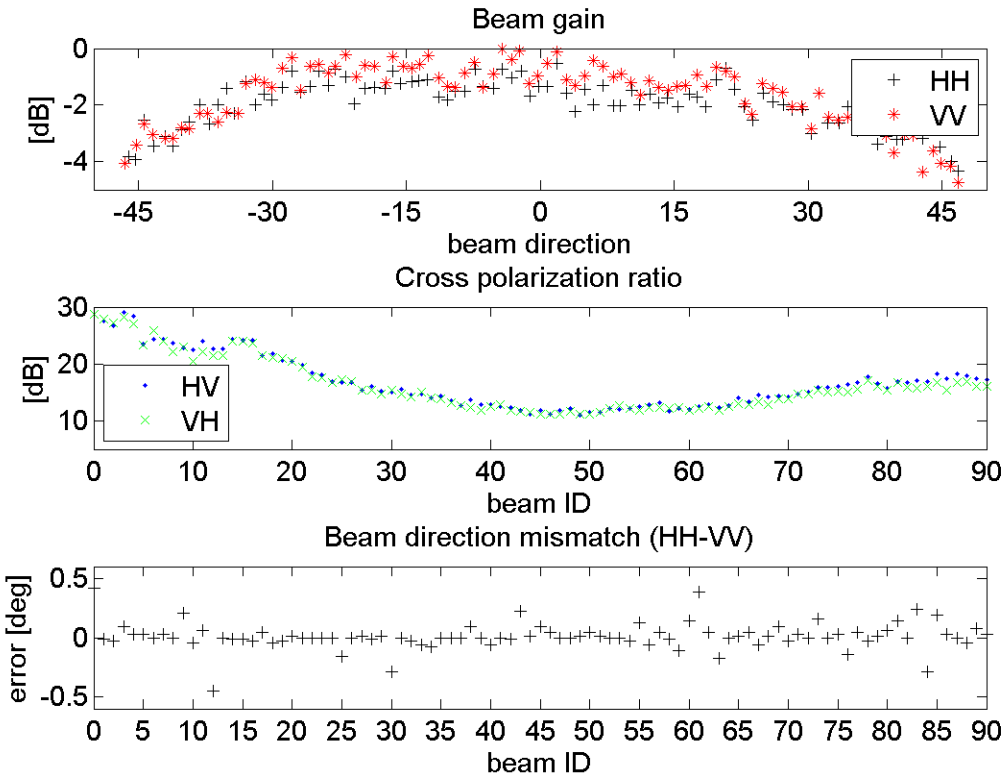

Figure 3.28. Figures of merit for a measured 2-way antenna patterns of beams ID $0 - 90$ using corner reflector. The bias in received power is on order of 1 dB in H-channel and 0.5 dB in V-channel due to low signal-to-clutter ratio. The cross polarization ratio improves as beam is directed away from broadside direction.

off and beam direction alignment and compare it against the horn calibration. Figure 3.28 shows the results of corner reflector calibration. The measurement was performed using a combination of electronic and mechanical PPI scan, i.e., the radar system was slowly moved mechanically in azimuth while performing electronic beam switching. The beam gain reduction up to $4dB$ stands in good agreement with a synthesized 2-way horn antenna calibration. The increased beam direction misalignment is a consequence of high signal to clutter ratio. Additionally, a cross polarization ratio (CPR) is determined. Due to antenna design fault, CPR is the lowest at broadside on order of 13dB and is better than 18dB at $\pm 45°$ away of broadside beam location.

CHAPTER 4

PULSE COMPRESSION TECHNIQUES FOR A PHASED-ARRAY WEATHER RADAR

4.1 Introduction

Over the past few decades, solid state devices have become of primary interest in radar system design and have started to offer a practical alternative to the traditional high power RF sources such as magnetrons or klystrons. Pulse compression is a signal processing technique which overcomes the low power limitation of the modern RF amplifiers and provides room for improvement of both radar sensitivity and range resolution. This technology has been widely implemented in military and air control radars, where precise detection of individual hard targets is the main interest. Although attempts to implement pulse compression in ground-based weather radar dates back to the 1970s (*Fetter*, 1970) (*Austin*, 1974), the first successful implementation was reported by *Mudukutore et al.* (1998) in the late 1990s using Barker phase coding. Feasibility studies about implementing pulse compression using frequency modulated waveforms were reported by *Ashe et al.* (1994) and *Keeler and Hwang* (1995), but its field test validation was not carried out due to hardware limitations.

In recent years, *O'Hora and Bech* (2007) used a digital transceiver and an FM based pulse compression processor in a C-band weather radar system to demonstrate that a magnetron can be replaced by a traveling wave tube producing 30 times less power while at the same time improving radar performance. *George et al.* (2010) documented an FM waveform design for a solid-state X-band weather radar.

This chapter is divided in three sections. First, the basic theory of pulse compression techniques and its benefits and constraints is presented. This is followed

by a discussion of waveform selection and a comparison of different mismatched filtering techniques. Here, emphasis is placed on a detailed methodology of inverse filter design. The next section gives a concise description of a procedure to design an FM waveform and an inverse filter for weather radar. Finally, pulse compression performance is validated in a field test.

4.2 Pulse compression techniques

4.2.1 Theory of operation

The major disadvantage of a solid state transmitter is its comparatively low peak power. According to the weather radar equation, the sensitivity of radar depends on the average transmitted power, which is a product of pulse duration and the transmitter's peak power. Since peak power is a constant parameter of the RF source, one way to improve radar sensitivity is by increasing the average power by increasing the pulse width. However, in a traditional pulsed radar, pulse width, τ, is coupled with range resolution, ΔR_τ, as follows:

$$\Delta R_\tau = \frac{c\tau}{2} \tag{4.1}$$

where c is the speed of light. Therefore increasing radar sensitivity will decrease range resolution. Pulse compression allows transmission of very long pulses to increase radar detection, while recovering range resolution using frequency modulation. Range resolution, ΔR_B, is then inversely proportional to the utilized bandwidth B:

$$\Delta R_B = \frac{c}{2B}. \tag{4.2}$$

Compressing the received signal can be accomplished by using a matched filter receiver. As shown by *Richards* (2005) the matched filter is known to produce maximal signal-to-noise-ratio (SNR) and is given by:

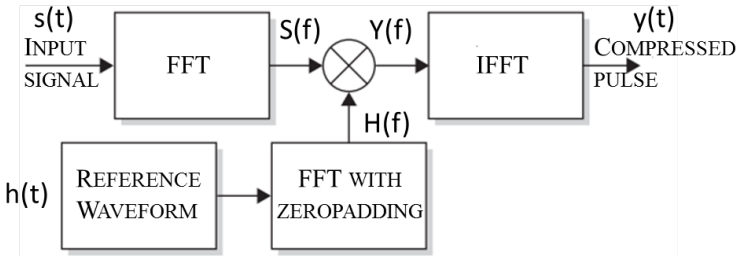

Figure 4.1. Frequency domain digital pulse compression implementation.

$$h(t) = s^*(-t) \quad \overset{\mathrm{F}}{\rightarrow} \quad H(f) = S^*(f) \tag{4.3}$$

$$y(t) = k \cdot s(t) \bullet h(t) \quad \overset{\mathrm{F}}{\rightarrow} \quad Y(f) = k \cdot S(f) \cdot H(f) = k \cdot |S(f)|^2 \tag{4.4}$$

where s(t) is a complex envelope sequence of the transmitted signal, y(t) is a compressed output of the matched filter, k is an attenuation factor, $*$ denotes the complex conjugation, and $\bullet$ indicates convolution.

Since convolution in the time domain is equivalent to multiplication in the frequency domain (see 4.4), two implementations are commonly used: a correlation processor using a finite impulse response (FIR) filter or a fast Fourier transform (FFT) processor. The first is advantageous in that the received data can be continuously processed and no buffering is necessary, while in the second case, illustrated in Figure 4.1, an entire range profile has to be collected before compression can be executed. However, *Bonato* (2002) showed that, FFT based processing outperforms FIR filter computational efficiency and is particularly favored in a case of longer input signals. Additionally, recent advances in digital signal processing enable FFT implementation into a low cost FPGA and hence the FFT based processor has become a preferable solution for pulse compression.

The compressed pulse has the shape of the autocorrelation function of the transmitted waveform attenuated by factor k. Assuming a rectangular pulse with a linear

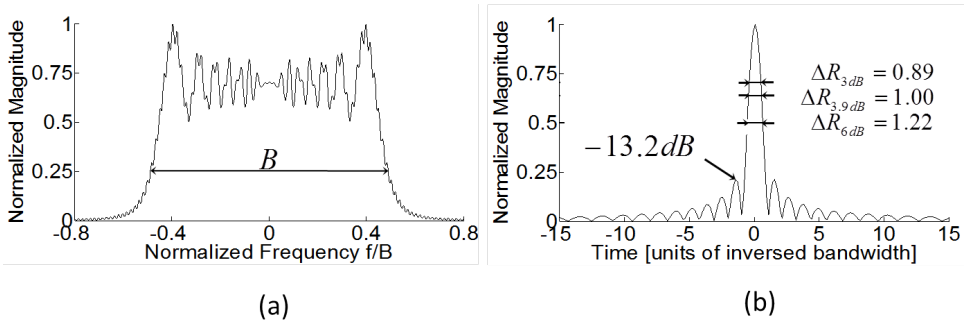

Figure 4.2. Frequency domain digital pulse compression implementation.

frequency modulation (LFM), one can expect an equally distributed frequency spectrum with relatively rectangular shape. This is reasonable since the carrier frequency is swept over a given bandwidth at a constant rate. Figure 4.2(a) presents a power spectrum of a compressed LFM waveform. Visible ripples can be noticed within waveform bandwidth, which are artifacts of Gibbs phenomenon and are directly related to the sharp discontinuities in the analyzed signal. This undesirable effect can be reduced, but not eliminated, if pulse duration or waveform bandwidth is increased. In general the shape of the power spectrum is better approximated as rectangular for large time-bandwidth (TB) products. However, this is usually limited by the system design constraints, i.e. maximum duty cycle and sampling frequency. The time bandwidth product for a typical weather radar application is usually kept below 100. Furthermore, the FFT assumes periodicity in the analyzed signal. In a pulsed weather radar, the transmitted signal does not begin and terminate at the same value e.g. zero, and hence a high frequency distortion overlaid on the waveform spectrum can be observed. This results in an artifact known as spectral leakage. Both effects can be significantly reduced by tapering transmitted pulse edges.

According to Fourier transform theory a rectangular shaped spectrum should resemble sinc function in the time domain. In consequence, part of the signal energy will be concentrated in unwanted range sidelobes as depicted in Figure 4.2(b) with

the first sidelobe level located -13.2 dB below main beam. These can severely corrupt data in the adjacent gates and has to be reduced by means of a separate range sidelobes suppression filter.

In all real systems, the desired radar echo is superimposed on white Gaussian noise. Since the noise is uncorrelated with the transmitted waveform, pulse compression does not effectively change noise statistics. Further, note that the signal energy is conserved after pulse compression processing (i.e. energy of input signal equals to the energy of output signal), but it is now for the most part located in the main beam of width c/B. Hence, we observe an improvement in signal power by a factor of BT. It should be emphasized that SNR can be increased only by increasing pulse duration or decreasing waveform bandwidth. Increasing signal bandwidth will in consequence raise the noise floor and reduce SNR. Finally, it is worth pointing out different range resolution definitions, which can be found in the literature (*Skolnik*, 1962). The range resolution given in Equation 4.2 is in fact 3.9 dB width of mainlobe, while in weather radar applications the 6 dB width is commonly used (see Figure 4.2(b)).

4.2.2 Trade offs

An optimal design of a radar waveform and pulse compression filter for a solid state weather radar is a result of many mutually dependent factors. The range resolution is nearly always several times smaller than the azimuth resolution, and hence it is a common procedure to average several consecutive range samples in order to increase the effective number of independent samples. In that manner the accuracy of measurements can be improved, and the dwell time can be reduced. In consequence, faster scan rates can be achieved. On the other hand, since deep reduction of range sidelobes should be a primary concern, implementation of a sidelobe suppression filter is necessary. Typically, such a filter will broaden the mainlobe of a compressed pulse and will reduce SNR compared to the matched filter output. Due to the fact

that modern solid state X-band amplifiers are rated below 1kW of peak power and that weather signal attenuates severely at X-band, it is a difficult compromise when considering sidelobe versus SNR reduction. An easy way to compensate for signal processing loss is by lengthening pulse duration, but this will also lengthen the radar blind zones, which can be a significant percentage of radar range. For example, a typical X-band radar covers a range up to 40 km, while a 40 μs pulse extends the 1^{st} radar blind zone to 6 km. This problem can be bypassed by interleaving a shorter uncompressed pulse as suggested by *Nakagawa et al.* (2006), but it comes at the cost of an additional signal processing complexity. Finally, since solid-state amplifiers are designed to sustain a high duty cycle, a high pulse repetition frequency (PRF) is preferred in order to reduce scan time and increase unambiguous velocity range. On the other hand this will reduce the unambiguous range R_{max}, as follows:

$$R_{max} = \frac{c(PRT - \tau)}{2} \tag{4.5}$$

Note that, unlike a simple pulsed radar system, pulse width τ can be relatively large compared with pulse repetition time (PRT) and thus cannot be ignored. For example, a 40 μs pulse transmitted at $PRF = 5kHz$ will result in an unambiguous range of 24 km instead of 30 km (see Figure 4.3). Therefore, if long pulse duration is required, a reduction in PRT is necessary.

4.2.3 Figures of merit

The performance of a range sidelobe suppression filter is evaluated by means of four figures of merit: peak sidelobe level (PSL), integrated sidelobe level (ISL), mismatch loss (L_{mm}), and range resolution (ΔR_{6dB}). The $6dB$ range resolution is measured in units of inversed bandwidth [$ibw = c/2B$] and represents the time extent over which the compressed pulse is within 6 dB of its peak. Typically, the range resolution will not exceed a value of 2.7 ibw, while its lower limit is set to 1.22 ibw

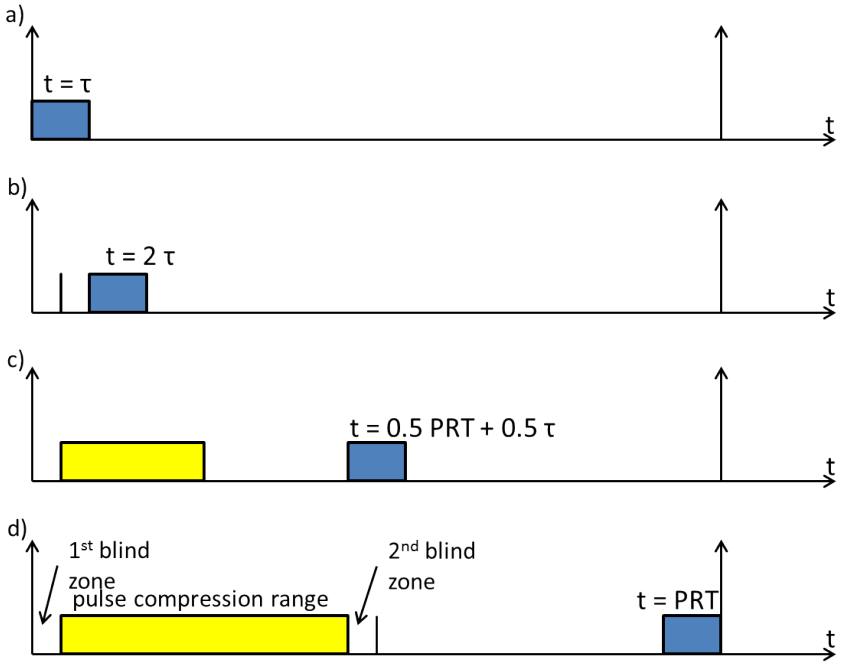

Figure 4.3. Illustration of a pulse compression blindzone. Radar sensitivity can be improved if the pulse duration is increased. The first gate with full pulse compression gain is located at $R = c\tau/2$ (b), and can be computed at $t = 2\tau$. The location of the trailing edge of the transmitted waveform at $t = 0.5PRT + 0.5\tau$ (c) indicates the beginning of the 2^{nd} blind zone (d). The extent of the 2^{nd} blind zone can be a significant if high PRF and long pulse duration is used. If duty cycle is above 50%, then 1^{st} and 2^{nd} blind zones overlap.

(matched filter case). Due to the finite sampling frequency, the shape and extent of the mainlobe of the filter output can be relatively poorly defined. Hence, in order to compare different filters, we define mainlobe inclusion and exclusion regions. The first contains all samples between the closest local minima in the vicinity of the mainlobe peak, while the latter contains all remaining samples. In the following equations s_j denotes sidelobe samples (mainlobe exclusion region) and m_k denotes the mainlobe samples of the compressed pulse (*Keeler and Hwang*, 1995):

$$PSL = 10log\left(\frac{max(|s_j|^2)}{max(|m_k|^2)}\right) \tag{4.6}$$

$$ISL = 10log\left(\frac{\sum |s_j|^2}{\sum |m_k|^2}\right) \tag{4.7}$$

The *PSL* indicates the highest power level in the mainlobe exclusion region compared to the mainlobe peak. The peak sidelobe is usually located close to the mainlobe, and hence restricts the maximum reflectivity gradient that can be correctly resolved. However, even more important for proper design of pulse compression for a meteorological radar is minimization of *ISL*, which is the ratio of the total energy outside the mainlobe exclusion region to the total energy inside the mainlobe inclusion region. Finally the mismatch loss L_{mm} represents the reduction in SNR after pulse compression compared to the matched filter output.

4.2.4 FM waveform

Ashe et al. (1994) concluded, that the tangent based NLFM waveform exhibits the best performance in terms of figures of merit. The frequency progression is defined as follows:

$$f(t) = \pm B\frac{tan(2\beta t/T)}{2\alpha} \qquad -\frac{T}{2} \leq t \leq \frac{T}{2} \tag{4.8}$$

$$\beta = tan^{-1}(\alpha) \tag{4.9}$$

where $\pm$ denote up- and down-chirp respectively,and α is a waveform frequency progression nonlinearity coefficient. Note that if $\alpha \to 0$, then Equation 4.8 defines the LFM waveform. The complex envelope of the NLFM waveform at baseband in terms of amplitude and phase modulation can be then described as:

$$u(t) = w(t) \cdot e^{j\pi ft} \qquad -\frac{T}{2} \leq t \leq \frac{T}{2}. \tag{4.10}$$

In general, the FM waveform is superior to the Barker-based phase code, due to its better Doppler sensitivity and mismatch loss. Additionally, as reported by *Ashe et al.* (1994), nonlinear frequency modulation (NLFM) codes, compared to their LFM counterparts, exhibit only a small SNR reduction when the range sidelobes suppression filter is implemented. The explanation for this can be found in the shape of power spectrum, which is less rectangular in the case of NLFM waveform. For example, it is possible to derive NLFM waveforms from a common window function such as Hann, that will exhibit the range sidelobe characteristics of the selected window at no reduction in SNR (*Richards et al.*, 2010). However, this gain comes at the cost of increased signal bandwidth, which in consequence will inevitably reduce system sensitivity. It is worth mentioning that, since the nonlinear frequency modulation is equivalent to the amplitude modulation in time domain, it is theoretically feasible to reduce mismatch loss of the LFM waveform by means of windowing on transmit. However, the improvement in mismatch loss, will not make up for the signal loss on transmit L_{Tx} due to the amplitude modulation itself. Additionally, it is desired to operate in the saturation region of a solid-state amplifier in order to maximize transmitted power. These are the main reasons against using amplitude modulation in weather pulse compression system.

In order to reduce the effect of the Gibbs phenomenon and spectral leakage, it is recommended to taper the edges of the transmitted waveform, and hence light amplitude modulation $w(t)$ is employed. Here it is important to ensure that $w(t = T/2) = w(t = -T/2) = p$, where $p \to 0$. In this manner, the signal periodicity requirement for FFT processing is fulfilled. Nonlinear frequency modulation results in a non-rectangular shape of spectrum, but at the same time the roll-off of spectrum edges is more gradual compared with the LFM waveform. Tapering on transmit reduces the signal bandwidth and in consequence reduces undesired aliasing effects. A good candidate for the amplitude modulation function is a Tukey window on pedestal, which is defined as (*Harris*, 1978):

$$w(x) = p + (1-p)\begin{cases} \frac{1}{2}\{1 + cos(\frac{2\pi}{\gamma}[x - \frac{\gamma}{2}])\} & 0 \leq x < \frac{\gamma}{2} \\ 1 & \frac{\gamma}{2} \leq x < 1 - \frac{\gamma}{2} \\ \frac{1}{2}\{1 + cos(\frac{2\pi}{\gamma}[x - 1 + \frac{\gamma}{2}])\} & 1 - \frac{\gamma}{2} \leq x \leq 1 \end{cases} \tag{4.11}$$

where γ is a ratio of tapered to constant sections of a window and p is a height of a pedestal. The Tukey window is a member of the raised cosine group of window functions. Therefore if $\gamma = 0$, Equation 4.11 defines rectangular window, while $\gamma = 1$ returns a von Hann window. The signal power loss due to waveform tapering L_{Tx} can be calculated using Parseval's theorem and for a moderate tapering factor ($\gamma \leq 0.17$) does not exceed $0.5dB$. Finally, the power spectrum of an FM waveform can be even further smoothed out by means of a sigma approximation method (*Lanczos*, 1956) or by application of an appropriate phase predistortion to the transmitted pulse as described by *Kowatsch and Stocker* (1982).

4.2.5 Window filter

A window filter can significantly reduce range sidelobes, but it comes at the expense of a reduction of both range resolution and SNR. An extensive review on available windows and their properties and limitations is described by *Harris* (1978).

The basic idea behind the window filter is to shape the frequency response of the matched filter. Figure 4.4 shows a matched filter frequency response for an LFM waveform and an overlay of a Blackman window. The window may be applied in the time domain or to the „flat" central part of the frequency-domain response. Again, an additional improvement can be accomplished by means of tapering waveform edges on transmit, which removes unwanted ripples in the central part of the spectrum. On the other hand, windowing on both transmit and receive rejects a part of signal energy reducing both SNR as well as range resolution, which is coupled with effective bandwidth. Increasing window support and the level of the pedestal will diminish these drawbacks, but will again raise the sidelobes. The window function reduces the signal power, but also reduces noise power. The SNR loss due to window applied in time domain is expressed as:

$$L_{SNR} = \frac{\left(\sum_{i=0}^{N-1} w_r[i]\right)^2}{N \sum_{i=0}^{N-1} \left(w_r[i]\right)^2} \tag{4.12}$$

where $w_r[i]$ are the *FIR* filter weights lying between 0 and 1. The numerator in Equation 4.12 reflects the loss due to the coherent summing of the matched filter to the chirp signal, while the denominator defines the filter loss on the noise. The noise adds noncoherently, and so the filter weights are combined as mean squares.

Although it is not feasible to design a window with no sidelobes, theoretically it is possible to construct a window with arbitrarily low sidelobes. However, since waveform design for a pulsed compression weather radar is a trade-off between many factors, this method for a low time-bandwidth product provides sidelobe suppression

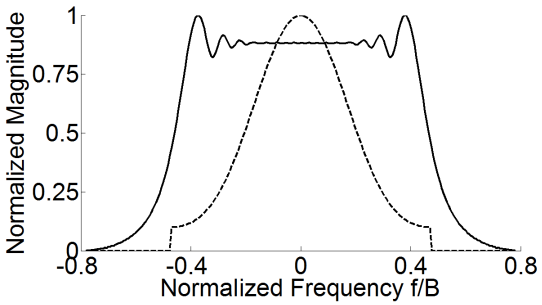

Figure 4.4. Blackman window on a pedestal superimposed on a matched filter frequency response. LFM waveform (BT = 80) with applied Tukey window (γ = 0.12).

up to $50dB$ at a cost of significant reduction in SNR in excess of 3 dB (*Zhao and Xin*, 2009).

4.2.6 Inverse filter

The inverse filter, also known as a deconvolution filter or Wiener filter, is an optimal design that minimizes energy in sidelobes in the least squares sense. An inverse filter is a unique design for a given waveform. It compensates ripples in the spectrum of a transmitted signal, and hence very low sidelobes can be obtained with only slight reduction in SNR and range resolution. The inverse filter can be applied to the matched filter output or directly to the uncompressed signal. The former tends to be the preferred choice since it reduces the complexity of the signal processing chain.

To compute filter coefficients, we use the least-square error method described by *Treitel and Robinson* (1966). The aim of optimization is to minimize the following quantity:

$$I = \sum_{k=0}^{M+N} (d_k - (f_k \bullet b_k))^2. \tag{4.13}$$

Here we want to construct a filter of length M ($f_k, k = 0, ..., M$) which will reshape the input signal of length N ($b_k, k = 0, ..., N$) into the desired output ($d_k, k = 0, ..., M + N$). Equation 4.13 can be rewritten into a matrix form as:

$$f = R^{-1} \cdot g \tag{4.14}$$

where R is an autocorrelation matrix of b_k and g is the causal part of the crosscorrelation of b_k and d_k. Note that R is Toeplitz and thus it is always invertible.

The proper definition of the desired response of the inverse filter is crucial. It has been found that samples in the direct vicinity of central peak considerably affect the performance of inverse filter. As reported by *Ashe et al.* (1994), minimization of these samples results in an increased sidelobe level. The optimal shape of the central peak is unknown, but it is here assumed that the ideal response should resemble the matched filter output with no sidelobes. Therefore it is suggested to calculate filter coefficients in an iterative manner (see Figure 4.5b), which is an extension of the method described by *Ashe et al.* (1994). In the first iteration we define the desired response of the inverse filter d_k as shown in Figure 4.5a. Here samples contained within the central peak (denoted with and $\diamond$ and $\circ$) are corresponding to the respective samples of the autocorrelation function of the transmitted waveform b_k, while remaining part of the response (denoted with $\times$) is set to zero. In this study the shape of the desired response is obtained by means of Nelder-Mead simplex method, which in each iteration changes $\circ$ samples and evaluates the optimization function:

$$t = w_1(PSL) + w_2(ISL) + w_3(\Delta R_{6dB}) + w_4(L_{mm}) \tag{4.15}$$

where w_n is a weigthing factor, which is a function of individual figures of merits. Typically, one would like to optimize integrated and peak sidelobes level, but it is also possible to minimize mismatch loss, improve range resolution or a combination of all four factors.

Inverse filter is superior to window filter due to the fact that in the case of inverse filter both amplitude and phase information are employed in order to decrease sidelobe level. *ISL* value in excess of 100 dB can be achieved if a filter much longer than the

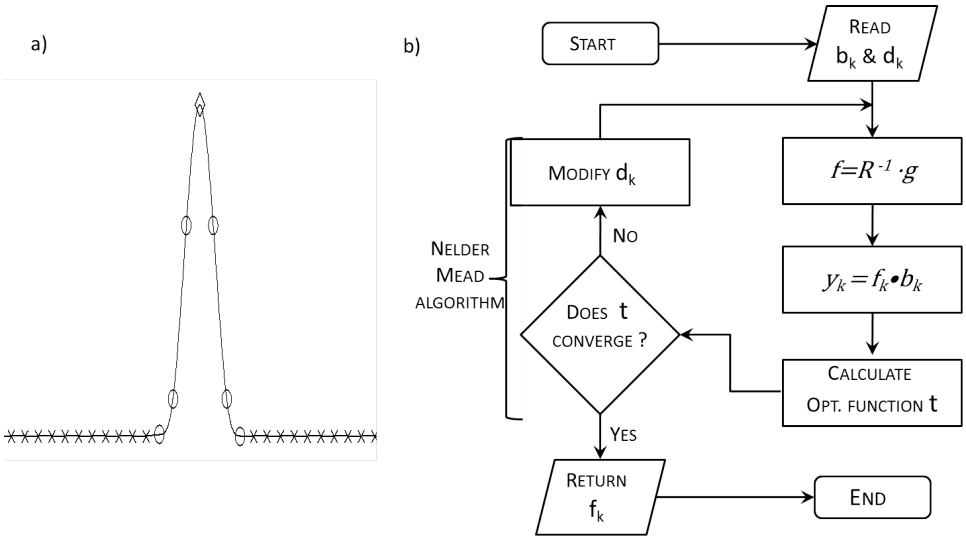

Figure 4.5. Inverse filter computation algorithm

transmitted waveform is applied. However, one should be aware that the designed filter will work perfectly only if no phase-shift is applied to the received waveform. This is almost never the case, since weather targets are usually affected by Doppler phase shift as well as a random sample-phase shift (due to reduction of sampling rate), which is uniformly distributed in range $\pm\pi$. As a consequence, a considerable degradation of filter performance occurs. This undesirable effect can be reduced if signal oversampling is applied (*Hwang and Keeler*, 1995). The effect of system phase noise should also be considered as shown by *Bharadwaj and Chandrasekar* (2012).

4.3 Pulse compressor design

4.3.1 Design methodology

The optimal design of a pulse compression weather system is a proper combination of radar waveform and compression filter. The type of observed weather should also be taken into consideration. Reflectivity gradients as high as $40dB/km$ can be observed in convective weather. The general approach is to guarantee that sidelobes are below the noise floor. Hence in this case the main objective is to reduce *PSL* below maximal

expected SNR within the Doppler range of interest ($\pm 40 m/s$). For X-band weather radar a PSL below 50 dB should eliminate sidelobe related data corruption if only weather targets are present. Strong returns from clutter targets may require even further PSL reduction. Fortunately, these sidelobes can be removed by means of clutter filtering. On the other hand, if a moderate precipitation event is observed, the main objective should be to minimize signal processing loss L_{mm}, while reducing PSL below 40 dB. This should be sufficient, since for a low-power radar, SNR in excess of 40dB is unlikely if $Z_H \leq 30 dBZ$. Finally, in case of severe weather observations such as tornadoes, an optimization function should put more weight on PSL and ΔR_{6dB} reduction.

The designed waveform is tested with the PTWR. Due to the system constraints it is desired to transmit a $20 \mu s$ chirp. Linear and nonlinear frequency modulated waveforms are tested using up to 3 MHz of bandwidth. A Tukey window can be applied to the transmitted pulse while operating in the saturation region of power amplifiers.

Based on the theory presented in the previous section, the compression filter depends on four parameters: the frequency modulation factor, α, amplitude modulation factor, γ, desired range resolution, ΔR_{6dB}, and filter length. Their effects on inverse filter performance in terms of figures of merit are illustrated in figures 4.6-4.8.

As shown in Fig.4.6a, tapering the edges of the transmitted pulse significantly decreases ISL. If an amplitude modulation is applied to more than 8% of pulse duration ($\gamma > 0.08$), an improvement of ISL in excess of $30 dB$ can be achieved compared with non-tapered pulse. This is caused by smoothing the waveform spectrum, which can be better approximated by an inverse filter function and does not depend on the applied frequency modulation. However, increasing the extent of amplitude modulation effectively wipes out the effect of the nonlinear frequency modulation, which is also applied mostly at the edges of transmitted waveform. Hence an increase in pro-

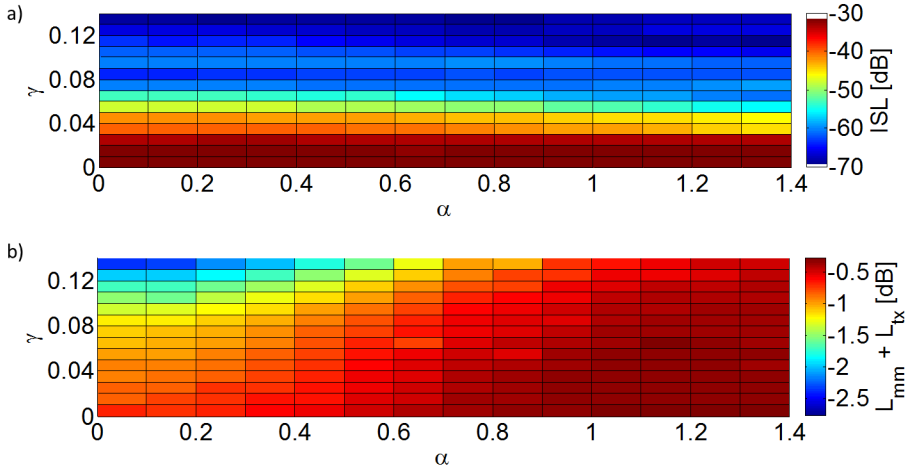

Figure 4.6. Inverse filter performance (200 taps, $\Delta R_{6dB} = 1.4ibw$) as a function of applied nonlinear frequency modulation α, and amplitude modulation γ: a) ISL b) processing loss

cessing loss will occur. As shown in Fig.4.6b, if $\alpha > 0.9$ the filter is almost matched ($L_{mm} \approx 0.2dB$) to the waveform without resorting to amplitude modulation. This is a direct consequence of a less rectangular spectrum. It is advised to keep frequency modulation factor, α, as low as possible, if better range resolution over mismatch loss improvement is preferred.

The range resolution can be arbitrarily defined as one of the optimization criteria in the Nelder-Mead algorithm. As presented in Fig.4.7, mismatch loss is minimized if $1.35ibw < \Delta R_{6dB} < 1.45ibw$. In consequence minor beam broadening occurs as compared to the matched filter ($\Delta R_{6dB} = 1.22ibw$) occur. Here it is worth pointing out that the common window functions (e.g. Hann) result in beam broadening greater than $1.85ibw$. The superior performance in range resolution of the inverse filter is due to the fact that it is applied to the entire spectrum of the processed signal, while common window functions are typically applied only to the relatively flat center part of the signal spectrum.

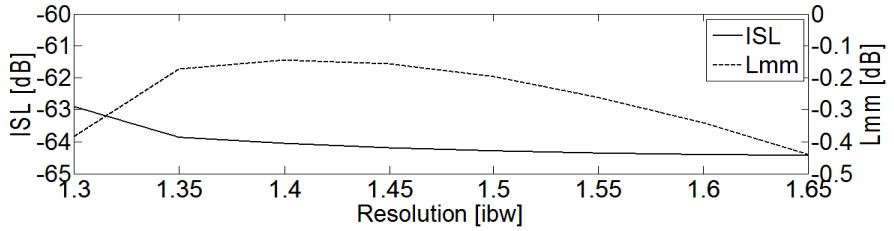

Figure 4.7. Inverse filter performance ($\alpha = 1.0, \gamma = 0.1$, 200 taps) versus 6_{dB} main lobe width for a point target.

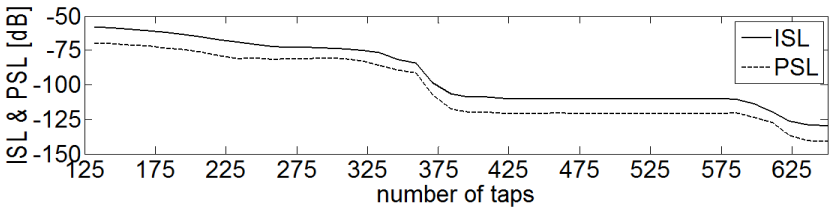

Figure 4.8. Inverse filter performance ($\alpha = 1.0, \gamma = 0.1, \Delta R_{6dB} = 1.4ibw$) versus filter length for a point target. The waveform length is T=126 taps. The inverse filter of length 1T,3T,5T,... significantly minimizes the energy in peak sidelobes.

Finally, the effect of filter length on inverse filter performance is shown in Fig.4.8. The biggest improvement in ISL can be obtained if energy in peak sidelobes is reduced rather than energy in the remaining sidelobes. This is illustrated by the steps in the characteristic. We observe that the energy in peak sidelobes is reduced, if the length of the filter is an odd multiple of the waveform length. In theory, longer filters enable extreme sidelobe reduction, but as mentioned in the previous section, this result is subject to detrimental effects of phase noise and Doppler shift. Typically, the procedure of designing a filter that is longer than the input signal involves zero-padding. This operation is equivalent to interpolation, and although it increases the number of points in FFT, no new information is added. Thus the effective improvement achieved by means of longer filters is in general limited.

4.4 Pulse compression performance verification

4.4.1 Theoretical performance evaluation

Figure 4.9 shows the ambiguity function for the NLFM waveform analyzed in the previous subsection. The peak sidelobes are at level -75 dB and the ISL is approximately -65 dB at zero Doppler shift. Since the input waveform is oversampled by $2.1 \cdot f_s$, the designed filter exhibits very low Doppler sensitivity keeping ISL below 60 dB within Doppler range of interest $\pm$ 50 m/s.

The downside of inverse filter implementation in a weather radar system is that it is designed for a specific sequence of a sampled continuous waveform, while the received signal can be represented by one out of an infinite set of sequences as a consequence of a finite sampling frequency. The shift in the sample-phase gradually deteriorates the output of the compression filter, resulting in an degraded range resolution. The worst case scenario occurs when the samples of received signals are located exactly between the respective samples of the transmitted waveform (*Hwang and Keeler*, 1995). If this is the case 6 dB mainlobe width broadens to $1.45ibw$. Additionally, as depicted in Figure 4.10, a degradation in *ISL* and *PSL* due to system jitter can be severe and it can not be compensated by an increased filter length. In fact, an inverse filter slightly longer than the transmitted waveform will perform almost always as well as a filter, which is several times longer than the transmitted waveform. Furthermore, it should be pointed out that the system jitter poses an important limitation on inverse filter performance. A system jitter of 0.9° is required in order to keep ISL below 40 dB.

4.4.2 Waveform and pulse compression evaluation using horn antenna

The performance of a window and an inverse filter applied to the frequency modulated waveform was tested using the setup presented in Figure 3.12. The tested waveform was transmitted from the PTWR and received by a horn antenna located 50 m away from the radar. The received X-band signal was then downconverted to

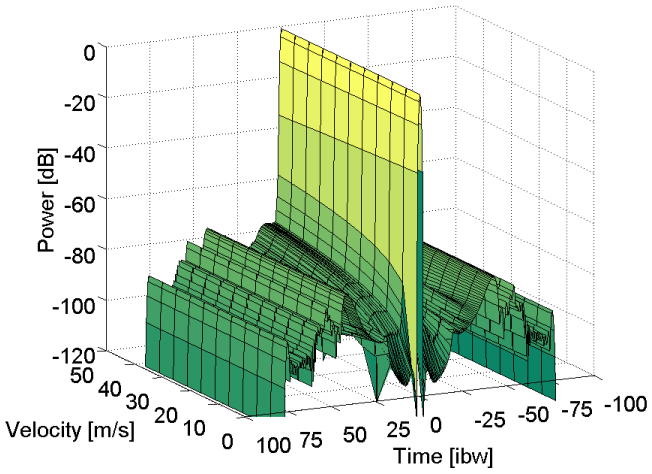

Figure 4.9. Ambiguity function of NLFM waveform ($\alpha = 1.0, \gamma = 0.1, \Delta R_{6dB} = 1.4ibw$, 200 taps). Very low Doppler sensitivity (ISL below 60 dB within Doppler range $\pm 50m/s$) can be achieved when oversampling is used.

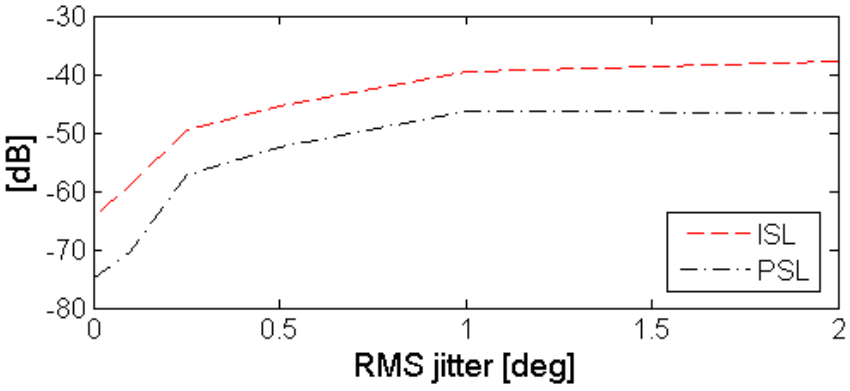

Figure 4.10. ISL and PSL as a function of a RMS system jitter for a NLFM waveform ($\alpha = 1.0, \gamma = 0.1, \Delta R_{6dB} = 1.4ibw$, 200 taps)

60 MHz and, using a long IF cable, sent back to the radar data acquisition card. This experiment was conducted in order to verify the shape of the transmitted waveform and its effect on pulse compression performance.

As shown in Figures 4.11 - 4.15, the implemented waveform exhibits an unwanted asymmetric amplitude modulation over its entire duration. The beginning of the waveform is about 2 dB below the saturation level and the power amplifiers require about $13\mu s$ to stabilize. This characteristic has been observed in multiple waveforms and it is assumed that the source of the distortion is the power supply subsystem. It is expected that the deformation of the waveform will have a moderate impact on inverse filter performance, since it is designed and optimized for the waveform under test. The influence on the window filter is expected to be minor.

The application of a Tukey window on transmit reduces Gibbs ripples in the power spectrum of the waveform under consideration. The additional advantage of tapering on transmit is visible in the shape of power spectrum, which becomes more rectangular as the γ factor is increased due to reduced spectral leakage effect. The reduced finite bandwidth has an effect on the power contained in the far range sidelobes, which decrease from -40 dBc ($\gamma = 0$; see Figure 4.11) to -90 dBc ($\gamma = 0.6$; see Figure 4.15).

The application of nonlinear frequency modulation impacts the shape of the part of the power spectrum which is related to the waveform bandwidth, while the roll-off of power spectrum edges is controlled using amplitude modulation. A linear frequency modulated waveform ($\alpha = 0$) has a relatively flat top part of the power spectrum (see Figure 4.11). In the case of nonlinear frequency modulated waveform (see Figures 4.12 - 4.15), the shape of the top part of the power spectrum can be approximated by an arc. The radius of the arc increases with the frequency modulation factor α. The more rounded spectrum shape is a reason that the peak sidelobe level can be reduced at no SNR penalty. However, as α is increased, range resolution will decrease.

Table 4.1 summarizes the performance of different pulse compression techniques applied to five waveforms. The common settings for all waveforms are: B=3 MHz, T=20 μs, and F_s=6.25 MHz. Both nonlinear ($\alpha = 1$) and linear ($\alpha = 0$) frequency modulations were tested. The power amplifiers were driven into saturation to maximize the radar's sensitivity. The impact of tapering the rising and falling edge of a waveform was tested using a Tukey window described by γ factor in range $0.0 - 0.6$. The performance of pulse compression is evaluated by 4 figures of merit: *SNR* loss, *PSL*, *ISL*, and ΔR_{6dB}. These parameters were computed after 16 pulses were accumulated and normalized. The SNR loss, which combines the loss due to the mismatched filter and windowing on transmit, is normalized to the output of a matched filter applied to the waveform with: $\alpha = 1$ and $\gamma = 0$. All figures of merit were computed using a theoretical waveform and the implemented waveform as a reference for a matched filter.

Hann and Blackman windows are commonly used in narrowband applications and were applied in both time and frequency domain. In the time domain, the window filter was applied to the copy of the transmitted waveform, while in the frequency domain, it was applied to its spectrum over the bandwidth of the waveform under test. The former method provides sidelobe reduction close to the theoretical value guaranteed by a window function, while the latter provides better range resolution and improved SNR at the cost of increased sidelobe level. The frequency domain approach is especially useful when short waveforms are considered. The inverse filter was designed to minimize ISL, while keeping ΔR_{6dB} below 100 m. The length of the filter was chosen to be three times larger than the transmitted waveform.

The performance of the inverse filter is subject to system jitter. Figure 4.16 illustrates this effect. The inverse filter was designed using a stored waveform of profile #1. When applied to the same profile, excellent sidelobe performance is achieved (ISL = -50.0 dB and PSL = -62.7 dB). The same filter was then used to compress the

waveform stored in profile #2. The effect of phase noise is clearly visible in sidelobes performance degradation (ISL = -38.1 dB and PSL = -43.8 dB), while the range resolution and SNR loss are not affected. This justifies the usage of the Nelder-Mead algorithm for inverse filter computation.

The Nelder-Mead technique is a heuristic search method and its performance is subject to start conditions. However, since sidelobe reduction is subject to noise, a highly accurate solution is not necessary. All that is desired is an improvement in function value, rather than full optimization.

As shown in Table 4.1, the performance of a window filter is roughly the same when the theoretical and recorded waveform is used as a matched filter. Sidelobe reduction over 50 dB is possible if a 3 dB loss in SNR is acceptable. However, as shown in Figure 4.15, implementation of a Blackman window causes significant degradation in range resolution. Under this condition, the peak sidelobes of a matched filter are within the range of the mainlobe of the windowed waveform. Hence, a careful inspection of the time domain output of pulse compressor is recommended. The best performance of the inverse filter is achieved if a recorded waveform is used for a filter design.

The SNR and range resolution are significantly improved when compared to the window based filters. The best performance was measured for a nonlinear chirp ($\alpha = 1$) with no amplitude modulation ($\gamma = 0$). The inverse filter is almost matched to the waveform (SNR loss = 0.2 dB) and peak sidelobes are below 42 dB, while the range resolution suffers only a minor degradation (83 m compared to 69 m for a matched filter output).

4.4.3 Pulse compression evaluation using volume target

Low power, solid-state radars present a promising solution for weather observation in mountainous areas. Observations close to the ground are crucial for an accurate flooding prediction in the valleys and are rarely provided by a current long range

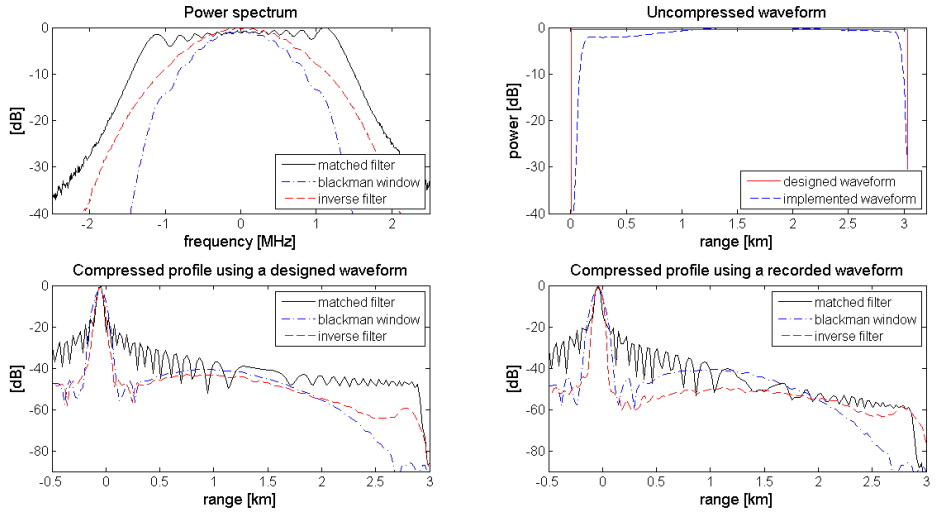

Figure 4.11. Comparison of pulse compression performance using a matched filter, a Blackman window, and an inverse filter. The pulse compression waveform is a linear chirp ($\alpha = 0$) and B = 3 MHz, T = 20 μs. Light amplitude modulation was applied to taper the rising and falling edge of the transmitted pulse ($\gamma = 0.1$).

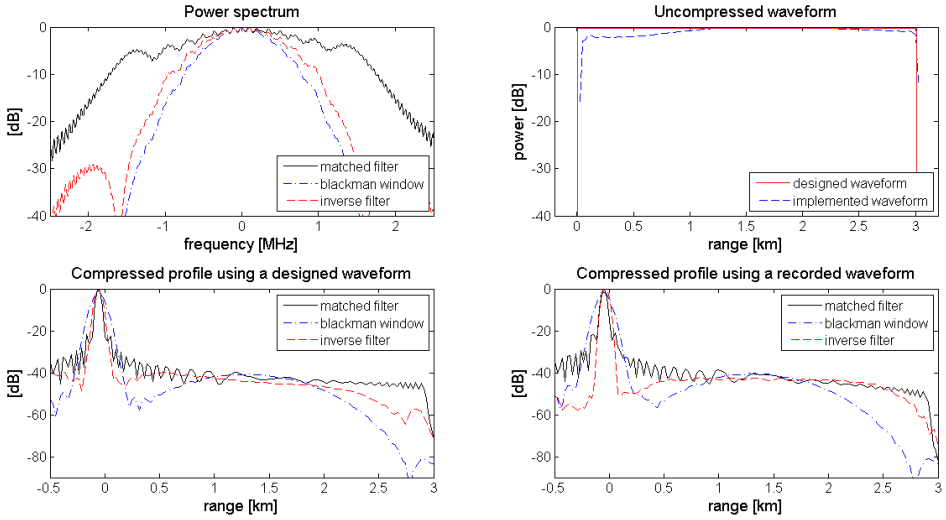

Figure 4.12. Comparison of pulse compression performance using a matched filter, a Blackman window, and an inverse filter. The pulse compression waveform is a nonlinear chirp ($\alpha = 1$) and B = 3 MHz, T = 20 μs. No amplitude modulation was applied.

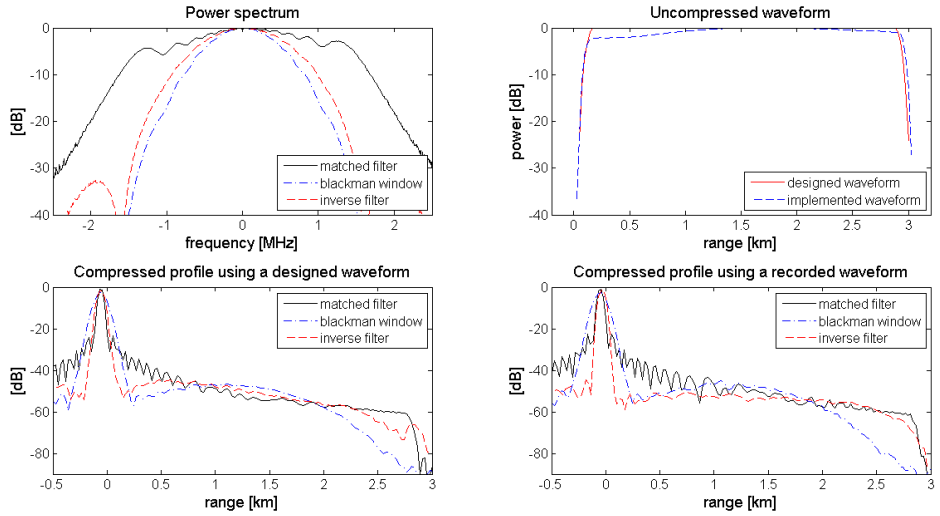

Figure 4.13. Comparison of pulse compression performance using a matched filter, a Blackman window, and an inverse filter. The pulse compression waveform is a nonlinear chirp ($\alpha = 1$) and B = 3 MHz, T = 20 μs. Light amplitude modulation was applied to taper the rising and falling edge of the transmitted pulse ($\gamma = 0.1$).

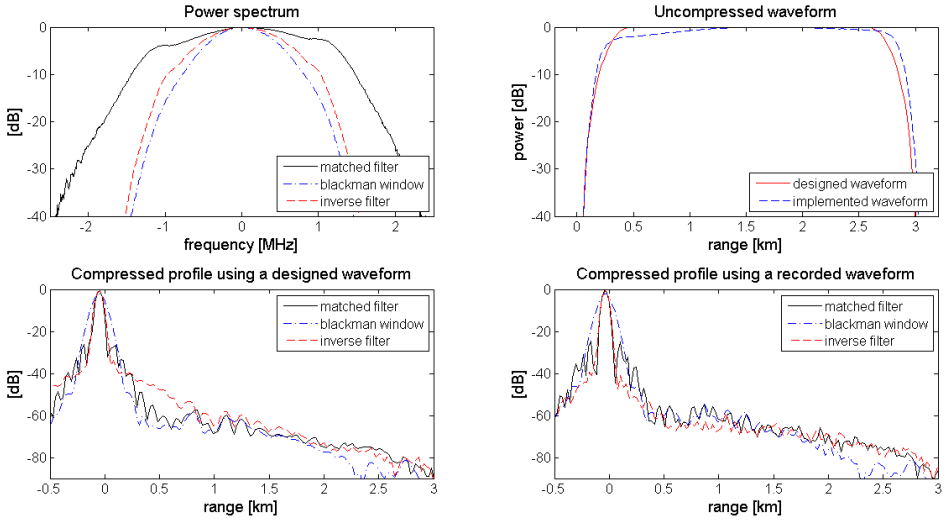

Figure 4.14. Comparison of pulse compression performance using a matched filter, a Blackman window, and an inverse filter. The pulse compression waveform is a nonlinear chirp ($\alpha = 1$) and B = 3 MHz, T = 20 μs pulse length. Moderate amplitude modulation was applied to taper the rising and falling edge of the transmitted pulse ($\gamma = 0.3$).

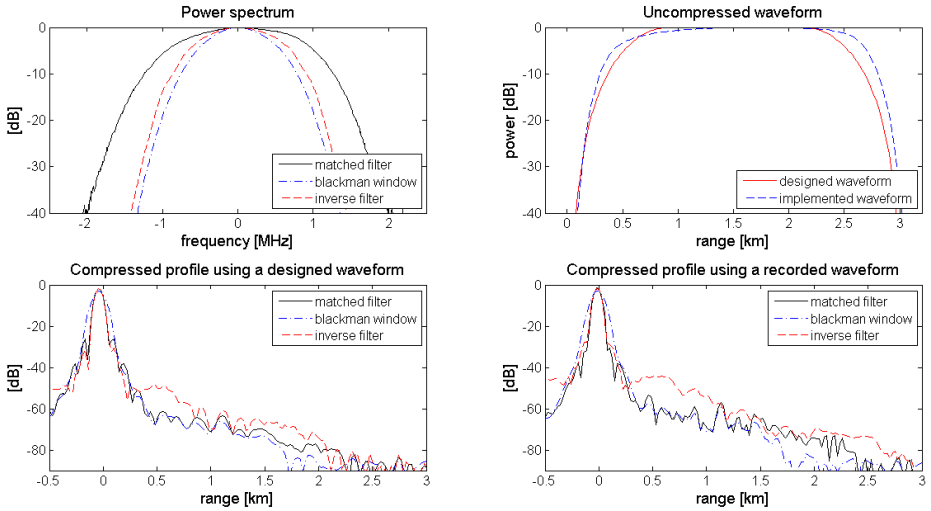

Figure 4.15. Comparison of pulse compression performance using a matched filter, a Blackman window, and an inverse filter. The pulse compression waveform is a nonlinear chirp ($\alpha = 1$) and B = 3 MHz, T = 20 μs pulse length. Strong amplitude modulation was applied to taper rising and falling edge of transmitted pulse ($\gamma = 0.6$).

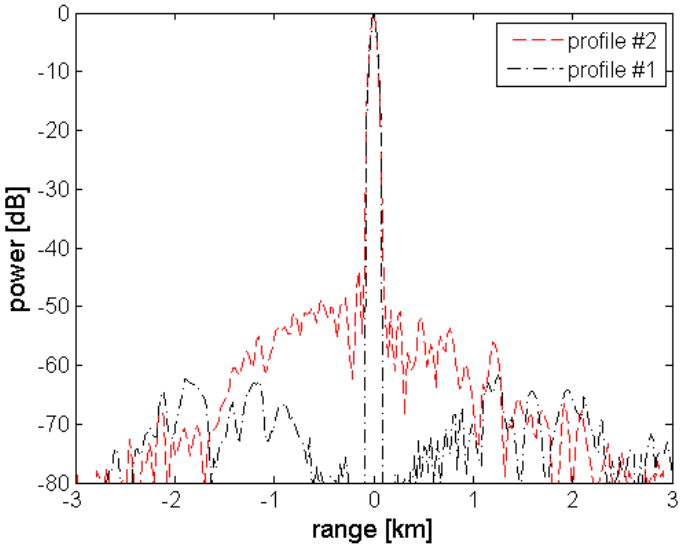

Figure 4.16. This inverse filter was designed using a stored waveform of profile #1. Pulse compressed waveform exhibits excellent sidelobes performance (ISL = -50.0 dB and PSL = -62.7 dB). The same filter was used to compress the waveform stored in profile #2. The effect of phase noise is clearly visible in sidelobes performance degradation (ISL = -38.1 dB and PSL = -43.8 dB).

Table 4.1. Pulse compression performance evaluation using FM waveform ($B = 3MHz, T = 20\mu s, F_s = 6.25MHz$). Hann and Blackman windows were applied to the matched filter in time domain (TD) and in frequency domain (FD) over the central 3 MHz.

	theoretical waveform				implemented waveform			
Filter type	**SNR loss [dB]**	**PSL [dB]**	**ISL [dB]**	ΔR_{6dB} **[m]**	**SNR loss [dB]**	**PSL [dB]**	**ISL [dB]**	ΔR_{6dB} **[m]**
LFM ($\alpha = 0$, $\gamma = 0.1$)								
Matched	0.51	−15.0	−11.4	65.6	0.22	−20.7	−14.5	69.5
Hann FD	0.87	−32.0	−19.4	87.8	0.90	−31.0	−21.1	91.4
TD	1.36	−33.7	−25.0	102.2	1.46	−38.5	−25.5	104.4
Blackman FD	1.32	−32.9	−20.4	100.1	1.34	−34.2	−23.2	102.6
TD	1.93	−38.5	−26.8	116.6	2.01	−38.8	−26.8	118.8
Inverse	1.00	−42.0	−27.9	77.8	0.76	−46.7	−32.56	79.2
NLFM ($\alpha = 1$, $\gamma = 0$)								
Matched	0.17	−21.7	−17.8	66.6	0	−21.2	−17.0	69.1
Hann FD	0.75	−34.5	−22.8	102.2	0.82	−34.3	−22.6	105.1
TD	1.16	−39.2	−26.0	119.5	1.31	−38.9	−26.0	123.8
Blackman FD	1.09	−33.8	−23.3	115.9	1.24	−33.9	−23.0	118.8
TD	1.69	−38.3	−26.3	140.0	1.84	−37.9	−26.3	144.4
Inverse	1.16	−37.5	−24.1	97.2	0.19	−42.3	−27.7	83.2
NLFM ($\alpha = 1$, $\gamma = 0.1$)								
Matched	0.97	−22.2	−19.2	69.8	0.90	−21.6	−18.6	72.0
Hann FD	1.52	−39.6	−29.6	101.9	1.61	−37.9	−28.5	104.8
TD	1.98	−43.9	−32.2	119.2	2.10	−43.4	−32.2	123.2
Blackman FD	1.91	−41.6	−31.3	115.2	1.99	−40.2	−29.9	118.4
TD	2.59	−44.3	−33.4	139.6	2.70	−42.7	−33.3	143.6
Inverse	1.72	−42.8	−30.8	96.5	0.99	−43.8	−33.6	79.6
NLFM ($\alpha = 1$, $\gamma = 0.3$)								
Matched	0.58	−25.5	−22.9	79.9	0.55	−24.0	−22.4	78.8
Hann FD	1.10	−32.8	−34.4	104.0	1.18	−39.5	−36.8	105.5
TD	1.61	−45.4	−42.7	120.6	1.69	−43.6	−40.4	123.5
Blackman FD	1.49	−43.3	−40.5	115.9	1.58	−41.8	−39.7	118.1
TD	2.16	−47.8	−46.4	140.0	2.26	−44.0	−41.4	143.6
Inverse	0.97	33.1	−30.7	95.4	0.83	−38.7	−36.0	77.4
NLFM ($\alpha = 1$, $\gamma = 0.6$)								
Matched	1.80	−24.6	−23.6	101.2	1.68	−29.0	−30.3	94.0
Hann FD	2.21	−29.1	−28.8	119.5	2.13	−37.2	−35.2	114.5
TD	2.64	−40.7	−39.0	133.9	2.52	−38.6	−38.7	131.2
Blackman FD	2.51	−32.0	−34.4	129.2	2.40	−38.3	−36.1	125.3
TD	3.09	−51.4	−46.7	150.0	3.02	−54.4	−45.4	148.3
Inverse	1.96	−29.0	−28.0	100.4	1.79	−26.1	−25.0	90.7

Figure 4.17. Radar deployment on 11/07/2013. Holyoke Range was chosen as a clutter target in order to provide high signal to noise ratio.

weather systems. Unfortunately, ground-level observations are usually contaminated with a response from stationary targets such as ground, buildings, radio towers, and mountains. These unwanted radar returns must be filtered out by means of a clutter filter. The traditional method is to apply a time-domain notch filter (*Torres and Zrnic*, 1999), which reduces the power of all signals, including weather returns, with zero Doppler velocity. The frequency domain filter proposed by *Siggia* (2004) reduces the signal-to-clutter-ratio (CSR) caused by a stationary target while recovering the weather spectrum around zero Doppler velocity at the cost of a significant increase in a computation time. However, as reported by *Cao et al.* (2012), clutter filtering could bias the weather signal and should not be applied at all times, especially if low Doppler velocities in weather targets are observed.

Pulse compression is implemented to the raw data input as the first step in a weather signal processing chain. Therefore, a low sidelobe compression filter might significantly reduce the necessity of clutter filtering, which is subject to signal-to-clutter-ratio. In a traditional weather system, clutter targets will only contaminate few range bins, which are tied to their physical presence. However, in a solid-state weather system utilizing pulse compression, a single clutter target can corrupt data in hundreds of range bins. This worst case scenario was evaluated using data collected

by the PTWR as shown in Figure 4.17. The duration of the transmitted pulse was $20\mu s$, which results in a 3 km blind zone range and a $\pm$ 3 km sidelobe contamination zone. Figure 4.18 presents a single compressed profile using different waveforms and compression filters. The clutter targets are present within a few gates around 4 km away from the radar site, but the sidelobe contamination extends up to 7 km.

Qualitative comparison of a non-tapered ($\gamma = 0$) against a tapered waveform ($\gamma = 0.1$) shows better far range sidelobe reduction if a Tukey window is applied independent of the compression technique used. Blackman window introduces visible beam broadening and can not resolve a target located around 3.9 km, which is clearly detected using a matched or an inverse filter. Pulse compression filters based on a recorded waveform described in the previous section were also evaluated. Quantitative comparison shows the improvement in range resolution and SNR if a filter based on the implemented waveform is utilized. This stands in good agreement with the results presented in Table 4.1. Finally, Figure 4.19 presents a PPI view of an illuminated area. The use of a Blackman window smears the data, which is related to the degradation in range resolution. An inverse filter implemented to a NLFM waveform with a light amplitude modulation ($\gamma = 0.1$) exhibits the best sidelobe reduction performance, which in consequence reduces the signal-to-clutter-ratio and removes the necessity of a clutter filter.

Sidelobe reduction plays an important role in severe weather analysis, where steep reflectivity gradients are possible. Range resolution helps to detect fine weather structures such as tornadoes. However, in the case of light stratiform rain or snow observations, emphasis should be put on improving signal-to-noise-ratio. This type of precipitation is characterized by low reflectivity gradients and usually extends over the entire field of view. Note that since noise power is subtracted from the received signal, sidelobe reduction which exceeds SNR level is sufficient.

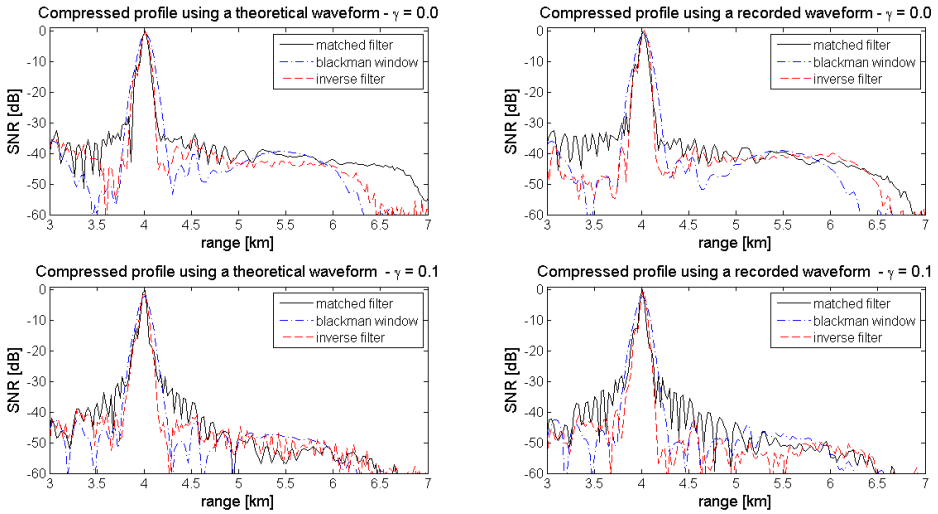

Figure 4.18. Comparison of pulse compression performance observing a clutter target using a matched filter, a Blackman window, and an inverse filter. The pulse compression waveform uses a nonlinear chirp ($\alpha = 1$) and B = 3 MHz, T = 20 μs. The inverse filter outperforms the window filter, providing better sidelobe reduction at the minimal cost of SNR reduction. Range resolution degradation is minimal if inverse filter is used instead of a Blackman filter.

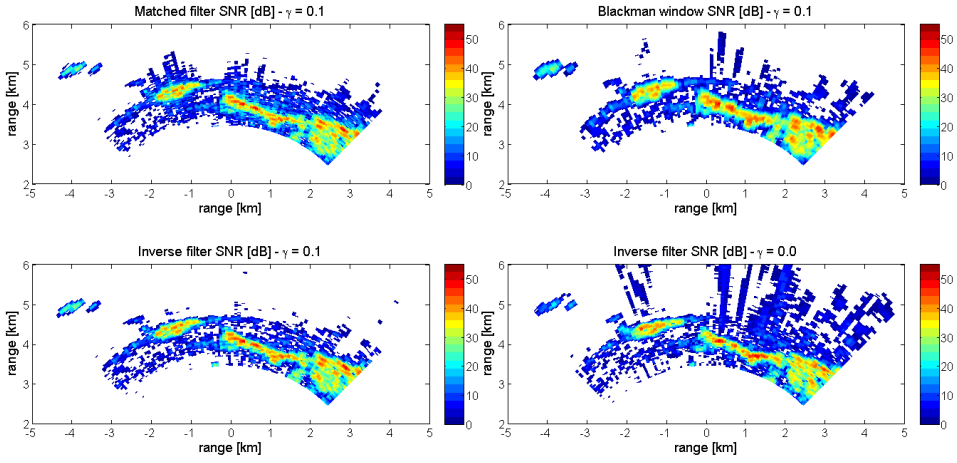

Figure 4.19. Comparison of pulse compression performance observing a clutter target using a matched filter, a Blackman window, and an inverse filter. An inverse filter implemented to a NLFM waveform with a light amplitude modulation ($\gamma = 0.1$) exhibits the best sidelobe reduction performance.

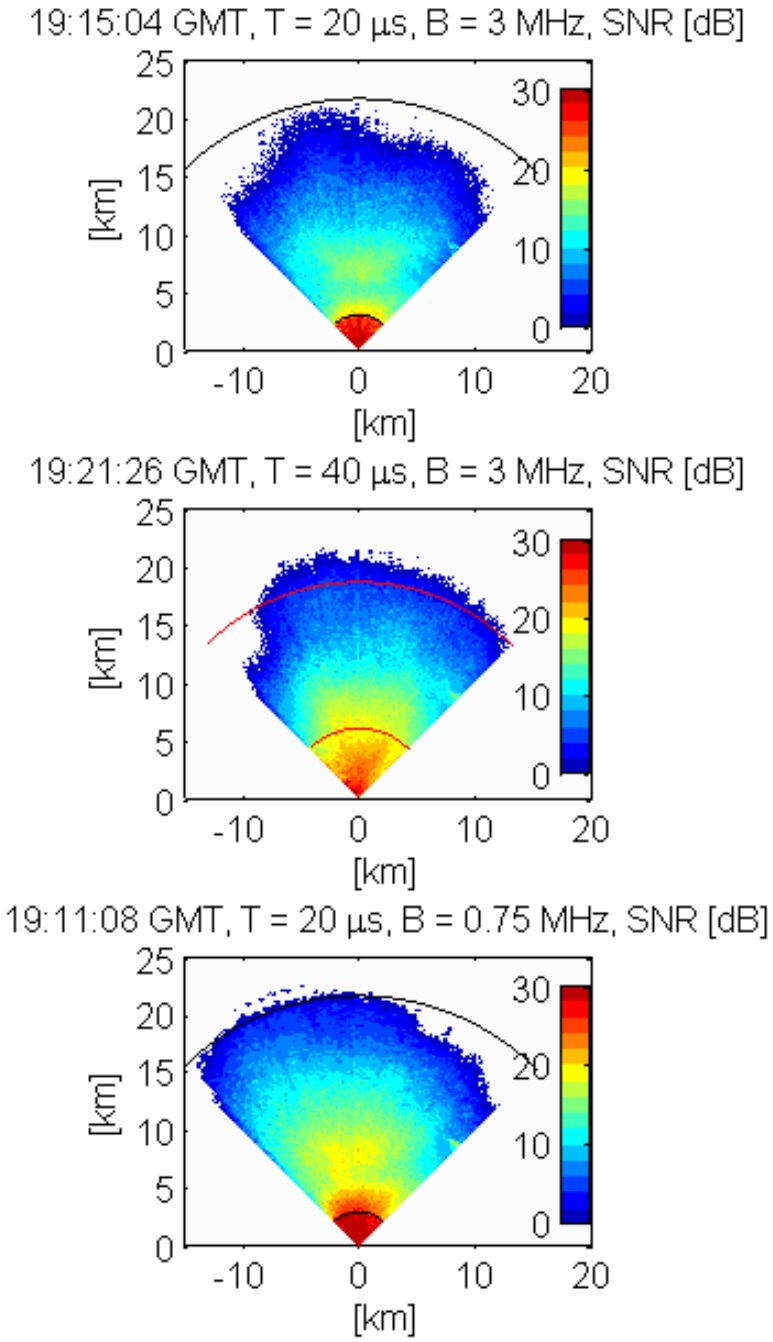

Figure 4.20. The PTWR observations of a light snow (reflectivity factor on order of 13 dBz) collected on 02/13/2014 in Hadley, Massachusetts. Three waveforms were tested over time span of 10 minutes allowing for a limited qualitative comparison. The black and red arcs indicate the boundaries of the first and second blind zones located at 3, 21 and 6, 18 km respectively.

Figure 4.20 presents the PTWR observations of light snow (reflectivity factor on order of 13 dBz) collected on 02/13/2014 in Hadley, Massachusetts. Three waveforms were tested over a time span of 10 minutes, allowing for a limited qualitative comparison. The upper panel presents a PPI SNR view of a matched filter output using a 20 μs waveform linearly swept over 3 MHz. The black arcs indicate the boundaries of the first and second blind zones, which are located at 3 and 21 km respectively. The middle panel shows a PPI SNR view of a matched filter output, but the waveform duration is 40 μs. A 3dB improvement in SNR can be detected. However, the boundaries of the first and second blind zones are now located at 6 and 18 km (depicted by red arcs) resulting in a 6 km reduction of the available field of view. Thus, only a limited improvement in far range detection is possible. Targets located over 18 km away from radar can be detected, but a full compression gain is not achieved. Finally, the lower panel presents a PPI SNR view of a matched filter output using a 20 μs waveform linearly swept over 0.75 MHz. The narrowband waveform provides a 6 dB SNR improvement compared with the first waveform at the cost of reduced range resolution. It is an acceptable trade off due to the homogeneity of the observed reflectivity fields.

In all three cases the SNR is almost always below 20 dB. In order to keep sidelobes below the noise floor it is suggested to use an NLFM waveform with $\alpha > 1$ and a matched filter. A similar result can be obtained with an LFM waveform compressed using a Hann window filter applied in the frequency domain. The SNR against sidelobe reduction performance can be optimized by adjusting level of pedestal (see Figure 4.4). It is evident that reduction of bandwidth over increasing pulse duration provides better SNR, while improving range of observations.

CHAPTER 5

BIAS REMOVAL FOR PHASED-ARRAY RADAR POLARIMETRY: THEORY AND APPLICATION FOR WEATHER RADAR

A common source of error intrinsic to the array antenna itself is a non-optimal cross-polarization isolation or mismatch of the beam patterns in the two polarizations. These are defined at the system design stage and can vary over time due to aging, temperature changes, and other effects. Another error is due to the misprojection of the co- and cross-polar fields onto the local horizontal and vertical directions. In the case of the PTWR architecture, synthesized beams remain in the principle plane of the array and hence the H and V polarizations remain orthogonal across the scan. However, they do rotate as the radar scans off-boresight at non-zero elevation angle, introducing a constant canting angle (see Figure 5.1b). Fortunately, this bias can be corrected by an appropriate multiplication of the measured scattering matrix with a rotation matrix.

5.1 Scanning geometry for 1-D phased array architecture

The dependence of the polarization orientation on scan angle is based on a model of a pair of crossed-dipoles located at the coordinate system origin as presented in Figure 5.1a. For consistency, we assume the same conditions and use the same terminology as in *Zhang et al.* (2009), who described polarization properties for 2D phased array architecture. The PTWR is an example of 1-D array architecture, which enables electronic scanning in the azimuth plane only, while the array is mechanically tilted in elevation.

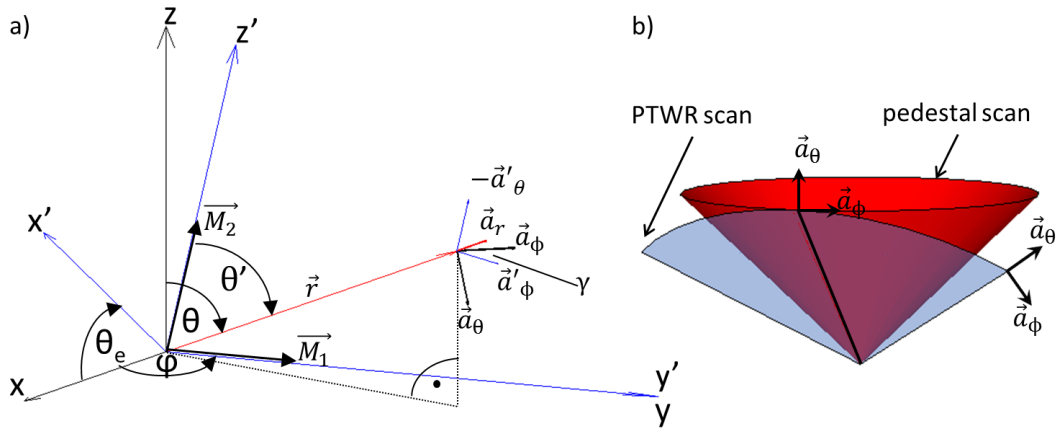

Figure 5.1. a) Spherical coordinate system for electric fields radiating from a pair of dipoles having moments $\underline{\boldsymbol{M_1}}$ and $\underline{\boldsymbol{M_2}}$. Unit vectors $\underline{\boldsymbol{a_\phi}}$, $\underline{\boldsymbol{a_\theta}}$, $\underline{\boldsymbol{a'_\phi}}$, $\underline{\boldsymbol{a'_\theta}}$ lie in the same plane perpendicular to $\underline{\boldsymbol{r}}$. In case of PTWR, $\theta' = 90°$.
b) Visualization of a radar field of view (elevation angle $\theta_e = 45°$) using standard pedestal scan and phase-tilt architecture. A 1-D phased-array radar PPI scan is a single face of a pyramid. This is principally different from a case of a mechanically rotated dish antenna system, which scans a section of a cone. H and V polarizations remain orthogonal across the scan, but they are not parallel and perpendicular to the ground respectively as one scans away from broadside.

In Figure 5.1a, the y-z plane is perpendicular to the ground, while the antenna aperture is in the $y^{'} - z^{'}$ plane. The coordinate system $X^{'}Y^{'}Z^{'}$ is obtained by rotation about the y-axis by the elevation angle θ_e. The $x^{'}$-axis represents the boresight of the radar system at elevation angle θ_e. $\overrightarrow{M_1}$ is the magnetic current density of a horizontally polarized radiating element, and $\overrightarrow{M_2}$ is the magnetic current density of a vertically polarized radiating element.

The following transformation relates the level and tilted coordinates in the Cartesian system:

$$\begin{aligned} \overrightarrow{a_x^{'}} &= \overrightarrow{a_x}\cos\theta_e + \overrightarrow{a_z}\sin\theta_e \\ \overrightarrow{a_y^{'}} &= \overrightarrow{a_y} \\ \overrightarrow{a_z^{'}} &= -\overrightarrow{a_x}\sin\theta_e + \overrightarrow{a_z}\cos\theta_e \end{aligned} \tag{5.1}$$

In the spherical coordinate system, unit vectors are defined as follows:

$$\begin{aligned} \overrightarrow{a_\phi^{'}} &= -\overrightarrow{a_x}\cos\theta_e\sin\phi' + \overrightarrow{a_y}\cos\phi' - \overrightarrow{a_z}\sin\theta_e\sin\phi' \\ \overrightarrow{a_\theta^{'}} &= \overrightarrow{a_x}\sin\theta_e - \overrightarrow{a_z}\cos\theta_e \end{aligned} \tag{5.2}$$

And, given that for the PTWR $\theta' = 90°$, unit vectors in terms of the tilted coordinate system are:

$$\begin{aligned} \overrightarrow{a_\phi^{'}} &= -\overrightarrow{a_x^{'}}\sin\phi' + \overrightarrow{a_y^{'}}\cos\phi' \\ \overrightarrow{a_\theta^{'}} &= -\overrightarrow{a_z^{'}} \end{aligned} \tag{5.3}$$

Projections of $\overrightarrow{a_\phi^{'}}$ and $\overrightarrow{a_\theta^{'}}$ onto the horizontal ($\overrightarrow{a_\phi}$) and vertical ($-\overrightarrow{a_\theta}$) directions yield:

$$
\begin{aligned}
\vec{a_\phi} \cdot \vec{a'_\phi} &= \cos\theta_e \sin\phi \sin\phi' + \cos\phi \cos\phi' = \cos\gamma \\
-\vec{a_\theta} \cdot \vec{a'_\phi} &= -\sin\gamma \\
\vec{a_\phi} \cdot \vec{a'_\theta} &= \sin\gamma \\
-\vec{a_\theta} \cdot \vec{a'_\theta} &= \cos\gamma
\end{aligned}
\tag{5.4}
$$

where angle γ defines the rotation of the local ,,horizontal" unit vector out of the horizontal plane. Furthermore, one can define the electric field at distance $\vec{r}$ away from $\overrightarrow{M_1}$ and $\overrightarrow{M_2}$ as:

$$
\begin{aligned}
\overrightarrow{E_1} &= E_{t1}[-\vec{a_x}\cos\theta_e \cos\phi' \sin\phi' + \vec{a_y}\cos^2\phi' - \vec{a_z}\sin\theta_e \cos\phi' \sin\phi'] = E_{t1}\cos\phi' \vec{a'_\phi} \\
\overrightarrow{E_2} &= E_{t2}[-\vec{a_x}\sin\theta_e + \vec{a_z}\cos\theta_e] = -E_{t2}\vec{a'_\theta} \\
E_{t1,2} &= \frac{k^2 e^{-jkr}}{4\pi\epsilon r} M_{1,2}
\end{aligned}
\tag{5.5}
$$

The factor $\cos\phi'$ in definition of E_1 indicates a reduction of intensity of the H field as the beam is directed away from broadside, which is a direct consequence of the dipole's electric field pattern. This effect can be measured during initial array calibration and included in the radar calibration constant on a beam by beam basis. An inspection of the electric fields E_1 and E_2 proves that both H and V polarizations remain orthogonal across the scan, since they are oriented along unit vectors $\vec{a'_\theta}$ and $\vec{a'_\phi}$. However, note that $\vec{a'_\phi}$ expressed in terms of the level coordinate system reveals a vertical component ($\vec{a_z}$), which is produced by a horizontal dipole $\overrightarrow{M_1}$. This is the source of bias in polarimetric products.

Finally, it is important to point out that the 1-D phased array radar PPI scan is a single face of a pyramid. This is principally different from the case of a mechanically rotated dish antenna system, which scans a section of a cone. In the case of the

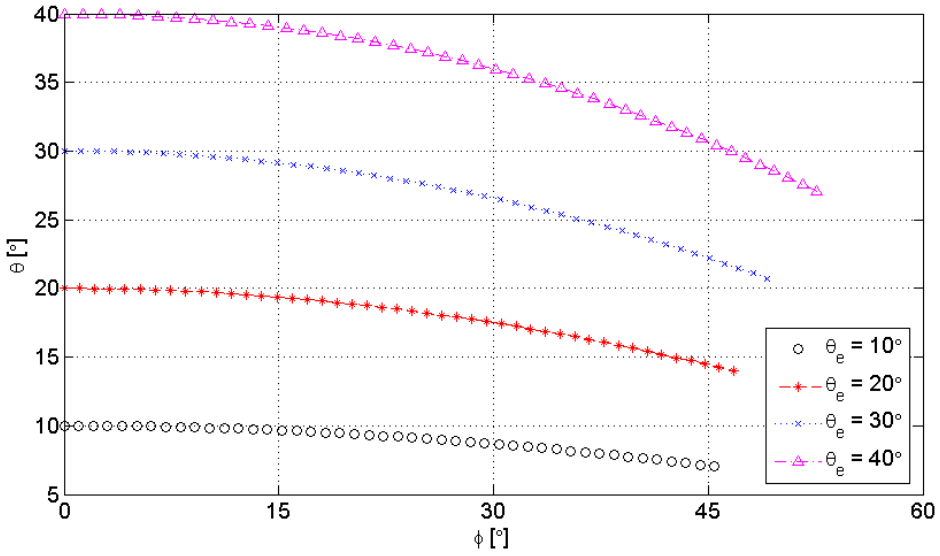

Figure 5.2. Effective radar beam direction (ϕ,θ) for various elevation tilts θ_e and radar defined azimuth angle $\phi^{'} = [0, 45]$.

PTWR, the effective beam elevation decreases θ from the requested elevation θ_e as the beam is directed away from broadside. Similarly, the effective azimuth ϕ increases from the requested azimuth $\phi^{'}$ as the beam is directed away from broadside. The effect is more evident at higher elevation angles (see Figure 5.2). The radar-defined beam direction ($\phi^{'}$,θ_e) is related to beam direction in the level coordinate system (ϕ,θ) as:

$$\phi = \arctan(\tan\phi^{'} \sec\theta_e) \tag{5.6}$$

$$\theta = \arccos(\cos\phi^{'} \sin\theta_e) \tag{5.7}$$

5.2 Scattering and rotation matrix

It is generally assumed that in most meteorological observations of interest, water drops take the form of oblate spheroids with a zero mean canting angle, that is, the angle between the incident electric field and the axis of symmetry of a water drop. In this case, the off-diagonal components of the backscattering matrix can be ignored. However, in the case of the PTWR, there is a constant non-zero canting angle due

to the orientation error in the polarization plane. This is a rather unusual phenomena observed in radar data (*Ryzhkov and Zrnic*, 2007). Canted hydrometeors cause depolarization of linearly polarized H and V waves, but the effect of depolarization on co-polar variables is negligible if the canting angle is on the order of a few degrees (*Ryzhkov*, 2001). Furthermore, *Zrnic et al.* (2010) showed that bias due to cross-polar and copolar radiation coupling is of higher importance in the case of the simultaneous transmit simultaneous receive (STSR) mode of operation. *Wang and Chandrasekar* (2006) also investigated a case of antenna feed alignment error, concluding that in the alternate mode of operation, orientation error up to 5 degrees can be tolerated if an error ΔZ_{DR} of 0.2 dB can be accepted.

Although the PTWR operates in the alternate transmit alternate receive (ATAR) mode, the self-induced canting angle due to polarization rotation can exceed 5 degrees (see Figure 5.3). For example, if the beam direction is set 45 degrees away from broadside and the array aperture is tilted by 10 degrees, then the canting angle is 7.1 degrees, which is equivalent to the apparent antenna cross-polarization isolation level (CPL) of around -18 dB. The cross-polarization isolation level and the polarization rotation angle are related as follows (*Wang and Chandrasekar*, 2006):

$$CPL = 20\log_{10}(\tan\gamma) \tag{5.8}$$

Under polarization rotation free conditions, the intrinsic radar backscattering matrix $S^{(b)}$ is defined as:

$$S^{(b)} = \begin{bmatrix} s_{hh}^{(b)} & s_{hv}^{(b)} \\ s_{hv}^{(b)} & s_{vv}^{(b)} \end{bmatrix} \tag{5.9}$$

Due to the symmetry of hydrometeors, it is assumed that $s_{hv}^{(b)} = s_{vh}^{(b)}$.

The transmission matrix, T, takes into account the effect of phase shift and attenuation due to wave propagation in atmosphere containing hydrometeors. The cross-

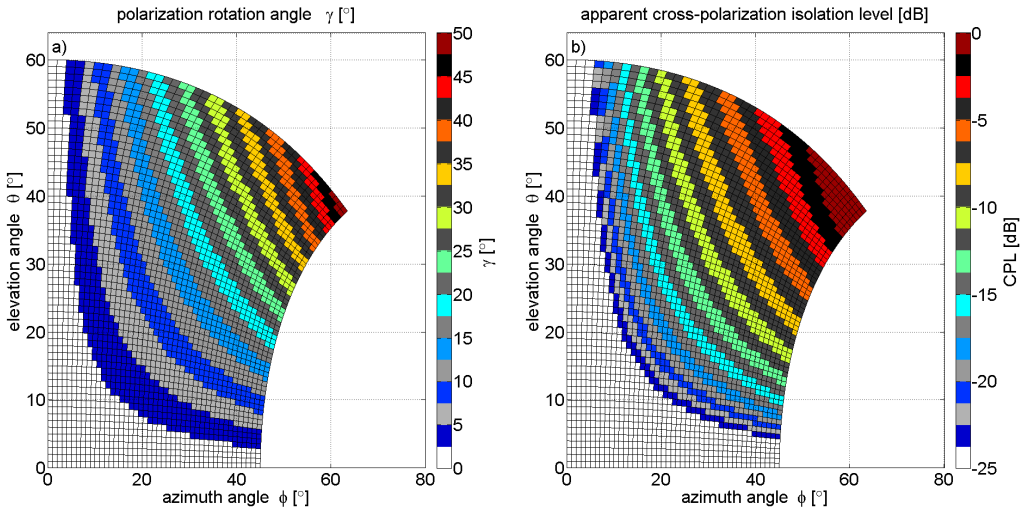

Figure 5.3. a) polarization rotation angle γ, and b) apparent cross-polarization isolation level for elevation tilts $\theta_e = [0, 60]$ and radar defined azimuth angle $\phi' = [0, 45]$.

coupling of the H and V fields is negligible and therefore the transmission matrix is assumed diagonal. It is defined as (*Doviak and Zrnic*, 1993):

$$T = \begin{bmatrix} T_{hh} & 0 \\ 0 & T_{vv} \end{bmatrix} \tag{5.10}$$

If the forward and back propagation effect is included, the received backscattering matrix is modified to (*Zrnic et al.*, 2011):

$$S' = TS^bT = \begin{bmatrix} T_{hh}^2 s_{hh}^{(b)} & T_{hh}T_{vv}s_{hv}^{(b)} \\ T_{hh}T_{vv}s_{hv}^{(b)} & T_{vv}^2 s_{vv}^{(b)} \end{bmatrix} = \begin{bmatrix} s'_{hh} & s'_{hv} \\ s'_{hv} & s'_{vv} \end{bmatrix} \tag{5.11}$$

The effect of polarization rotation can be included by the introduction of a rotation matrix:

$$P(\gamma) = \begin{bmatrix} p_{11} & p_{12} \\ p_{21} & p_{22} \end{bmatrix} = \begin{bmatrix} \cos\gamma & \sin\gamma \\ -\sin\gamma & \cos\gamma \end{bmatrix} \tag{5.12}$$

The rotation matrix is Toeplitz and has the following properties:

$$\begin{aligned} P(\gamma) &= P^{-1}(-\gamma) = P^{T}(-\gamma) \\ P(-\gamma) &= P^{-1}(\gamma) = P^{T}(\gamma) \end{aligned} \tag{5.13}$$

The backscattering matrix including polarization rotation effect, S^p, is given by:

$$\begin{aligned} S^p &= P(-\gamma)TP(\gamma)P(-\gamma)S^bP(\gamma)P(-\gamma)TP(\gamma) \\ &= P(-\gamma)TS^bTP(\gamma) \\ &= P(-\gamma)S'P(\gamma) \end{aligned} \tag{5.14}$$

If it is noted that $p_{11} = p_{22}$ and $p_{12} = -p_{21}$, then the biased backscattering matrix for the PTWR is given by:

$$S^p = \begin{bmatrix} p_{11}^2 s'_{hh} + p_{21}^2 s'_{vv} + 2p_{11}p_{21}s'_{hv} & p_{11}p_{21}(s'_{vv} - s'_{hh}) + (p_{11}^2 - p_{21}^2)s'_{hv} \\ p_{11}p_{21}(s'_{vv} - s'_{hh}) + (p_{11}^2 - p_{21}^2)s'_{hv} & p_{21}^2 s'_{hh} + p_{11}^2 s'_{vv} - 2p_{11}p_{21}s'_{hv} \end{bmatrix} \tag{5.15}$$

For most meteorological observations, hydrometeors have a vertical axis of symmetry, and therefore $s_{hv}^{(b)} = s_{vh}^{(b)} = 0$ (*Lei et al.*, 2013). Thus, (5.15) can be simplified to:

$$S^p = P^T(\gamma)S'P(\gamma) = \begin{bmatrix} p_{11}^2 s'_{hh} + p_{21}^2 s'_{vv} & p_{11}p_{21}(s'_{vv} - s'_{hh}) \\ p_{11}p_{21}(s'_{vv} - s'_{hh}) & p_{21}^2 s'_{hh} + p_{11}^2 s'_{vv} \end{bmatrix} \tag{5.16}$$

Theoretically, the unbiased backstattering matrix S' can be recovered by a simple multiplication with the inverse of rotation matrix as:

$$S' = (P^T(\gamma))^{-1}S^{(p)}P^{-1}(\gamma) = C^T S^{(p)} C \tag{5.17}$$

where the correction matrix C is defined as:

$$C = P^{-1}(\gamma) = \begin{bmatrix} \cos\gamma & -\sin\gamma \\ \sin\gamma & \cos\gamma \end{bmatrix}. \tag{5.18}$$

However, the biased backscattering matrix S^p defined in (5.16) can not be measured simultaneously by the PTWR. In general, four pulses separated by pulse repetition time T_s are required to establish S^p. The phase shifts caused by the scatterers' motion are different in consecutive measurements. Hence the backscattering matrix has to be adjusted for the Doppler effect before polarization correction can be applied (*Zrnic et al.*, 2011). Additionally, so far only the effect of the fields' misprojection has been considered. The antenna pattern is beam and polarization dependent and is characterized during initial system calibration, resulting in a set of calibration factors ($C_{HH}(\phi')$, $C_{HV}(\phi')$,$C_{VH}(\phi')$,$C_{VV}(\phi')$). If both effects are included, then the biased backscattering matrix S^p can be defined as:

$$\begin{aligned} S^{(p)} &= \begin{bmatrix} C_{HH}(\phi')s_{hh}^{(p)}(2i) & C_{HV}(\phi')s_{hv}^{(p)}(2i+3) \\ C_{VH}(\phi')s_{vh}^{(p)}(2i+2) & C_{VV}(\phi')s_{vv}^{(p)}(2i+1) \end{bmatrix} \\ &= \begin{bmatrix} C_{HH}(\phi')s_{hh}^{(p)}(2i) & C_{HV}(\phi')e^{-j2k_0v3T_s}s_{hv}^{(p)}(2i) \\ C_{VH}(\phi')e^{-j2k_0v2T_s}s_{vh}^{(p)}(2i) & C_{VV}(\phi')e^{-j2k_0v1T_s}s_{vv}^{(p)}(2i) \end{bmatrix} \end{aligned} \tag{5.19}$$

where v is the radial velocity, and the arguments *2i,2i+1,2i+2,2i+3* denote radar pulse indices.

Finally, under the assumption that $s_{hv}^{(b)} = s_{vh}^{(b)} = 0$, only the diagonal terms of the backscattering matrix are necessary in order to compute the unbiased standard weather radar products. First, the Doppler effect correction and the antenna pattern calibration factor should be implemented. Then, the unbiased elements of the backscattering matrix (s'_{hh}, s'_{vv}) can be simply obtained as follows:

$$
\begin{aligned}
s'_{hh} &= \frac{s^{(p)}_{vv} - \left(\frac{p_{11}}{p_{21}}\right)^2 s^{(p)}_{hh}}{p^2_{21} - \frac{p^4_{11}}{p^2_{21}}} \\
s'_{vv} &= \frac{s^{(p)}_{vv} - \left(\frac{p_{21}}{p_{11}}\right)^2 s^{(p)}_{hh}}{p^2_{11} - \frac{p^4_{21}}{p^2_{11}}}
\end{aligned}
\tag{5.20}
$$

5.3 Impact of polarization rotation on polarimetric observations in ATAR mode of operation.

The difference in antenna gain between copolar channels is addressed during the initial system calibration. In this section, the bias in reflectivity, differential reflectivity, correlation coefficient, specific differential phase, and linear depolarization ratio due to apparent canting angle when the beam is scanned away from broadside will be analyzed. This study assumes uniform beam filling and homogeneous scatter distribution.

5.3.1 Reflectivity and differential reflectivity factor

The horizontal and vertical reflectivity factors $Z'_{h,v}$ measured under no polarization rotation condition are defined as:

$$
Z'_{h,v} = \frac{4\lambda N}{\pi |K_w|^2} \left\langle \left| s'_{hh,vv} \right|^2 \right\rangle \tag{5.21}
$$

where N is the number density of scatters per unit volume, λ is the wavelength, and K_w is the complex refractive index of water. The definition of $Z'_{h,v}$ includes the propagation effects.

Using the definitions given in (5.16) and (5.21), the reflectivity factors measured by a phase-tilt radar are:

$$
\begin{aligned}
Z_h^{(p)} &= \frac{4\lambda N}{\pi |K_w|^2} \left\langle \left| s_{hh}^{(p)} \right|^2 \right\rangle \\
&= \frac{4\lambda N}{\pi |K_w|^2} \left\langle \left| p_{11}^2 s'_{hh} + p_{21}^2 s'_{vv} \right|^2 \right\rangle \\
&= p_{11}^4 Z'_h + p_{21}^4 Z'_v + 2\sqrt{Z'_h Z'_v} Re[\rho'_{hv}] p_{11}^2 p_{21}^2 \\
&= cos^4(\gamma) Z'_h + sin^4(\gamma) Z'_v + \frac{1}{2}\sqrt{Z'_h Z'_v} Re[\rho'_{hv}] sin^2(2\gamma)
\end{aligned}
\tag{5.22}
$$

$$
\begin{aligned}
Z_v^{(p)} &= \frac{4\lambda N}{\pi |K_w|^2} \left\langle \left| s_{vv}^{(p)} \right|^2 \right\rangle \\
&= \frac{4\lambda N}{\pi |K_w|^2} \left\langle \left| p_{11}^2 s'_{vv} + p_{21}^2 s'_{hh} \right|^2 \right\rangle \\
&= p_{21}^4 Z'_h + p_{11}^4 Z'_v + 2\sqrt{Z'_h Z'_v} Re[\rho'_{hv}] p_{11}^2 p_{21}^2 \\
&= sin^4(\gamma) Z'_h + cos^4(\gamma) Z'_v + \frac{1}{2}\sqrt{Z'_h Z'_v} Re[\rho'_{hv}] sin^2(2\gamma)
\end{aligned}
\tag{5.23}
$$

Further, the differential reflectivity factor Z'_{DR} measured under no polarization rotation condition is defined as:

$$
Z'_{DR} = 10 \log_{10} \left(\frac{\left\langle \left| s'_{hh} \right|^2 \right\rangle}{\left\langle \left| s'_{vv} \right|^2 \right\rangle} \right) \tag{5.24}
$$

Using the definitions given in (5.16) and (5.24), the differential reflectivity factor measured by a phase-tilt radar is:

$$
\begin{aligned}
Z_{DR}^{(p)} &= 10\log_{10}\left(\frac{\left\langle\left|s_{hh}^{(p)}\right|^2\right\rangle}{\left\langle\left|s_{vv}^{(p)}\right|^2\right\rangle}\right) \\
&= 10\log_{10}\left(\frac{p_{11}^4 Z'_h + p_{21}^4 Z'_v + \frac{1}{2}\sqrt{Z'_h Z'_v}Re[\rho'_{hv}]sin^2(2\gamma)}{p_{21}^4 Z'_h + p_{11}^4 Z'_v + \frac{1}{2}\sqrt{Z'_h Z'_v}Re[\rho'_{hv}]sin^2(2\gamma)}\right) \\
&= 10\log_{10}\left(\frac{cos^4(\gamma)Z'_{dr} + sin^4(\gamma) + \frac{1}{2}\sqrt{Z'_{dr}}Re[\rho'_{hv}]sin^2(2\gamma)}{sin^4(\gamma)Z'_{dr} + cos^4(\gamma) + \frac{1}{2}\sqrt{Z'_{dr}}Re[\rho'_{hv}]sin^2(2\gamma)}\right)
\end{aligned}
\tag{5.25}
$$

The retrieval biases for radar reflectivity and differential reflectivity are defined as:

$$
\begin{aligned}
\Delta Z_{h,v} &= 10\log_{10}\left(\frac{Z_{h,v}^{(p)}}{Z'_{h,v}}\right) \\
\Delta Z_{DR} &= 10\log_{10}\left(\frac{Z_{dr}^{(p)}}{Z'_{dr}}\right)
\end{aligned}
\tag{5.26}
$$

where $Z_{h,v}^{(p)}$, $Z'_{h,v}$, $Z_{dr}^{(p)}$, and Z'_{dr} are given in linear scale.

Equations (5.22), (5.23), (5.25) reveal that $Z_h^{(p)}$, $Z_v^{(p)}$ and $Z_{DR}^{(p)}$ depend on Z'_h and Z'_v as well as ρ'_{hv} and rotation matrix P. Figure 5.4 shows the reflectivity and differential reflectivity bias, for the ATAR mode, as a function of polarization rotation angle γ. Parameters used in the calculation are: (a)-(c) $Z_{DR} = 1dB$, (d)-(f) $Z_{DR} = 3dB$, and $\rho_{hv} = 0.98$, $0^\circ \leq \gamma \leq 45^\circ$ in all cases. The biases are more pronounced with increasing Z_{DR} and rotation angle γ. It can be seen that the horizontal reflectivity factor is always biased low. The bias in vertical reflectivity can be either positive or negative, depending on the differential propagation phase ϕ_{dp}. The differential reflectivity is biased low. This parameter is related to the oblateness of the hydrometeors. Note that for $\gamma = 45^\circ$, the return from both polarizations is expected to be the same, and hence $Z_{DR}^{(p)} = 0dB$. This is clearly visible in Figure 5.4c where $\Delta Z_{DR}(\gamma = 45^\circ) = -1dB$ and Figure 5.4f where $\Delta Z_{DR}(\gamma = 45^\circ) = -3dB$. Finally, it is evident that if $\gamma \leq 10^\circ$, the bias in $\Delta Z_{DR} \leq 0.1dB$. This corresponds to the

radar field of view where the tilt angle $\Theta_e < 10^\circ$ (see Figure 5.3), which is where quantitative measurements of precipitation are required.

5.3.2 Correlation coefficient

The correlation coefficient between horizontally and vertically oriented waves ρ_{hv} provides important information for discrimination of echoes of meteorological significance. High values of ρ_{hv} in excess of 0.97 indicate the presence of uniformly shaped hydrometeors such as rain drops, while ρ_{hv} values in range 0.8 to 0.97 denote region filled with scatterers which are characterized by non-uniform shapes, such as snow and hail. The correlation coefficient is also useful in detection of non-meteorological targets such as birds and ground clutter, which, due to their complex shapes are indicated by ρ_{hv} values below 0.8. The correlation coefficient depends on the shape, oscillation, wobbling, and canting angle distribution of hydrometeors (*Sachidananda and Zrnic*, 1985).

The measured co-polar correlation coefficient ρ'_{hv} under no polarization rotation condition is defined as:

$$\rho'_{hv} = \frac{\left\langle s'^{*}_{hh} s'_{vv} \right\rangle}{\sqrt{\left\langle \left| s'_{hh} \right|^2 \right\rangle \left\langle \left| s'_{vv} \right|^2 \right\rangle}} = \rho_{hv} \exp(j\phi_{dp}) \tag{5.27}$$

Using the definitions given in (5.16) and (5.27), the correlation coefficient measured by a phase-tilt radar is:

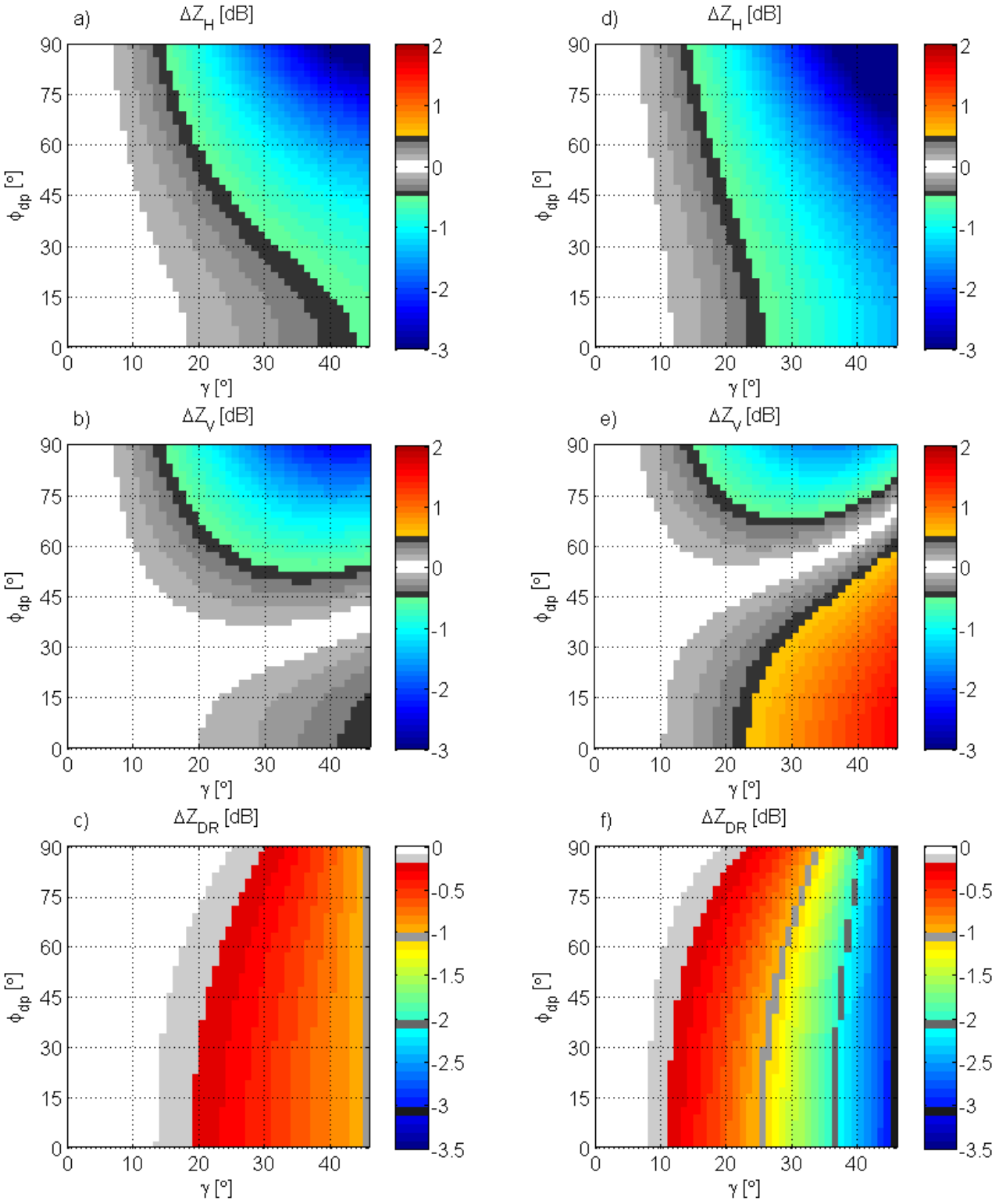

Figure 5.4. Dependence of reflectivity and differential reflectivity bias on the polarization rotation angle γ. Parameters used in the calculation are: (a)-(c) $Z_{DR} = 1dB$, (d)-(f) $Z_{DR} = 3dB$, and $\rho_{hv} = 0.98$ in all cases. White indicates region where bias is less than 0.1 dB.

$$
\begin{aligned}
\rho_{hv}^{(p)} &= \frac{\left\langle s_{hh}^{(p)*} s_{vv}^{(p)} \right\rangle}{\sqrt{\left\langle \left| s_{hh}^{(p)} \right|^2 \right\rangle \left\langle \left| s_{vv}^{(p)} \right|^2 \right\rangle}} \\
&= \frac{\left\langle \left(p_{11}^2 s'_{hh} + p_{21}^2 s'_{vv}\right)^* \left(p_{11}^2 s'_{vv} + p_{21}^2 s'_{hh}\right) \right\rangle}{\sqrt{\left\langle \left| p_{11}^2 s'_{hh} + p_{21}^2 s'_{vv} \right|^2 \right\rangle \left\langle \left| p_{11}^2 s'_{vv} + p_{21}^2 s'_{hh} \right|^2 \right\rangle}} \\
&= \frac{p_{11}^2 p_{21}^2 (Z_{dr}^{'-1/2} + Z_{dr}^{'1/2}) + p_{11}^4 \rho'_{hv} + p_{21}^4 \rho'^*_{hv}}{\sqrt{\left(p_{11}^4 + p_{21}^4 Z_{dr}^{'-1} + 2p_{11}^2 p_{21}^2 Re[\rho'_{hv}] Z_{dr}^{'-1/2}\right)\left(p_{12}^4 Z'_{dr} + p_{11}^4 + 2p_{11}^2 p_{21}^2 Re[\rho'_{hv}] Z_{dr}^{'1/2}\right)}} \\
&= \frac{\frac{1}{4} sin^2(2\gamma)(Z_{dr}^{'-1/2} + Z_{dr}^{'1/2}) + cos^4(\gamma)\rho'_{hv} + sin^4(\gamma)\rho'^*_{hv}}{\sqrt{\left(cos^4(\gamma) + sin^4(\gamma) Z_{dr}^{'-1} + \frac{1}{2} sin^2(2\gamma) Re[\rho'_{hv}] Z_{dr}^{'-1/2}\right)\left(sin^4(\gamma) Z'_{dr} + cos^4(\gamma) + \frac{1}{2} sin^2(2\gamma) Re[\rho'_{hv}] Z_{dr}^{'1/2}\right)}}
\end{aligned}
\tag{5.28}
$$

The correlation coefficient $\rho_{hv}^{(p)}$ is biased high and depends on Z'_{dr}, ρ_{hv} and rotation angle γ. The dependence of $\rho_{hv}^{(p)}$ on Z'_{dr} is negligible within the range of Z'_{dr} expected for meteorological targets. The bias in $\rho_{hv}^{(p)}$ is more significant for lower values of ρ_{hv} as shown in Figure 5.5, which compares $\rho_{hv}^{(p)}$ simulated for (a) hail and (b) rain cases. Based on a typical setting of hydrometeor-type classification boundaries (*Liu and Chandrasekar*, 2000), *Wang and Chandrasekar* (2006) defined that the correct classification of rain, hail, and bright band observations requires bias in the correlation coefficient to be less than 2%, 5% and 10% respectively. This condition is satisfied in all cases as long as $\gamma \leq 20°$.

5.3.3 Specific differential phase

Specific differential phase K_{dp} is defined as a range derivative of differential propagation phase ϕ_{dp}. The typical range of values spans from -2 to 7 $°/km$. Most meteorological targets of interest such as raindrops are horizontally oriented and thus produce a positive K_{dp}. Negative K_{dp} can be caused by vertically-oriented ice crystals, and is also related to a strong electrical activity within the storm (*Ryzhkov and Zrnic*, 2007). *Chandrasekar et al.* (1990) showed that a K_{dp} based rain rate estimator performs better than Z_H and Z_{DR} based estimators, especially at higher rain rates due to the fact that it depends not only on hydrometeor shapes, but also their con-

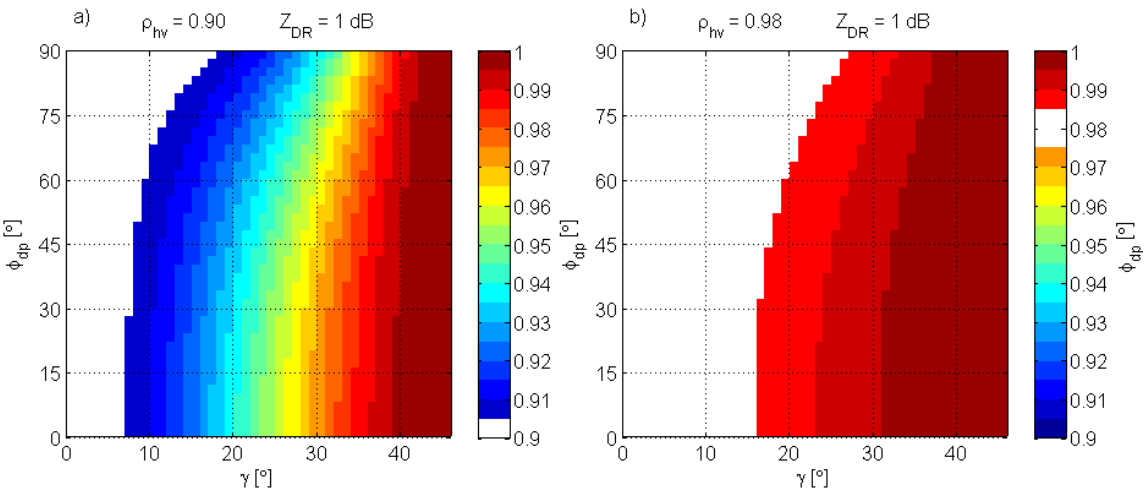

Figure 5.5. $\rho_{hv}^{(p)}$ of a phase-tilt radar for a) hail b) rain case. $Z_{DR} = 1dB$ in all cases.

centration. Additionally, K_{dp} is neither affected by system absolute calibration nor by rain-induced attenuation.

The retrieval bias in differential propagation phase shift is defined as:

$$\Delta\phi_{dp} = \phi_{dp}^{(p)} - \phi_{dp} \tag{5.29}$$

where $\phi_{dp}^{(p)} = \arg(\rho_{hv}^{(p)})$. The slope of $\Delta\phi_{dp}$ with respect to ϕ_{dp} can be defined as the relative error in K_{dp} as:

$$\frac{\Delta K_{dp}}{K_{dp}} = \frac{d\Delta\phi_{dp}}{d\phi_{dp}} \tag{5.30}$$

Wang and Chandrasekar (2006) have shown that the relative error in K_{dp} due to cross polarization isolation exhibits a negligible dependence on precipitation type. Given the typical measurement accuracy, they suggest the accuracy constraint on ΔK_{dp} should be less than 10%. Figure 5.6 presents the relative error in K_{dp} as a function of rotation angle γ and differential propagation phase ϕ_{dp}. It can be seen that the relative error in K_{dp} is below 10% for $\gamma \leq 13°$. Note that for $\gamma = 45°$, the

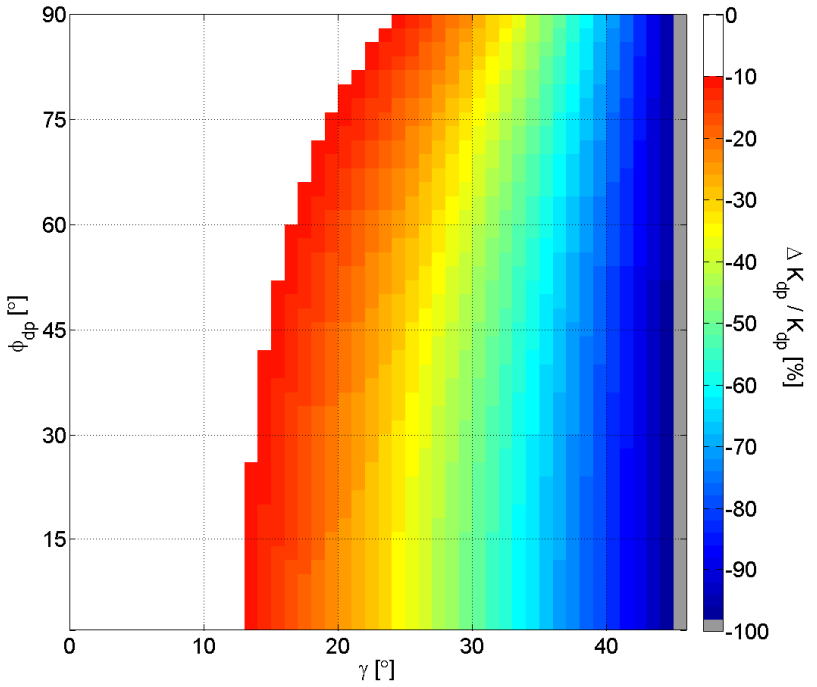

Figure 5.6. Relative error in K_{dp} as a function of rotation angle γ and differential propagation phase ϕ_{dp}. No color indicates region where error is less than 10%.

error in K_{dp} equals to 100%. This is expected, since if $\gamma = 45°$, then the differential propagation phase ϕ_{dp} is always equal to 0.

5.3.4 Linear depolarization ratio

Linear depolarization ratio LDR can be measured only in the alternate transmit mode of operation. It is defined as a ratio of the cross-polar signal power to the co-polar signal power:

$$\begin{aligned} LDR_h &= 10\log_{10}\left(\frac{\left\langle\left|s'_{vh}\right|^2\right\rangle}{\left\langle\left|s'_{hh}\right|^2\right\rangle}\right) \\ LDR_v &= 10\log_{10}\left(\frac{\left\langle\left|s'_{hv}\right|^2\right\rangle}{\left\langle\left|s'_{vv}\right|^2\right\rangle}\right) \end{aligned} \tag{5.31}$$

The cross-polar backscattering matrix element $s_{vh}^{(b)}$ is related to the angle between the propagation direction of the incident field and the hydrometeor symmetry axis δ and the canting angle β as(*Stapor and Pratt*, 1984):

$$s_{vh}^{(b)} \sim cos^2(\delta) sin(2\beta) \tag{5.32}$$

From (5.32) it can be deduced that LDR can be only finite if canting angle β and its distribution σ_β is larger than zero. A radar based study presented in *Bringi et al.* (2008) proved that the mean canting angle is close to 0° with a standard deviation (σ_β) of $7^\circ - 8^\circ$ in low wind conditions and 12° in moderate wind conditions. However, in case of a phase-tilt architecture, the self induced rotation angle γ results in the apparent canting angle $\beta = \gamma$. *Thurai et al.* (2014) performed scattering calculations using the T-matrix method with the measured drop size distributions as input at C-band. LDR increase up to $-10dB$ is reported for apparent canting angle varying from $0^\circ - 30^\circ$, if differential reflectivity larger than 2dB is considered.

Using the definitions given in (5.16) and (5.31), the LDR measured by a phase-tilt radar is:

$$\begin{aligned}
LDR_h^{(p)} &= 10\log_{10}\left(\frac{\left\langle \left| s_{vh}^{(p)} \right|^2 \right\rangle}{\left\langle \left| s_{hh}^{(p)} \right|^2 \right\rangle}\right) \\
&= 10\log_{10}\left(\frac{\left\langle \left| p_{11}p_{21}(s'_{vv} - s'_{hh}) \right|^2 \right\rangle}{\left\langle \left| p_{11}^2 s'_{hh} + p_{21}^2 s'_{vv} \right|^2 \right\rangle}\right) \\
&= 10\log_{10}\left(\frac{p_{11}^2 p_{21}^2 (Z'_{dr} + 1 - 2\sqrt{Z'_{dr}} Re[\rho'_{hv}])}{p_{11}^4 Z'_{dr} + p_{21}^4 + 2p_{11}^2 p_{21}^2 \sqrt{Z'_{dr}} Re[\rho'_{hv}]}\right) \\
&= 10\log_{10}\left(\frac{\frac{1}{4} sin^2(2\gamma)(Z'_{dr} + 1 - 2\sqrt{Z'_{dr}} Re[\rho'_{hv}])}{cos^4(\gamma) Z'_{dr} + sin^4(\gamma) + \frac{1}{2} sin^2(2\gamma)\sqrt{Z'_{dr}} Re[\rho'_{hv}]}\right)
\end{aligned} \tag{5.33}$$

$$
\begin{aligned}
LDR_v^{(p)} &= 10\log_{10}\left(\frac{\left\langle\left|s_{hv}^{(p)}\right|^2\right\rangle}{\left\langle\left|s_{vv}^{(p)}\right|^2\right\rangle}\right) \\
&= 10\log_{10}\left(\frac{\left\langle\left|p_{11}p_{21}(s'_{vv}-s'_{hh})\right|^2\right\rangle}{\left\langle\left|p_{11}^2 s'_{vv}+p_{21}^2 s'_{hh}\right|^2\right\rangle}\right) \\
&= 10\log_{10}\left(\frac{p_{11}^2 p_{21}^2(Z'_{dr}+1-2\sqrt{Z'_{dr}}Re[\rho'_{hv}])}{p_{11}^4+p_{21}^4 Z'_{dr}+2p_{11}^2p_{21}^2\sqrt{Z'_{dr}}Re[\rho'_{hv}]}\right) \\
&= 10\log_{10}\left(\frac{\frac{1}{4}sin^2(2\gamma)(Z'_{dr}+1-2\sqrt{Z'_{dr}}Re[\rho'_{hv}])}{cos^4(\gamma)+sin^4(\gamma)Z'_{dr}+\frac{1}{2}sin^2(2\gamma)\sqrt{Z'_{dr}}Re[\rho'_{hv}]}\right)
\end{aligned}
\tag{5.34}
$$

The LDR of a phase-tilt radar as a function of rotation angle γ and differential propagation phase ϕ_{dp} is shown in Figure 5.7. Bias in $LDR_v^{(p)}$ is slightly larger than that in $LDR_h^{(p)}$, because the signal power in V channel is expected to be lower due to the geometry of scatterers. Furthermore, the effect of depolarization of H and V waves in canted hydrometeors due to polarization rotation can be noticed as an increase in LDR with distance. *Ryzhkov* (2001) suggests to use this trend as an indication of either nonzero canting angle or system imperfections like nonorthogonality of transmitted and received waves. Finally, the bias in LDR can reach several decibels, and thus the observed improvement in LDR can be used to verify the effectiveness of polarization rotation correction presented in Section 5.2.

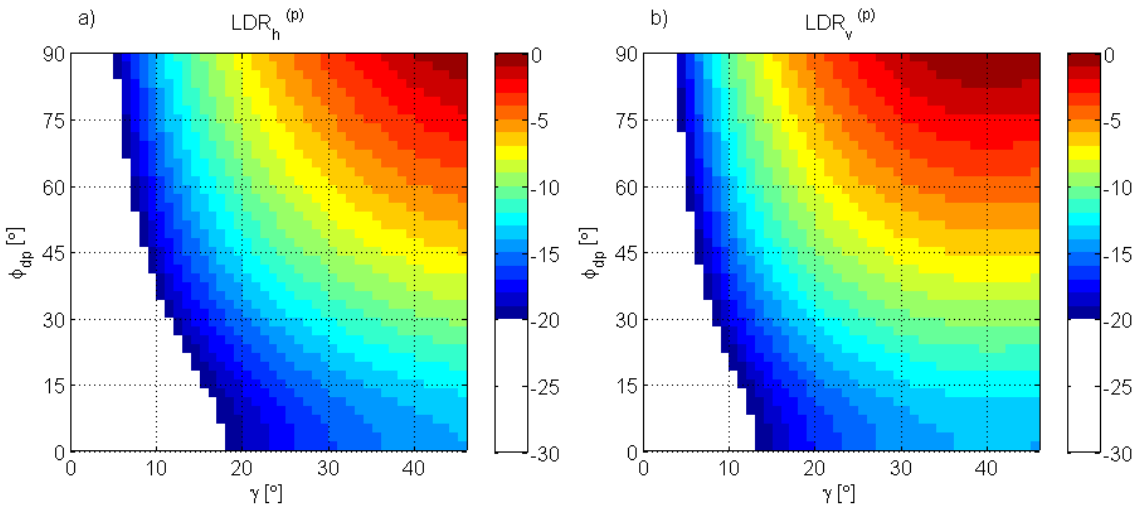

Figure 5.7. LDR of a phase-tilt radar as a function of rotation angle γ and differential propagation phase ϕ_{dp}. $Z_{DR} = 3dB$ and $\rho_{hv} = 0.98$ in all cases.

CHAPTER 6

CONCLUSIONS AND FUTURE WORK

The design and performance of a new low-profile, low-cost, weather radar has been demonstrated. Phased-array technology has been utilized due to its expected overall system cost reduction. The initial radar system price is subject to the cost of moving parts, such as the high-speed pedestal. Significant savings are available, if pedestal requirements can be limited. The proposed 1-D scanning architecture is a current compromise between development cost, maintenance cost and polarization purity requirements. The work on a next generation, 2-D radar is already in progress (*Weber et al.*, 2007). However, the system concept presented herein should be considered as a solution towards a low-maintenance weather radar only, rather than a multimission radar. The overall cost of the Phase-Tilt Weather Radar (parts only) presented in this dissertation is below 90 thousands US dollars. As of today, CASA licensed this system design to ITT, EWR, Vaisala and Raytheon. The latter, in cooperation with FirstRF, is offering this system commercially.

The performance of the prototype PTWR was verified by a comparison against high-power operational radars. The qualitative comparison with S-band and C-band radars revealed both: the advantages of X-band for weather observations such as higher mean spatial and temporal resolution, as well as, disadvantages such as lower sensitivity and higher attenuation caused by propagation in a water filled atmosphere. The quantitative comparison of uncorrected reflectivity fields measured by the PTWR and a collocated X-band radar demonstrated an excellent correlation value of 0.9. This confirms the hypothesis that a solid-state weather radar can be a valid alter-

native to the high-power magnetron systems. However, the lower signal-to-noise ratio detected by the PTWR impairs the quality of radar products, especially the co-polar correlation coefficient ρ_{hv}. This product is crucial for a correct hydrometeor classification, but is characterized by a very narrow dynamic range. Therefore, for upcoming deployments, a waveform with longer pulse duration and reduced bandwidth is suggested in order to increase radar sensitivity. Alternatively, the use of spectral processing or multi-lag time domain processing should be considered. Finally, it is expected that high-power solid-state transmitters will be available in the near future.

The calibration techniques at the element level have been developed, implemented and analyzed. It is confirmed that, using a calibration method based on a mutual coupling, a full array calibration is possible. Additionally, this technique is excellent for system diagnosis allowing for identification of malfunctioning TR modules. It is suggested to perform an extended in time calibration test in order to assess array performance stability. Furthermore, an in-field calibration technique using a horn antenna and pedestal have been evaluated. The introduced method allows for a satisfactory evaluation of the sidelobe level and the collocation of polarization patterns. However, a two-way beam calibration constant can only be synthesized using four independent measurements, which is inadequate for a precise absolute calibration required by weather radar. The calibration using a corner reflector mounted on a tower is not feasible due to high clutter contamination and is also not desired since a final phased-array weather radar solution will be lacking a pedestal. A suggested solution for an effective in-field end-to-end calibration is the utilization of a calibration target on a moving platform such as a commercial drone.

To overcome the inadequate sensitivity issue, the pulse compression technique was implemented. However, frequency modulation and long transmit pulses result in the well-known range sidelobes contamination. A method for a waveform and compression filter design was presented in this dissertation. Using real data collected

by a horn antenna, several waveforms were evaluated. It is demonstrated that sidelobe attenuation in excess of 40 dB compared to mainlobe power is possible at a minimal penalty in signal-to-noise ratio and range resolution. To the author's knowledge, this is also the first study which focuses on interrelation of all figures of merits (ISL,PSL, L_{mm},ΔR_{6dB}) rather than only peak sidelobe level. The performance of the designed waveform and a dedicated compression filter was also evaluated using PTWR data collected in a heavy clutter environment. An excellent sidelobe reduction, while preserving range resolution and SNR, is confirmed again. In order to further advance sidelobe reduction techniques, it is suggested to examine the effect of oversampling on inverse filter performance. Another option is to investigate NLFM waveforms with a higher α factor, which are supposed to provide even better PSL reduction, but at the considerable degradation of range resolution.

Finally, the phase-tilt architecture is negatively affected by a polarization rotation if beam is steered away from broadside direction and elevation angle is larger than 0°. The system geometry has been described and the effect of polarization rotation on reflectivity, differential reflectivity, specific differential phase, correlation coefficient and linear depolarization ratio has been demonstrated. In general we can conclude that the bias introduced by an apparent canting angle can be neglected if elevation angle is less than 15°. If a 2-D array is considered, this bias will be more significant and will require a correction similar to the one derived in Chapter 5. Finally, it is worth exploring the benefits offered by a phase-spin configuration, which performs electronic scanning in the vertical plane, while rotating mechanically in the horizontal plane. This setup is not affected by system polarization rotation and enables for a rapid full volume scan with a single 1-D phased-array system.

APPENDIX

SPACED ANTENNA BEAM PATTERNS

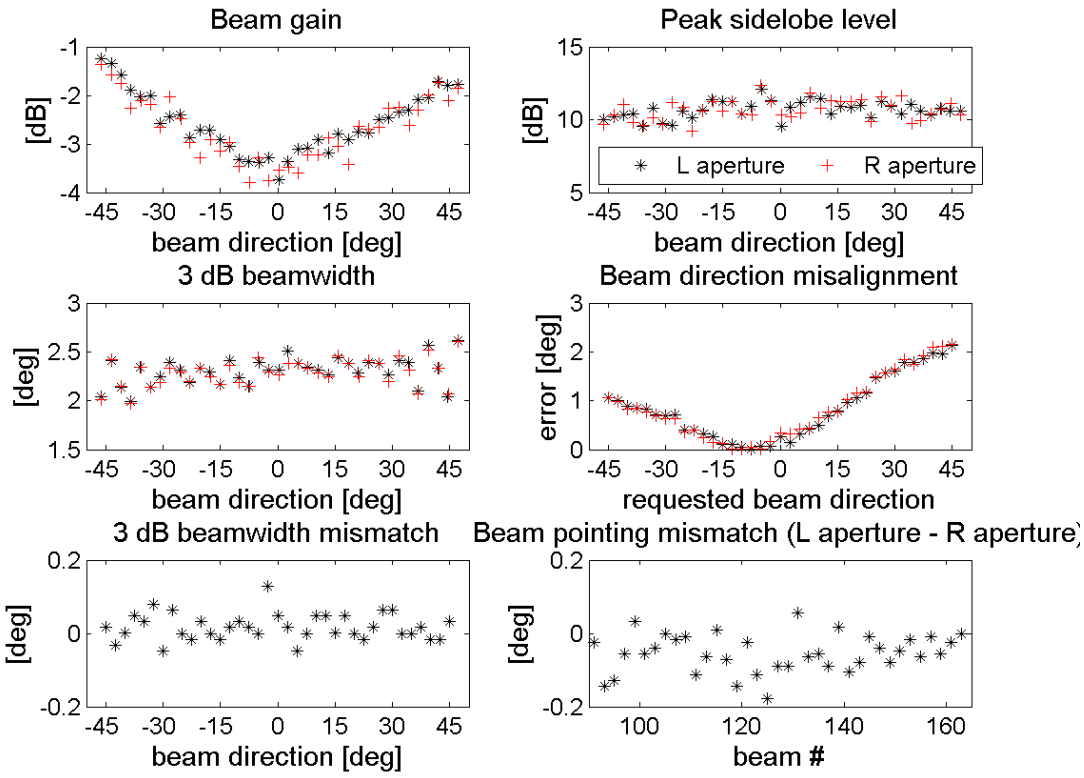

Figure A.1. Figures of merits for spaced antenna patterns of beams ID 91 – 164 in Tx-V-pol mode of operation. Beam gain is normalized to the broadside beam using all TR modules. The number of used TR modules is increased as beam is directed away from broadside.

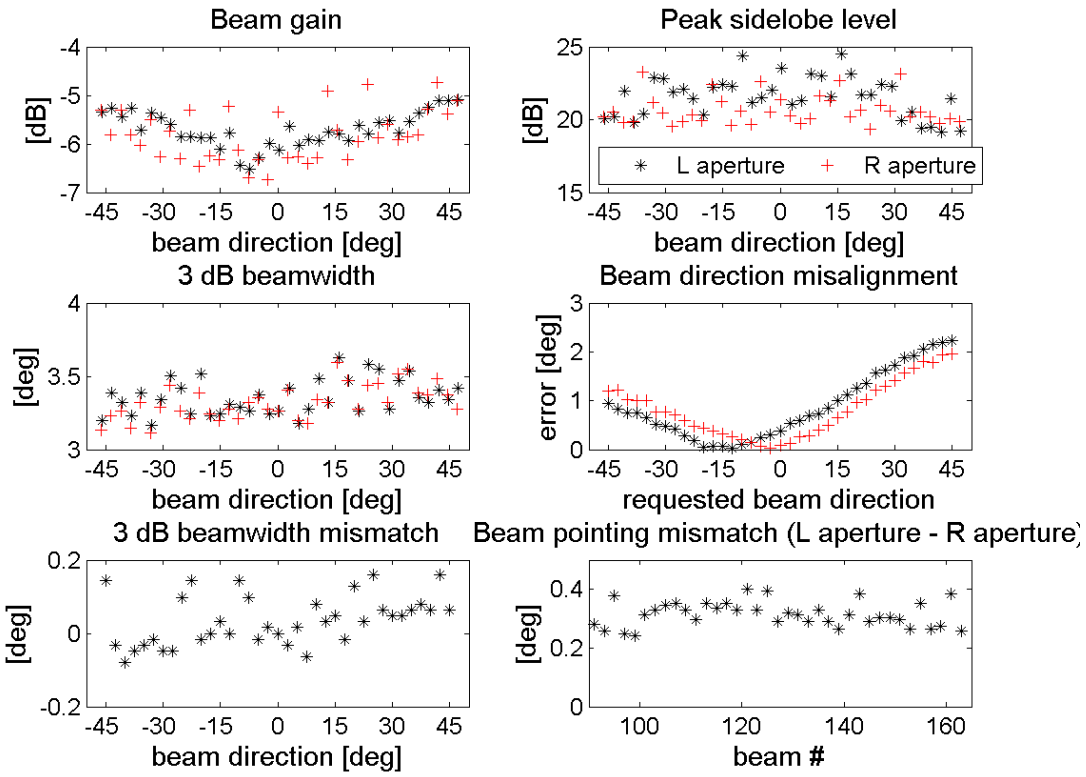

Figure A.2. Figures of merits for spaced antenna patterns of beams ID $91 - 164$ in Rx-V-pol mode of operation. Beam gain is normalized to the broadside beam using all TR modules. The number of used TR modules is increased as beam is directed away from broadside. Spaced antenna beams were designed to illuminate the same volume using different subset of available TR modules. The measurements indicate that beam pointing mismatch up to 0.4° can be expected.

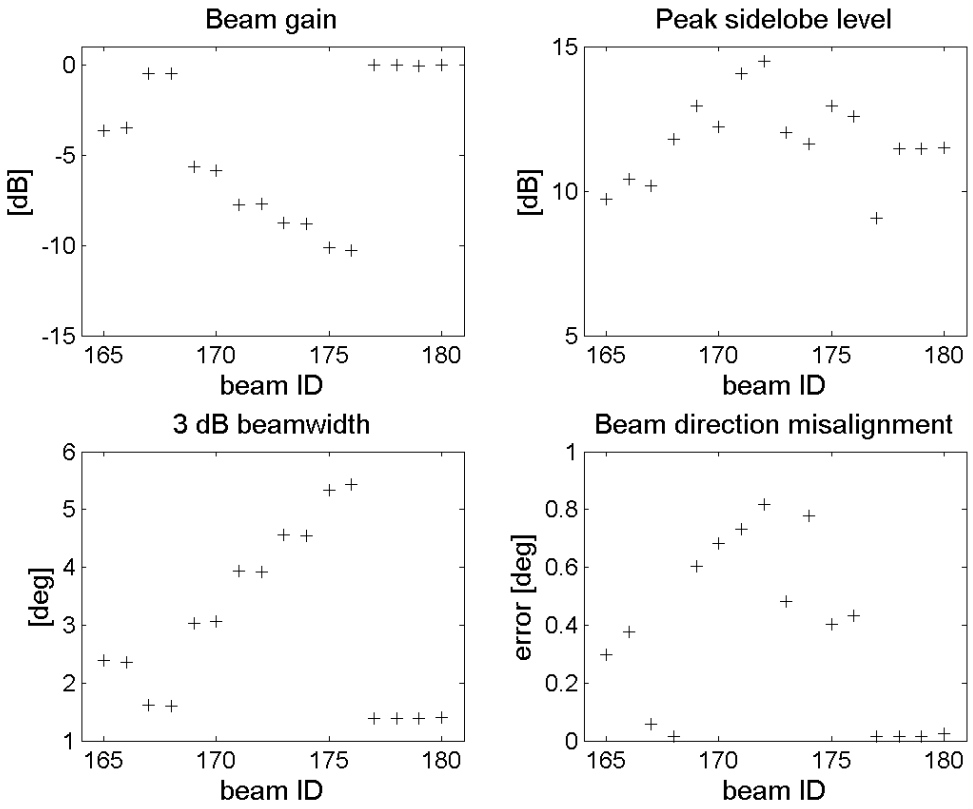

Figure A.3. Figures of merits for broadside antenna patterns of beams ID $165-180$ in Tx-V-pol mode of operation using variable number of TR modules. Beam IDs $177-180$ are using all available TR modules and can be used to quantify the precision of calibration measurements. The beam gain decreases and the beam width increases when the number of used TR modules is reduced (beams ID $167-176$).

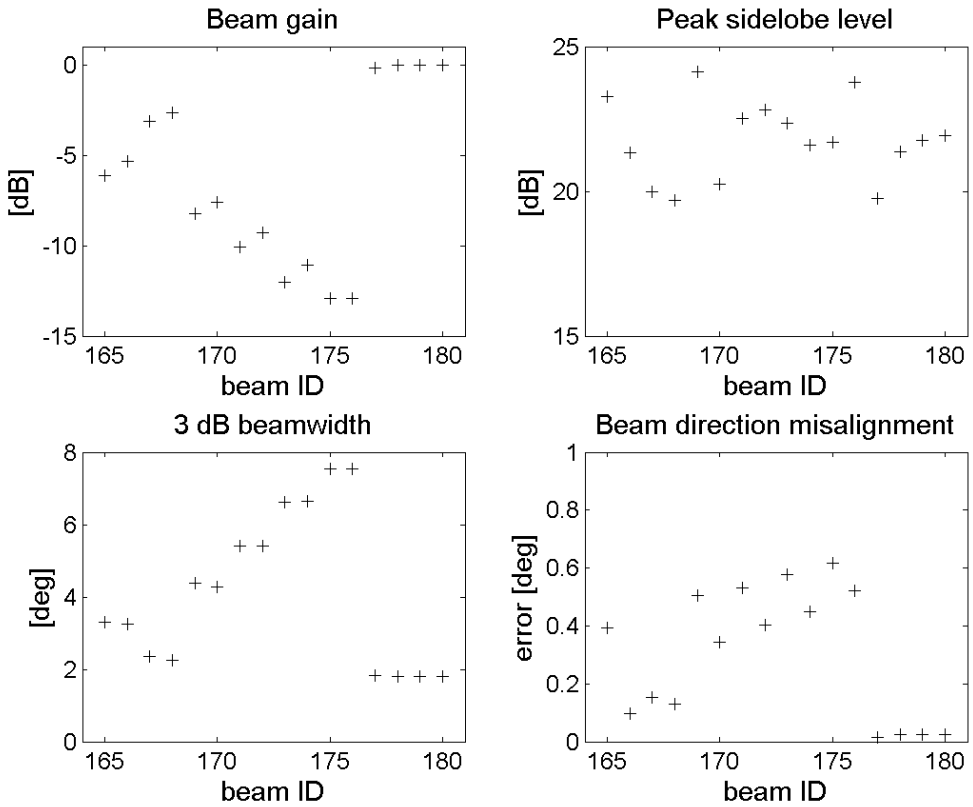

Figure A.4. Figures of merits for broadside antenna patterns of beams ID $165-180$ in Rx-V-pol mode of operation using variable number of TR modules. Beam IDs $177-180$ are using all available TR modules and can be used to quantify the precision of calibration measurements. The beam gain decreases and the beam width increases when the number of used TR modules is reduced (beams ID $167-176$). The beam pointing error increases when the number of TR modules is reduced.

BIBLIOGRAPHY

Ashe, J., R. Nevin, D. Murrow, H. Urkowitz, N. Bucci, and J. Nespor (1994), Range sidelobe suppression of expanded/compressed pulses with droop, in *Radar Conference, 1994., Record of the 1994 IEEE National*, pp. 116–122, doi:10.1109/NRC.1994.328109.

Aumann, H., A. Fenn, and F. Willwerth (1989), Phased array antenna calibration and pattern prediction using mutual coupling measurements, *Antennas and Propagation, IEEE Transactions on*, *37*(7), 844 –850, doi:10.1109/8.29378.

Austin, G. L. (1974), Pulse compression systems for use with meteorological radars, *Radio Science*, *9*(1), 2933, doi:10.1029/RS009i001p00029.

Bajaj, A., and B. Philips (2012), Casting the net - a revolutionary business model for depolying weather radar networks, *Meteorological Technology International*, pp. 106–108.

Bharadwaj, N., and V. Chandrasekar (2012), Wideband waveform design principles for solid-state weather radars, *Journal of Atmospheric and Oceanic Technology*, *29*(1), 14–31, doi:10.1175/JTECH-D-11-00030.1.

Bharadwaj, N., K. Widener, L. Andrei, and V. Venkatesh (2013), Calibration system for ARM radars.

Bluestein, H. B., M. M. French, I. PopStefanija, R. T. Bluth, and J. B. Knorr (2009), A mobile, phased-array doppler radar for the study of severe convective storms, *Bulletin of the American Meteorological Society*, *91*(5), 579–600, doi:10.1175/2009BAMS2914.1.

Bonato, M. (2002), A comparison of two computational technologies for digital pulse compression.

Bringi, V., M. Thurai, and D. Brunkow (2008), Measurements and inferences of raindrop canting angles, *Electronics Letters*, *44*(24), 1425–1426, doi:10.1049/el:20082899.

Bringi, V. N., and V. Chandrasekar (2001), *Polarimetric Doppler Weather Radar: Principles and Applications*, Cambridge University Press.

Brunkow, D., V. N. Bringi, P. C. Kennedy, S. A. Rutledge, V. Chandrasekar, E. A. Mueller, and R. K. Bowie (2000), A description of the CSUCHILL national radar facility, *Journal of Atmospheric and Oceanic Technology*, *17*(12), 1596–1608, doi:10.1175/1520-0426(2000)017⟨1596:ADOTCC⟩2.0.CO;2.

Buckreuss, S., W. Balzer, P. Muhlbauer, R. Werninghaus, and W. Pitz (2003), The terraSAR-x satellite project, in *Geoscience and Remote Sensing Symposium, 2003. IGARSS '03. Proceedings. 2003 IEEE International*, vol. 5, pp. 3096–3098 vol.5, doi:10.1109/IGARSS.2003.1294694.

Cao, Q., G. Zhang, R. Palmer, M. Knight, R. May, and R. Stafford (2012), Spectrum-time estimation and processing (STEP) for improving weather radar data quality, *IEEE Transactions on Geoscience and Remote Sensing*, *50*(11), 4670–4683, doi:10.1109/TGRS.2012.2190608.

Carlson, B. D., L. M. Goodman, J. Austin, M. W. Ganz, and L. O. Upton (1990), An ultralow-sidelobe adaptive array antenna, *The Lincoln Laboratory Journal*, pp. 291–310.

Chandrasekar, V., V. N. Bringi, N. Balakrishnan, and D. S. Zrnic (1990), Error structure of multiparameter radar and surface measurements of rainfall. part III: Specific differential phase, *Journal of Atmospheric and Oceanic Technology*, *7*(5), 621–629, doi:10.1175/1520-0426(1990)007⟨0621:ESOMRA⟩2.0.CO;2.

Chandrasekar, V., et al. (2013), The CASA dallas fort worth remote sensing network ICT for urban disaster mitigation, *EGU General Assembly*.

Chen, H., and V. Chandrasekar (2012), High resolution rainfall mapping in the dallas-fort worth urban demonstration network, in *Geoscience and Remote Sensing Symposium (IGARSS), 2012 IEEE International*, pp. 1936–1939, doi:10.1109/IGARSS.2012.6351123.

Cheong, B. L., J. Kurdzo, G. Zhang, and R. D. Palmer (2013), The impacts of multi-lag moment processor on a solid-state polarimetric weather radar, in *AMS 36th Conference on Radar Meteorology*.

Doviak, R. J., and D. S. Zrnic (1993), *Doppler Radar and Weather Observations*, Courier Dover Publications.

Doviak, R. J., V. Bringi, A. Ryzhkov, A. Zahrai, and D. Zrnic (2000), Considerations for polarimetric upgrades to operational WSR-88d radars, *Journal of Atmospheric and Oceanic Technology*, *17*(3), 257–278, doi:10.1175/1520-0426(2000)017⟨0257:CFPUTO⟩2.0.CO;2.

Farr, T. G., et al. (2007), The shuttle radar topography mission, *Reviews of Geophysics*, *45*(2), RG2004, doi:10.1029/2005RG000183.

Fetter, R. (1970), Radar weather performance enhanced by pulse compression, American Meteorological Society, Tucson, AZ.

Frasier, S. J., F. Kabeche, J. Figueras i Ventura, H. Al-Sakka, P. Tabary, J. Beck, and O. Bousquet (2013), In-place estimation of wet radome attenuation at x band, *Journal of Atmospheric & Oceanic Technology*, *30*(5), 917–928, doi:10.1175/JTECH-D-12-00148.1.

Frech, M. (2013), Monitoring the data quality of the new polarimetric weather radar network of the german meteorological service, Breckenridge, CO, USA.

Frigo, M., and S. Johnson (2005), The design and implementation of FFTW3, *Proceedings of the IEEE*, *93*(2), 216–231, doi:10.1109/JPROC.2004.840301.

Fulton, C., and W. Chappell (2009), Calibration techniques for digital phased arrays, in *Microwaves, Communications, Antennas and Electronics Systems, 2009. COMCAS 2009. IEEE International Conference on*, pp. 1 –10, doi:10.1109/COMCAS.2009.5385979.

George, J., K. V. Mishra, C. M. Nguyen, and V. Chandrasekar (2010), Implementation of blind zone and range-velocity ambiguity mitigation for solid-state weather radar, in *2010 IEEE Radar Conference*, pp. 1434–1438, IEEE, doi:10.1109/RADAR.2010.5494392.

Golestani, K., T. Chandrasekar, and R. Keeler (1995), Dual polarized staggered PRT scheme for weather radars: analysis and applications, *IEEE Transactions on Geoscience and Remote Sensing*, *33*(2), 239–246, doi:10.1109/36.377923.

Gosset, M., and I. Zawadzki (2001), Effect of nonuniform beam filling on the propagation of the radar signal at x-band frequencies. part i: Changes in the k(z) relationship, *Journal of Atmospheric and Oceanic Technology*, *18*(7), 1113–1126, doi:10.1175/1520-0426(2001)018⟨1113:EONBFO⟩2.0.CO;2.

Harris, F. (1978), On the use of windows for harmonic analysis with the discrete fourier transform, *Proceedings of the IEEE*, *66*(1), 51–83, doi:10.1109/PROC.1978.10837.

Heinselman, P. L., D. L. Priegnitz, K. L. Manross, T. M. Smith, and R. W. Adams (2008), Rapid sampling of severe storms by the national weather radar testbed phased array radar, *Weather and Forecasting*, *23*(5), 808–824, doi:10.1175/2008WAF2007071.1.

Hopf, A., J. Salazar, R. Medina, V. Venkatesh, E. Knapp, S. Frasier, and D. McLaughlin (2009), CASA phased array radar system description, simulation and products, in *Geoscience and Remote Sensing Symposium,2009 IEEE International,IGARSS 2009*, vol. 2, pp. II–968–II–971, doi:10.1109/IGARSS.2009.5418262.

Hwang, C. A., and R. J. Keeler (1995), Sample phase aspects of FM pulse compression waveforms, in *Geoscience and Remote Sensing Symposium, 1995. IGARSS '95. 'Quantitative Remote Sensing for Science and Applications', International*, vol. 3, pp. 2126–2128 vol.3, IEEE, doi:10.1109/IGARSS.1995.524126.

Isom, B., et al. (2013), The atmospheric imaging radar: Simultaneous volumetric observations using a phased array weather radar, *Journal of Atmospheric and Oceanic Technology*, *30*(4), 655–675, doi:10.1175/JTECH-D-12-00063.1.

Junyent, F., V. Chandrasekar, D. McLaughlin, E. Insanic, and N. Bharadwaj (2010), The CASA integrated project 1 networked radar system, *Journal of Atmospheric and Oceanic Technology*, *27*(1), 61–78, doi:10.1175/2009JTECHA1296.1.

Kaltenboeck, R. (2012), "new generation of dual polarized weather radars in austria, Toulouse.

Karimkashi, S., G. Zhang, R. Kelley, J. Meier, R. Palmer, A. Zahrai, R. Doviak, and D. Zrnic (2013), Cylindrical polarimetric phased array radar demonstrator: Design and analysis of a frequency scanning antenna array, in *2013 IEEE International Symposium on Phased Array Systems Technology*, pp. 477–480, doi: 10.1109/ARRAY.2013.6731874.

Keeler, R., and C. Hwang (1995), Pulse compression for weather radar, in *Radar Conference, 1995., Record of the IEEE 1995 International*, pp. 529–535, doi:10. 1109/RADAR.1995.522603.

Keeler, R., J. Lutz, and J. Vivekanandan (2000), S-pol: NCAR's polarimetric doppler research radar, in *Geoscience and Remote Sensing Symposium, 2000. Proceedings. IGARSS 2000. IEEE 2000 International*, vol. 4, pp. 1570–1573 vol.4, doi:10.1109/ IGARSS.2000.857275.

Knapp, E., J. Salazar, R. Medina, A. Krishnamurthy, and R. Tessier (2011), Phase-tilt radar antenna array, in *Microwave Conference (EuMC), 2011 41st European*, pp. 1055–1058.

Knorr, J. (2007), Weather radar equation correction for frequency agile and phased array radars, *IEEE Transactions on Aerospace and Electronic Systems*, *43*(3), 1220–1227, doi:10.1109/TAES.2007.4383614.

Kowatsch, M., and H. R. Stocker (1982), Effect of fresnel ripples on sidelobe suppression in low time-bandwidth product linear FM pulse compression, *Communications, Radar and Signal Processing, IEE Proceedings F*, *129*(1), 41–44, doi: 10.1049/ip-f-1:19820007.

Krishnamurthy, A. (2011), Design of an FPGA-based array formatter for CASA phase-tilt radar system, *Masters Theses 1896 - February 2014*.

Lanczos, C. (1956), *Applied analysis.*, Prentice-Hall, Englewood Cliffs, N.J.

Lei, L., G. Zhang, R. J. Doviak, R. Palmer, B. L. Cheong, M. Xue, Q. Cao, and Y. Li (2012), Multilag correlation estimators for polarimetric radar measurements in the presence of noise, *Journal of Atmospheric and Oceanic Technology*, *29*(6), 772–795, doi:10.1175/JTECH-D-11-00010.1.

Lei, L., G. Zhang, and R. Doviak (2013), Bias correction for polarimetric phased-array radar with idealized aperture and patch antenna elements, *IEEE Transactions on Geoscience and Remote Sensing*, *51*(1), 473–486, doi:10.1109/TGRS.2012.2198070.

Liu, H., and V. Chandrasekar (2000), Classification of hydrometeors based on polarimetric radar measurements: Development of fuzzy logic and neuro-fuzzy systems, and in situ verification, *Journal of Atmospheric and Oceanic Technology*, *17*(2), 140–164, doi:10.1175/1520-0426(2000)017⟨0140:COHBOP⟩2.0.CO;2.

Mailloux, R. J. (2005), *Phased Array Antenna Handbook*, Artech House.

McLaughlin, D., et al. (2009), Short-wavelength technology and the potential for distributed networks of small radar systems, *Bulletin of the American Meteorological Society*, *90*(12), 1797–1817, doi:10.1175/2009BAMS2507.1.

Medina, R., E. Knapp, J. Salazar, and D. McLaughlin (2012a), T/R module for CASA phase-tilt radar antenna array, in *Microwave Conference (EuMC), 2012 42nd European*, pp. 1293–1296.

Medina, R., J. Salazar, E. Knapp, and D. McLaughlin (2012b), Calibration and validation of the CASA phased array antenna, in *Microwave Conference (EuMC), 2012 42nd European*, pp. 940–943.

Medina-Sanchez, R. (2013), BEAM STEERING CONTROL SYSTEM FOR LOW-COST PHASED ARRAY WEATHER RADARS: DESIGN AND CALIBRATION TECHNIQUES, *Doctoral Dissertations 2014-current*.

Mudukutore, A., V. Chandrasekar, and R. Keeler (1998), Pulse compression for weather radars, *IEEE Transactions on Geoscience and Remote Sensing*, *36*(1), 125–142, doi:10.1109/36.655323.

Nakagawa, K., H. Hanado, N. Takahashi, S. Satoh, K. Fukutani, and T. Iguchi (2006), Development of a c-band polarimetric and pulse compression radar in okinawa, japan, in *IEEE International Conference on Geoscience and Remote Sensing Symposium, 2006. IGARSS 2006*, pp. 1670–1673, doi:10.1109/IGARSS.2006.431.

O'Hora, F., and J. Bech (2007), Improving weather radar observations using pulsecompression techniques, *Meteorological Applications*, *14*(4), 389–401, doi:10.1002/met.38.

Palmer, R. D., et al. (2011), Observations of the 10 may 2010 tornado outbreak using OU-PRIME: Potential for new science with high-resolution polarimetric radar, *Bulletin of the American Meteorological Society*, *92*(7), 871–891, doi:10.1175/2011BAMS3125.1.

Richards, M. A. (2005), *Fundamentals of radar signal processing*, McGraw-Hill, New York.

Richards, M. A., J. Scheer, and W. A. Holm (2010), *Principles of modern radar*, SciTech Publishing, Raleigh, NC.

Ryzhkov, A. V. (2001), Interpretation of polarimetric radar covariance matrix for meteorological scatterers: Theoretical analysis, *Journal of Atmospheric and Oceanic Technology*, *18*(3), 315–328, doi:10.1175/1520-0426(2001)018⟨0315:IOPRCM⟩2.0.CO;2.

Ryzhkov, A. V., and D. S. Zrnic (2007), Depolarization in ice crystals and its effect on radar polarimetric measurements, *Journal of Atmospheric and Oceanic Technology*, *24*(7), 1256–1267, doi:10.1175/JTECH2034.1.

Ryzhkov, A. V., S. E. Giangrande, and T. J. Schuur (2005), Rainfall estimation with a polarimetric prototype of WSR-88d, *Journal of Applied Meteorology*, *44*(4), 502–515, doi:10.1175/JAM2213.1.

Sachidananda, M., and D. S. Zrnic (1985), ZDR measurement considerations for a fast scan capability radar, *Radio Science*, *20*(4), 907–922, doi:10.1029/RS020i004p00907.

Sachidananda, M., and D. S. Zrnic (1989), Efficient processing of alternately polarized radar signals, *Journal of Atmospheric and Oceanic Technology*, *6*(1), 173–181, doi:10.1175/1520-0426(1989)006⟨0173:EPOAPR⟩2.0.CO;2.

Salazar, J., R. Medina, E. Knapp, and D. McLaughlin (2008), Phase-tilt array antenna design for dense distributed radar networks for weather sensing, in *Geoscience and Remote Sensing Symposium, 2008. IGARSS 2008. IEEE International*, vol. 5, pp. V – 318–V – 321, doi:10.1109/IGARSS.2008.4780092.

Salazar, J., E. Knapp, and D. McLaughlin (2010), Dual-polarization performance of the phase-tilt antenna array in a casa dense network radar, in *Geoscience and Remote Sensing Symposium (IGARSS), 2010 IEEE International*, pp. 3470–3473, doi:10.1109/IGARSS.2010.5650310.

Salazar Cerreno, J. L. (2012), The feasibility of low-cost, dual-polarized, phase-tilt antenna arrays for dense radar networks, *Doctoral Dissertations Available from Proquest*, pp. 1–200.

Shipley, C., and D. Woods (2000), Mutual coupling-based calibration of phased array antennas, in *Phased Array Systems and Technology, 2000. Proceedings. 2000 IEEE International Conference on*, pp. 529 –532, doi:10.1109/PAST.2000.859012.

Siggia, R. E. P. J., A. D. (2004), Gaussian model adaptive processing (GMAP) for improved ground clutter cancellation and moment calculation.

Skolnik, M. I. (1962), *Introduction to radar systems.*, McGraw-Hill, New York, Auckland.

Snyder, J. C., H. B. Bluestein, G. Zhang, and S. J. Frasier (2010), Attenuation correction and hydrometeor classification of high-resolution, x-band, dual-polarized mobile radar measurements in severe convective storms, *Journal of Atmospheric and Oceanic Technology*, *27*(12), 1979–2001, doi:10.1175/2010JTECHA1356.1.

Snyder, J. C., H. B. Bluestein, V. Venkatesh, and S. J. Frasier (2013), Observations of polarimetric signatures in supercells by an x-band mobile doppler radar, *Monthly Weather Review*, *141*(1), 3–29, doi:10.1175/MWR-D-12-00068.1.

Stapor, D. P., and T. Pratt (1984), A generalized analysis of dual-polarization radar measurements of rain, *Radio Science*, *19*(1), 90–98, doi:10.1029/RS019i001p00090.

Tanamachi, R. L., H. B. Bluestein, M. Xue, W.-C. Lee, K. A. Orzel, S. J. Frasier, and R. M. Wakimoto (2013), Near-surface vortex structure in a tornado and in a sub-tornado-strength convective-storm vortex observed by a mobile, w-band radar during VORTEX2, *Monthly Weather Review*, *141*(11), 3661–3690, doi:10.1175/MWR-D-12-00331.1.

Thurai, M., P. T. May, and A. Protat (2014), Shipborne polarimetric weather radar: Impact of ship movement on polarimetric variables at c band, *Journal of Atmospheric and Oceanic Technology*, *31*(7), 1557–1563, doi:10.1175/JTECH-D-13-00242.1.

Torres, S. (2012), ADAPTS implementation: Can we exploit phased-array radar's electronic beam steering capabilities to reduce update times?, New Orleans, USA.

Torres, S. M., and D. S. Zrnic (1999), Ground clutter canceling with a regression filter, *Journal of Atmospheric and Oceanic Technology*, *16*(10), 1364–1372, doi:10.1175/1520-0426(1999)016⟨1364:GCCWAR⟩2.0.CO;2.

Treitel, S., and E. A. Robinson (1966), The design of high-resolution digital filters, *IEEE Transactions on Geoscience Electronics*, *4*(1), 25–38, doi:10.1109/TGE.1966.271203.

Venkatesh, V. (2013), Spaced-antenna wind estimation using an x-band active phased-array weather radar, *Doctoral Dissertations Available from Proquest*, pp. 1–162.

Venkatesh, V., et al. (2008), The UMass x-pol mobile doppler radar: Description, recent observations, and new system developments, in *Geoscience and Remote Sensing Symposium, 2008. IGARSS 2008. IEEE International*, vol. 5, pp. V – 101–V – 104, doi:10.1109/IGARSS.2008.4780037.

Wakimoto, R. M., and V. N. Bringi (1988), Dual-polarization observations of microbursts associated with intense convection: The 20 july storm during the MIST project, *Monthly Weather Review*, *116*(8), 1521–1539, doi:10.1175/1520-0493(1988)116⟨1521:DPOOMA⟩2.0.CO;2.

Wang, Y., and V. Chandrasekar (2006), Polarization isolation requirements for linear dual-polarization weather radar in simultaneous transmission mode of operation, *IEEE Transactions on Geoscience and Remote Sensing*, *44*(8), 2019–2028, doi:10.1109/TGRS.2006.872138.

Weber, M. E., J. Y. N. Cho, J. S. Herd, J. M. Flavin, W. E. Benner, and G. S. Torok (2007), The next-generation multimission u.s. surveillance radar network, *Bulletin of the American Meteorological Society*, *88*(11), 1739–1751, doi:10.1175/BAMS-88-11-1739.

Wu, C., and L. Liu (2014), Comparison of the observation capability of an x-band phased-array radar with an x-band doppler radar and s-band operational radar, *Advances in Atmospheric Sciences*, *31*(4), 814–824, doi:10.1007/s00376-013-3072-5.

Wurman, J., and M. Randall (2001), An inexpensive, mobile, rapid-scan radar, in *Preprints, 30th Int. Conf. on Radar Meteorology*, AMS, Munich, Germany.

Wurman, J., D. Dowell, Y. Richardson, P. Markowski, E. Rasmussen, D. Burgess, L. Wicker, and H. B. Bluestein (2012), The second verification of the origins of rotation in tornadoes experiment: VORTEX2, *Bulletin of the American Meteorological Society*, *93*(8), 1147–1170, doi:10.1175/BAMS-D-11-00010.1.

Yu, T.-Y., M. B. Orescanin, C. D. Curtis, D. S. Zrnic, and D. E. Forsyth (2007), Beam multiplexing using the phased-array weather radar, *Journal of Atmospheric and Oceanic Technology*, *24*(4), 616–626, doi:10.1175/JTECH2052.1.

Zhang, G., R. Doviak, D. Zrnic, J. Crain, D. Staiman, and Y. Al-Rashid (2009), Phased array radar polarimetry for weather sensing: A theoretical formulation for bias corrections, *IEEE Transactions on Geoscience and Remote Sensing*, *47*(11), 3679–3689, doi:10.1109/TGRS.2009.2029332.

Zhao, S., and H. J. Xin (2009), Study of side lobes suppression for using pulse compression in weather radar, in *2nd International Congress on Image and Signal Processing, 2009. CISP '09*, pp. 1–3, IEEE, doi:10.1109/CISP.2009.5301110.

Zrnic, D., and P. Mahapatra (1985), Two methods of ambiguity resolution in pulse doppler weather radars, *IEEE Transactions on Aerospace and Electronic Systems*, *AES-21*(4), 470–483, doi:10.1109/TAES.1985.310635.

Zrnic, D., R. Doviak, G. Zhang, and A. Ryzhkov (2010), Bias in differential reflectivity due to cross coupling through the radiation patterns of polarimetric weather radars, *Journal of Atmospheric and Oceanic Technology*, *27*(10), 1624–1637, doi:10.1175/2010JTECHA1350.1.

Zrnic, D., G. Zhang, and R. Doviak (2011), Bias correction and doppler measurement for polarimetric phased-array radar, *IEEE Transactions on Geoscience and Remote Sensing*, *49*(2), 843–853, doi:10.1109/TGRS.2010.2057436.